Advancing eddy parameterizations: Dynamic energy backscatter and the role of subgrid advection and stochastic forcing

Ekaterina Bagaeva[1], Sergey Danilov[2], Marcel Oliver[3], and Stephan Juricke[4]

[1]Constructor University
[2]Alfred Wegener Institute, Helmholtz Centre for Polar and Marine Research
[3]MIDS at KU Eichstätt-Ingolstadt
[4]Jacobs University Bremen

August 24, 2023

Abstract

A universal approach to overcome resolution limitations in the ocean is to parametrize physical processes. The traditional method of parametrizing mesoscale range processes on eddy-permitting mesh resolutions, known as a viscous momentum closure, tends to over-dissipate eddy kinetic energy. To return excessively dissipated energy to the system, the viscous closure is equipped with a dynamic energy backscatter, which amplitude is based on the amount of unresolved kinetic energy (UKE). Our study suggests including the advection of UKE to consider the effects of nonlocality on the subgrid. Furthermore, we suggest incorporating a stochastic element into the subgrid energy equation to account for variability, which is not present in a fully deterministic approach. This study demonstrates increased eddy activity and highlights improved flow characteristics. In addition, we provide diagnostics of optimal scale separation between dissipation and injection operators. The implementations are tested on two intermediate complexity setups of the global ocean model FESOM2: an idealized channel setup and a double-gyre setup.

Advancing eddy parameterizations: Dynamic energy backscatter and the role of subgrid advection and stochastic forcing

Ekaterina Bagaeva[1,2], Sergey Danilov[2], Marcel Oliver[3], Stephan Juricke[1,2]

[1]Constructor University, Campus Ring 1, 28759 Bremen, Germany
[2]Alfred Wegener Institute for Polar and Marine Research, Am Handelshafen 12, 27570 Bremerhaven, Germany
[3]Mathematical Institute for Machine Learning and Data Science, KU Eichstätt–Ingolstadt, Auf der Schanz 49, 85049 Ingolstadt, Germany

Key Points:

- Implementation and positive evaluation of subgrid advection for kinetic energy backscatter parameterization
- Inclusion of new stochastic term - based on high-resolution data - to subgrid energy equation
- Scale analysis reveals the necessity of sufficient scale separation between viscous energy dissipation and energy injection via backscatter

Corresponding author: Ekaterina Bagaeva, `ebagaeva@constructor.university`

Abstract

A universal approach to overcome resolution limitations in the ocean is to parametrize physical processes. The traditional method of parametrizing mesoscale range processes on eddy-permitting mesh resolutions, known as a viscous momentum closure, tends to over-dissipate eddy kinetic energy. To return excessively dissipated energy to the system, the viscous closure is equipped with a dynamic energy backscatter, which amplitude is based on the amount of unresolved kinetic energy (UKE). Our study suggests including the advection of UKE to consider the effects of nonlocality on the subgrid. Furthermore, we suggest incorporating a stochastic element into the subgrid energy equation to account for variability, which is not present in a fully deterministic approach. This study demonstrates increased eddy activity and highlights improved flow characteristics. In addition, we provide diagnostics of optimal scale separation between dissipation and injection operators. The implementations are tested on two intermediate complexity setups of the global ocean model FESOM2: an idealized channel setup and a double-gyre setup.

Plain Language Summary

Modeling oceanic eddies requires incorporating physical processes through additional equations. While the overall understanding of the ocean is clear, the models tend to lose too much kinetic energy, resulting in systematic errors. Our goal in this study is to explore how to prevent false energy loss by sending the energy back to where it originated. Our research shows that by adding an advection and a random element, the current method can better capture the turbulent nature of the flow. We tested the implementation on the channel and the double-gyre setups and observed an increase in eddy activity and an improvement in flow characteristics.

1 Introduction

Mesoscale eddies play an important role in determining ocean circulation. They contain a large part of the kinetic energy (KE) of the ocean, contribute to the transfer of heat and properties, and impact the form and evolution of ocean currents. Their horizontal size is proportional to the Rossby radius of deformation, which reaches up to 200 km in the low latitudes, decreasing to less than 10 km in high latitudes. In addition, the Rossby radius decreases in shelf areas reflecting weak density stratification and small depth.

Mesoscale eddies are generated through different types of instabilities, with the most prominent sources being the baroclinic instability and the instabilities of the mean flow. Baroclinic instability releases the available potential energy (APE) maintained by the mean forcing of the ocean, transferring it into eddy kinetic energy (EKE) across a range of scales near the Rossby deformation radius (Ferrari & Wunsch, 2009).

A direct cascade of enstrophy to small scales and an inverse cascade of energy to large scales usually accompany the dynamics of mesoscale eddies. Eddy kinetic energy is partly transferred to mean kinetic energy, but the rest of the upscale transfer is stopped by large-scale friction, eddy killing by winds at the surface, interactions with topography, or wave generation. Enstrophy and some energy go downscale, reaching grid scales where they need to be dissipated through horizontal eddy viscosity. In nature, at even smaller scales of the cascade, the flow transitions to ageostrophic turbulence and waves and finally to three-dimensional turbulence, the energy of which is converted to heat by molecular dissipation.

In climate studies, ocean models are integrated over hundreds of years, which limits their resolution to coarse (around 1°) or eddy-permitting resolutions (around 1/4°)(Hewitt et al., 2020). Baroclinic instability in an ocean model is not resolved at coarse resolution, and eddy-driven transfers of buoyancy and other properties are absent. The APE cannot be converted to EKE; it has to be taken out by parameterizations compensating for the missing eddies. This is generally done by the Gent-McWilliams (GM) parameterization (Gent & McWilliams, 1990; Gent, 2011), which introduces the so-called eddy bolus velocities, which model the eddy-driven property fluxes and release the APE. Additionally, the missing mixing by eddies along isopycnal surfaces is parameterized by isopycnal diffusion (Redi, 1982)

The horizontal grids with a cell size around $1/4°$ or $1/6°$ are often described as "eddy-permitting." Such grids are sufficiently fine to represent eddies and simulate baroclinic instability in parts of the ocean. The GM parameterization must be carefully tuned on eddy-permitting meshes, as described in Hallberg (2013). However, the range of resolved scales on such meshes is not large enough, and viscous closures (e.g., Fox-Kemper et al., 2008) intended to eliminate enstrophy and energy at grid scales also affect the scales where eddies are generated by baroclinic instability and where the bulk of EKE is residing. As a result, both EKE and eddy generation are excessively dissipated. Until the resolution reaches the level of resolving sub-mesoscale dynamics (generally finer than 5 km at midlatitudes), the entire range of scales, including large scales, will be exposed to the over-dissipation, as illustrated, e.g., by Soufflet et al. (2016). It leads to an underestimated transfer of heat, salt, momentum and misrepresentation of the mean dynamics of the ocean and the forcing sensitivity of models.

For a more accurate ocean simulation and better representation of eddy dynamics, energy dissipated due to horizontal viscosity should be returned back to the system. The kinetic energy backscatter parameterization proposed for the ocean in Jansen et al. (2015) and developed further by Juricke et al. (2019) is intended to help in such situations. Within our work, energy backscatter performs the function of energy reinjection, transferring energy to the scales of eddy generation, thereby compensating the over-dissipation of the large scales and energizing the entire range of scales.

The concept of energy backscatter in its deterministic and stochastic forms has a long history of research in atmospheric and ocean sciences. Physical and numerical approaches to the compensation of excessive energy losses for atmospheric parameterization were mentioned in the works of e.g. Berner et al. (2009), Leutbecher et al. (2017), Dwivedi et al. (2019). Idealized ocean models were enhanced by backscatter to account for the dynamics of unresolved mesoscale eddies in the works of e.g. Frederiksen et al. (2013), Jansen and Held (2014), Jansen et al. (2015), Zanna et al. (2017).

The task of backscatter implementation has simple solutions, such as a kinematic backscatter, proposed in Juricke et al. (2020). It reduces viscous over dissipation by subtracting locally averaged viscous force multiplied by a tuning coefficient. This parameterization does not increase the computational costs and significantly improves ocean simulation toward the high-resolution truth. However, it acts instantaneously and can not be flow-aware simply due to the backscatter design.

More physically grounded and reliable is the concept of dynamic energy backscatter, whose amplitude depends on the subgrid energy, first introduced in the context of eddy-permitting ocean models by Jansen et al. (2015) and developed further by Juricke et al. (2019). The subgrid kinetic energy budget, which will be explained further, controls how the excessively dissipated energy is returned back to the resolved scales. This work aims to contribute to the theory and practical use of the kinetic energy backscatter in the following three directions.

First, the existing implementations of dynamic kinetic energy backscatter by Jansen et al. (2015), Juricke et al. (2019), Juricke et al. (2020b), Klöwer et al. (2018) are either considering the balance of unresolved (subgrid) EKE (i.e., UKE) as taking place locally or being distributed by the barotropic (vertically mean) flow (Jansen et al., 2019). This is arguably a simplification, as UKE should be transported by the fully resolved 3D flow, and a question arises whether ignoring this transport is a good approximation. Indeed, one may expect that input (generation) of subgrid energy and its dissipation are not colocated, and the UKE density at a given point is influenced by its input in regions upstream. Only in situations when the flow statistics are homogeneous in the direction of mean flow (e.g., a uniform zonally re-entrant channel flow), the advection can be assumed to be of minor importance, but even in such cases, eddies can be strong enough to introduce inhomogeneities affecting the distribution of UKE in space.

This paper tries to partly answer the question of the role of subgrid advection. For this, we implement full 3D advection of UKE in backscatter parameterization of Juricke et al. (2019) and demonstrate that accounting for advection leads to consistent improvements compared to control simulations in which the advection of UKE was ignored. This conclusion holds even for the channel setup with zonally homogeneous mean flow.

Second, while stochastic backscatter can offer more freedom in how to return energy to the resolved scales than deterministic backscatter and also can be used to represent missing variability and subgrid uncertainties, the question of the optimal form of the stochastic contribution in backscatter schemes remains open. Among existing studies, stochastic eddy forcing is applied to the quasi-geostrophic model in Mana and Zanna (2014); stochastic parameterizations extracting information from the subgrid eddy statistics are studied in Grooms and Majda (2013), Grooms et al. (2015); stochastic forcing is applied to velocity and temperature equations in Cooper (2017); stochastic perturbations are tested on various parameterization schemes in Juricke et al. (2017). Perezhogin (2019) develops and compares deterministic and stochastic kinetic energy backscatter schemes for the primitive equations of the ocean. The interest of the ocean modeling community in stochastic schemes remains high and is expected to increase further during this decade (Fox-Kemper et al., 2019).

We propose to combine the deterministic backscatter with a stochastic approach by adding a new stochastic term to the UKE. The new term is designed to improve the simulated eddy variability using data from a high-resolution reference simulation denoted as truth. We test different intensities of such a data-driven stochastic term and find that certain intensity ranges benefit the flow. However, exceeding these intensity intervals can lead to serious flow distortion.

Third, in both deterministic and stochastic energy backscatter parameterizations, one has to decide about the scale of energy injection. Spatial smoothing applied to the injection ensures a scale separation between energy reinjection and energy dissipation. Spatial filtering operators commonly involve only the nearest discrete cells for the reason of parallel implementation. Every cycle of spatial filtering applied to the operators increases the scales on which these operators act. Both over-smoothing and insufficient smoothing hamper performance of the backscatter term.

Understanding scale separation is also essential when several parameterizations are applied simultaneously. Jansen et al. (2019) consider a generalized energy-based parameterization that combines the GM parameterization and backscatter approach proposed in Jansen et al. (2015). The GM parameterization dissipates APE at the grid scales and represents the effect of the conversion of APE into EKE; however, classically ignoring the respective EKE input into the momentum equations. A significant result of their paper is the opportunity to smoothly tune the model between non-eddy-resolving and eddy-resolving regimes by coupling GM to the backscatter parameterization.

The question on optimal smoothing is the third question addressed in this work. We show that insufficient scale separation could cause a leak of energy and the inability of the flow structures to propagate coherently.

The set of numerical simulations addresses the three research questions raised above. We run the Finite-volumE Sea ice-Ocean Model (FESOM2, Danilov et al., 2017; Scholz et al., 2019) for two middle complexity setups: a channel setup and a double gyre setup, described in detail in Section 2.4. Channel simulations allow us to compare results with the previous works mostly tested on the channel setup (e.g., Juricke et al., 2020). However, it has several disadvantages, such as high variability of area-integrated kinetic energy due to the channel's narrowness or a lack of spatial separation between regions of release and dissipation of energy. As an extension of the idealized channel setup, the double-gyre setup has more defined areas of creation and dissipation of kinetic energy and a longer zonal direction that allows eddies to develop and evolve in space. It also has the advantage of being more intuitively understandable and closer to reality, as it represents the idealized physical processes of subpolar and subtropical gyres in the North Atlantic or North Pacific basins. In addition, the double-gyre setup can be extended to include more complicated coastlines and bottom topography to create an even more realistic representation of basin dynamics.

The outline of the article is as follows. We begin in Section 2 with the model essentials, which include the methodology used to create the new components of the subgrid energy budget for energy backscatter, the description of the two modeling setups that we use to test the implementations and the diagnostics used to investigate the effect of the new components. Section 3 describes the results and improvements achieved in simulations whereas the advection and stochastic components in the UKE, applied independently and simultaneously. The paper closes with discussions and conclusions in Section 4.

2 Model essentials

2.1 Equations of motion

We solve the primitive equations in idealized ocean basins with eddy viscosity and backscatter. The horizontal momentum equation reads

$$\partial_t \boldsymbol{u}_\mathrm{h} + f\,\boldsymbol{e}_z \times \boldsymbol{u}_\mathrm{h} + (\boldsymbol{u}_\mathrm{h} \cdot \boldsymbol{\nabla}_\mathrm{h} + w\partial_z)\boldsymbol{u}_\mathrm{h} + \boldsymbol{\nabla}_\mathrm{h} p/\rho_0 = \boldsymbol{V}(\boldsymbol{u}_\mathrm{h}) + \boldsymbol{B}(\boldsymbol{u}, e) + \partial_z(\nu_v\,\partial_z \boldsymbol{u}_\mathrm{h}) \quad (1)$$

where $\boldsymbol{u} = (u, v, w)$ denotes the full three-dimensional velocity field, $\boldsymbol{u}_\mathrm{h} = (u, v)$ the horizontal velocity field, f the Coriolis parameter, $\boldsymbol{e}_z$ the unit vertical vector, p the pressure, ρ_0 the reference density, $\boldsymbol{V}(\boldsymbol{u}_\mathrm{h})$ the horizontal eddy viscosity, $\boldsymbol{B}(\boldsymbol{u}, e)$ the backscatter operator, described in more detail below, and ν_v the coefficient of vertical viscosity.

The vertical momentum equation reduces to hydrostatic balance in the form

$$\partial_z p = -g\rho = b\rho_0\,, \quad (2)$$

where g is the gravitational acceleration and ρ is the deviation of density from its reference value ρ_0; b denotes buoyancy and will be used in the following.

The equation for an arbitrary tracer takes the form

$$\partial_t T + \boldsymbol{\nabla} \cdot (\boldsymbol{u}T) = \boldsymbol{\nabla}(\boldsymbol{K}\boldsymbol{\nabla}T)\,, \quad (3)$$

where T is a tracer (temperature or salinity) and $\boldsymbol{K}$ is the diffusivity tensor in the form of a symmetric 3×3 matrix that aims at minimal mixing of tracers across surfaces of isoneutral density. We assume the linear form of the equation of state, in particular, density is linearly dependent only on temperature (salinity tracer stays constant in time). In this case, isoneutral $\boldsymbol{K}$ implies no mixing.

The horizontal viscosity operator in Eq. (1) is biharmonic and has the form described in Juricke et al. (2020), which was found to be minimally dissipative for FESOM.

Backscatter tries to reduce over-dissipation by harnessing the inverse cascade. The coefficients of viscous and backscatter parameterizations have opposite signs, and different approaches define their amplitude. Backscatter is based on a subgrid energy budget simulating the kinetic energy available for backscattering into the resolved flow.

Here, as in Jansen et al. (2015) and (Juricke et al., 2019), we use an explicit subgrid energy budget at each grid cell that defines the backscatter coefficient, i.e., the amplitude of local backscatter. The advantage of this approach is that we can explicitly control and model the transfer of energy between different terms of the resolved dynamics and the subgrid. The kinetic energy accumulated on the subgrid, $e = e(x, y, z, t)$, is called *unresolved kinetic energy* (UKE). The particular model for UKE studied by Juricke et al. (2019) is of the general form

$$\partial_t e = -c_{\text{dis}}\,\dot{E}_{\text{dis}} - \dot{E}_{\text{back}} - \boldsymbol{\nabla}\cdot\left(\nu^C\,\boldsymbol{\nabla} e\right). \tag{4}$$

The first term on the right-hand side of the equation is a kinetic energy source diagnosed from the dissipative term in the horizontal momentum equation. c_{dis} is a parameter that represents the share of direct energy cascade to microscales. If c_{dis} is smaller than 1, part of the kinetic energy goes to small scales and is dissipated. $(1 - c_{\text{dis}})$ can be interpreted as a hidden sink term for the flow. The second term $-\dot{E}_{\text{back}}$ is a UKE sink (on average) and represents the rate of energy returned to the resolved flow via the backscatter operator. The last term is UKE harmonic diffusion, which redistributes subgrid energy and has a significantly smaller magnitude when compared to the other terms. ν^C is a diffusion coefficient roughly corresponding to the average eddy thickness diffusivity over the baroclinically forced region according to Jansen et al. (2015) but the amplitude of this coefficient is of minor importance (see also discussion in Juricke et al. (2019).

To reduce the contribution from the grid-scale fluctuations (for a discussion, see Juricke et al. (2019)) and to control the scales at which energy is injected into the momentum equation via backscatter, it is necessary to apply a smoothing filter within the following terms: the UKE source term $\dot{E}_{\text{dis}}$, the backscatter term $\dot{E}_{\text{back}}$, and the backscatter contribution $\boldsymbol{B}(\boldsymbol{u}, e)$ to the momentum equation (Eq. (1)) (the corresponding order of amount of smoothing cycles is specified in Table 1). This is implemented by repeated application of a single averaging operator that averages cell centroid quantities to the common cell vertex and then averages the new vertex quantities back to the cell centroids. The effect of filtering involved in $\boldsymbol{B}(\boldsymbol{u}, e)$ will be analyzed later.

2.2 Deterministic backscatter with advection

In this study, we extend Eq. (4) by incorporating full advection of UKE in three dimensions by the velocity field of the resolved flow. The subgrid energy budget equation with the new term has the following form:

$$\partial_t e = -c_{\text{dis}}\,\dot{E}_{\text{dis}} - \dot{E}_{\text{back}} - \boldsymbol{\nabla}\cdot(\nu^C\boldsymbol{\nabla} e) - \boldsymbol{u}\cdot\boldsymbol{\nabla} e \tag{5}$$

We study the effect of UKE advection using a channel and double-gyre setups described in Section 2.4. The flow in the channel setup is statistically homogeneous in the zonal direction so that the regions of KE production and dissipation coincide. This makes it more challenging to analyze the direct effect of the subgrid advection term on local energy transfers. In the double-gyre setup, these regions are separated, which can help to interpret the effects of UKE advection.

2.3 Stochastic backscatter

The second extension of the subgrid kinetic energy model (Eq. (4)) is an additional stochastic term whose spatial pattern is derived by diagnosing the kinetic energy from a high-resolution reference simulation. It aims to improve the missing spatial and temporal variability.

To generate correlated patterns for the stochastic forcing, we first ran a higher-resolution, 10km simulation and calculated kinetic energy for every mesh element for each simulated day of a 9 year simulation. Then we coarse-grained the field to the eddy-permitting mesh by calculating the average amount of kinetic energy over four neighboring cells. This provides us with a coarse-grained field of high-resolution kinetic energy that can then be used to generate correlation patterns for the stochastic term in the UKE equation.

The coarse-grained high-resolution kinetic energy is then decomposed into empirical orthogonal functions (EOFs) and the corresponding set of principal components (PCs) that reflect the temporal dynamics of each EOF, where we retain only the EOF patterns with the largest contribution to the total variance. Here, we choose the cutoff at 50% of the total variance, thereby reducing the number of EOFs from thousands to dozens.

We also attempted to use data on the difference between coarse and fine resolution runs for the EOF decomposition (see Section 3.7 for more information) but decided against it due to the higher computational expense and the lack of a clear physical argument in favor.

Based on this decomposition, we introduce a new stochastic term in the subgrid energy equation (Eq. (4)), which now reads

$$\partial_t e = -c_{\mathrm{dis}}\, \dot{E}_{\mathrm{dis}} - \dot{E}_{\mathrm{back}} - \boldsymbol{\nabla} \cdot (\nu^C \boldsymbol{\nabla} e) + C_1\, e \sum_i \mathrm{EOF}_i(x)\ \mathrm{PC}_i(t)\,. \tag{6}$$

The summation is over i, the ordinal number of the EOF. The corresponding PCs follow Ornstein–Uhlenbeck processes

$$\mathrm{d}\,\mathrm{PC}_i = -\mu_i\ \mathrm{PC}_i\ \mathrm{d}t + \sigma\, \mathrm{d}W_i\,, \tag{7}$$

where the $\mathrm{d}W$ is an increment of the standard Wiener process and the mean reversion rates μ_i are determined by fitting the Euler–Maruyama discretization of Eq. (7), which is an AR(1) process, to daily mean data. For simplicity, the variance parameter σ is taken the same across all the PC_i, and is absorbed into the tuning parameter C_1 which is further discussed in Section 3. To generate realizations for a model run, the stochastic equation is again converted into a time-discrete AR(1) process, but with the actual model time step. Finally, the prefactor e in Eq. (6) is a heuristic choice, corresponding to multiplicative noise in order to avoid over-energizing the calm areas of the flow where the subgrid energy is low.

In Section 3, the effect of the implementations described above will be compared to the impact of the older version of the UKE budget for kinetic energy backscatter following Juricke et al. (2019) (Eq. (4)). The latter already substantially improves the mean state. Despite the general capacity of the backscatter to inject as much kinetic energy as we want, the subgrid is designed to limit this amount of energy input. With stochastic forcing in the subgrid, we could continue to increase the amount of input arbitrarily. However, it will not necessarily make a simulation closer to the high-resolution truth but more energetic and model stability may become an issue. Therefore, the diagnostics introduced in Section 2.7 and the tuning of C_1 focus not only on the mean kinetic energy but also on other flow variables and their variability in order to capture the overall effect of the addition of the stochastic term as part of the UKE budget.

2.4 Simulation setups

We use two different setups of the FESOM2 model, which solves the primitive equations on a quasi-B-grid. The surface mesh is triangular, and there are 40 vertical layers, with layer depth varying from 9 m in the top layer to 370 m in the bottom layer, which divide the domain into small triangular prisms. Both setups are bounded vertically by a flat bottom at a depth of 4000 m. The bottom boundary conditions are taken as linear friction. The viscous operator is a discrete biharmonic operator depending on the difference in velocities between neighboring elements following the formula $\nu_{c'c} = \gamma_0 l_{c'c} + \gamma_1 |\boldsymbol{u}_{c'} - \boldsymbol{u}_c| l_{c'c} + \gamma_2 |\boldsymbol{u}_{c'} - \boldsymbol{u}_c|^2 l_{c'c}$, where c and c' are the neighboring grid cells, $l_{c'c}$ is the length of the edge between the cells, and γ_0, γ_1, γ_2 are the tuning coefficients (for more details see (Juricke et al., 2020)). We use the PP vertical mixing scheme (Pacanowski & Philander, 1981) for both setups. For a discussion of alternative mixing schemes, see Scholz et al. (2022).

The first of two test configurations is a zonally periodic channel following Soufflet et al. (2016). The size of the channel is 4.5° (about 500 km) in the zonal direction and 18° (about 2000 km) in the meridional direction.

The initial density profile changes gradually along the meridional direction as well as vertically (Fig. 2a). It is directly associated with the temperature gradient by a linear equation of state. The gradient allows the model to form a jet in the middle of the channel. To continuously maintain a quasi-stationary turbulent regime, the zonally averaged velocity and temperature fields are relaxed to the initial mean temperature and velocity state in the entire domain.

The Rossby radius of deformation (approximately 20 km in the center and ±5 km from south to north) is governed by the predefined vertical stratification to which the model is relaxed. Thus, we choose a coarse grid consisting of equilateral triangles with 20 km edge length, which is eddy-permitting, and a fine grid where the edge length is 10 km thus (barely) eddy-resolving (see Fig. 1a,b).

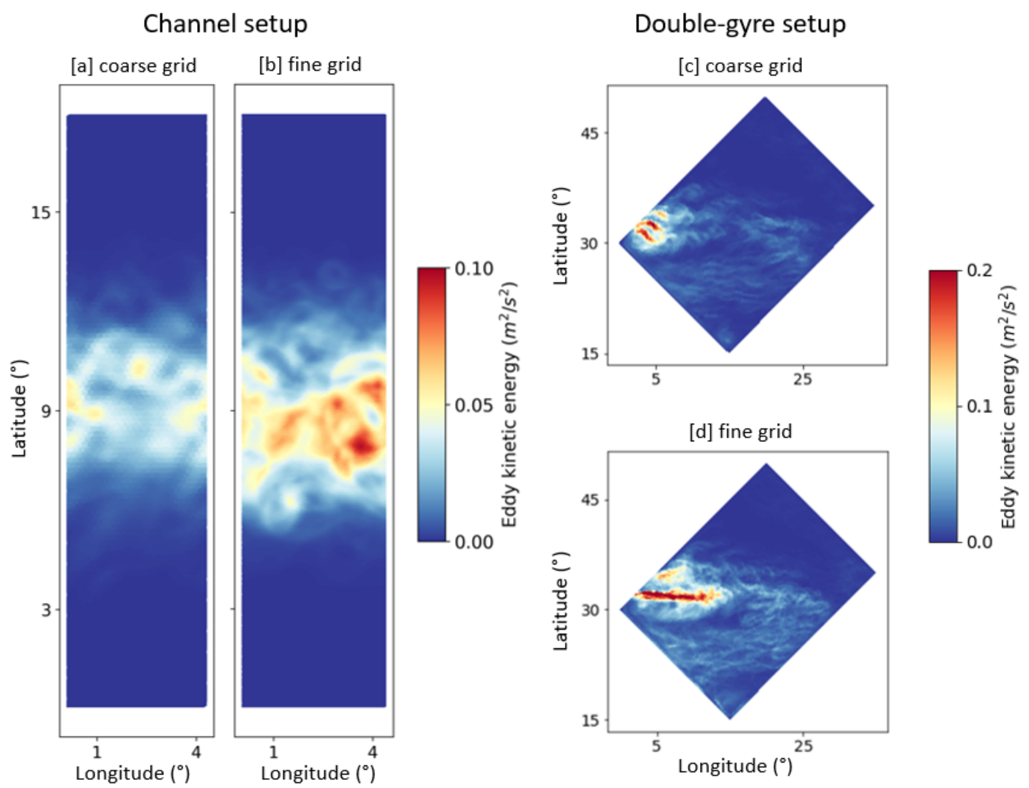

Figure 1. Channel (a,b) and double-gyre (c,d) setups. Annual-mean EKE $[m^2/s^2]$ (after spin-up) for the coarse grid simulation (a,c) and for the fine grid simulation (b,d), which was determined by the formula: $\frac{\overline{u^2}+\overline{v^2}-\overline{u}^2-\overline{v}^2}{2}$. Aerial view of the surface layer.

The second setup follows Levy et al. (2010) and represents a double-gyre configuration, from now on referred to as the DG setup. It uses a rectangular domain with its left corner at 30°N, rotated by 45°. The size of the domain is 28.3° (about 3140 km) on the long side and 21.2° (about 2350 km) on the short side. Vertical walls bound it on all four sides. Here, we use a mesh formed of right-angled triangles instead of equilateral triangles to avoid castellated boundaries. The short sides of the right-angled triangles are equal to 20 km and 10 km, corresponding to the coarse and the high-resolution simulations.

The initial temperature profile follows Pacanowski and Philander (1981) and Levy et al. (2010). It is rapidly nonlinearly decreasing from the surface to a depth of 500 m and slowly linearly decreasing to 0 °C below (Fig. 2b). There is no initial meridional temperature stratification. The initial vertical temperature stratification adjusts during the simulation based on forcing and internal mixing, but due to the depth of the setup, this process takes several decades. Surface forcing is based on a mean northern hemisphere wind stress (Fig. A1b) and heat flux. Wind forcing is an essential flow driver through Ekman pumping. A sinusoidal wind stress profile forces a subpolar gyre in the north and a subtropical gyre in the south, thereby imitating North Atlantic dynamics. The heat flux can be divided into several components, i.e. latent, sensible, and radiative heat flux (Levy et al., 2010). As a simplification, we only use sensible and radiative heat fluxes here. Both enter the surface directly, while radiative heating is also distributed vertically over the first couple of layers according to a solar penetration profile. The heat fluxes then further update the tracer equation via diffusion and mixing. The exact sensible heat flux expression used in the simulation is $-\gamma(T_{\text{ocean}} - T_{\text{atm}})$, where γ is a transfer coefficient and shall be taken to be equal to $4\,\mathrm{W\,m^{-2}\,K^{-1}}$, T_{ocean} - sea surface temperature, and T_{atm} - apparent air temperature (Fig. A1a). The solar radiation model (Fig. A1c) takes losses due to cloudiness, reflection and albedo into account. Latent heat flux due to evaporation is neglected, and so is any freshwater flux (i.e., salinity is constant).

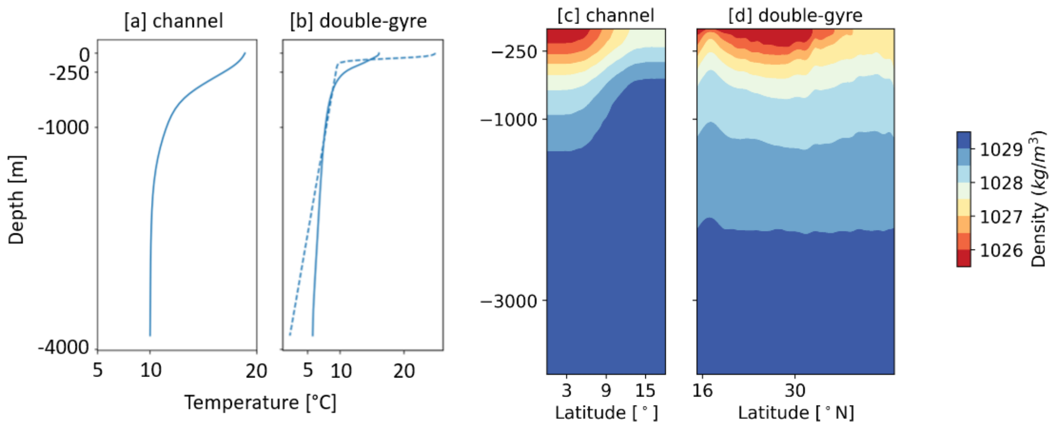

Figure 2. Vertical temperature and density profiles. Panel (a) shows the initial vertical temperature stratification in the channel, while panel (b) displays both the initial (dashed line) and equilibrium (solid line) vertical temperature stratification in the double-gyre setup. Panel (c) shows the annual mean of the vertical density profile along 2.5° longitude in the channel, and panel (d) shows the annual mean of the vertical density profile along 15° longitude in the double-gyre setup after spin-up.

We use cartesian geometry for the channel setup (i.e., we replace the cosine of latitude by one) and spherical geometry for the double-gyre simulation. For the Coriolis parameter, we use the β-plane approximation $f = f_0 - \beta d$, where d is the meridional distance from the zero-degree latitude. The constants here and above are chosen to agree with those originally proposed for these test cases, and are specified in Table A1.

Fig. 2c,d show the stratification of both setups. It is evident that the double gyre has a more complex vertical stratification that changes with integration time until it reaches a (quasi-)equilibrium state, while for the channel, stratification is continuously relaxed back to the initial state.

2.5 How much filtering is necessary?

The use of filters as described in Section 2.1 raises the question of whether shielding the system from small-scale noise could interfere with the impact of the subgrid advection term as advection and smoothing both affect where and at which scales energy is reinjected. In this context, we also want to revisit the question of how much smoothing is really necessary to ensure sufficient scale separation between injection and dissipation range for the energy cascade. Thus, we ran additional simulations, where we reduced the number of filter cycles for the contribution of backscatter in the momentum equation to zero (i.e., in $\boldsymbol{B}(\boldsymbol{u}, e)$ in Eq. 1). We ran these tests with and without subgrid advection.

2.6 Spin-up

Both setups start with appropriate temperature stratification and a small initial perturbation, which leads to the emergence of turbulence in a short time, as evidenced by the growth of kinetic energy over the first year (Fig. 3) and by the presence of eddies in the vorticity field (not shown).

The channel simulation reaches a statistically steady state after a little more than one year, maintained by the relaxation of the velocity and temperature fields. For our diagnostics, we thus take nine years after a single spin-up year. In the DG setup, isopycnals become inclined because of Ekman pumping in the southern part of the domain and Ekman suction in the northern part of the domain as a consequence of the sinusoidal wind forcing. This process is much slower, so we require a 50-year spin-up to reach a quasi-equilibrium state.

Besides the difference in spin-up time, Fig. 3 also indicates different levels of surface KE fluctuation between the two setups. The comparatively larger fluctuations in the channel vs. double-gyre are explained by the fact that the channel is narrow in the zonal direction and, therefore, cannot host many eddies simultaneously. As a result, the resolved EKE fluctuates greatly along the eddy life cycles. To minimize the fluctuation effect, we use 9-year averaging for both setups, i.e., a simulation length of 9 years after the respective spin-up.

Overall, we use the DG setup as an extension of the idealized zonally-periodic channel setup as it has better-defined areas of creation and dissipation of kinetic energy and is longer in the zonal direction, which allows eddies to develop and evolve in space. In addition, the DG setup could be extended to include more complicated and realistic coastlines and bottom topography. One of our aims is to understand how the complexity of the setup influences the effectiveness of the default backscatter of Eq. (4) itself and the new subgrid energy components of Eqs. (5) and (6) implemented in this study.

2.7 Diagnostics

We examine a set of mean quantities calculated for each vertical layer z to diagnose the effect of our changes in the subgrid equation. As a main diagnostic, we use vertical profiles of the area-averaged layer-wise mean eddy kinetic energy

$$\mathrm{EKE}(z) = \overline{\sum_i \tfrac{1}{2}\left((u(z) - \overline{u(z)})_i^2 + (v(z) - \overline{v(z)})_i^2\right) A_i \Big/ \sum_i A_i}\,, \tag{8}$$

where A_i denotes the area of grid cell i, and the overbar denotes the time average of 9 years. We also examine the vertical profiles of the root mean square of vertical velocity anomalies,

$$w_{\mathrm{RMS}}(z) = \sqrt{\overline{\sum_j (w(z) - \overline{w(z)})_j^2 \, B_j \Big/ \sum_j B_i}} \tag{9}$$

where j denotes the vertex index and B_j is the area of the median-dual cell associated with vertex j. As they show the amplitude of the time-averaged vertical velocity fluctuations

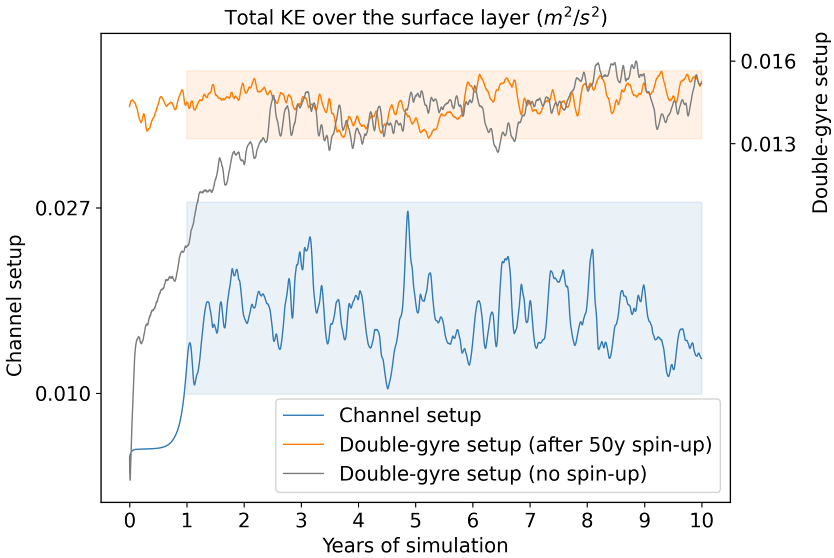

Figure 3. The variability of total surface kinetic energy over time. The blue line represents a 10-year simulation of the channel setup. The highlighted solid blue box indicates the 9 years chosen for analysis, excluding the first spin-up year. After a 50-year spin-up, the orange line corresponds to the double-gyre setup, with the 9 years chosen for analysis indicated by a solid orange box. The grey line indicates the amplitude of the initial drift of the double-gyre setup.

for each vertical layer, they enable the detection of vertical fluctuation anomalies that may appear due to the wrong viscosity and backscatter settings. The different cell areas in Eq. (8) vs. (9) arise because in FESOM2, scalars and pressure are located on vertices while horizontal velocities are located on centroids. Lastly, vertical profiles of buoyancy flux, which characterizes the vertical profile of the release of APE, are computed as

$$\overline{w'\,b'(z)} = \overline{\sum_j (w(z) - \overline{w(z)})_j\,(b(z) - \overline{b(z)})_j\,B_j \Big/ \sum_j B_j}\,. \tag{10}$$

An abnormal change in RMS vertical velocity (Eq. (9)) and in the structure of APE release (Eq. (10)) could indicate an excitation of nonphysical waves, or otherwise changing stratification and dynamics (as is often seen when varying the grid resolution).

Taking the scalar product of the horizontal momentum equation (Eq. (1)) with $\boldsymbol{u}_\mathrm{h}$, we obtain an evolution equation for the (horizontal) kinetic energy density,

$$\frac{1}{2}\partial_t|\boldsymbol{u}_\mathrm{h}|^2 = -\boldsymbol{u}_\mathrm{h}\cdot(\boldsymbol{u}_\mathrm{h}\cdot\boldsymbol{\nabla}_\mathrm{h})\boldsymbol{u}_\mathrm{h} - \frac{1}{\rho_0}\boldsymbol{u}_\mathrm{h}\cdot\boldsymbol{\nabla}_\mathrm{h}p + \boldsymbol{u}_\mathrm{h}\cdot\boldsymbol{V}(\boldsymbol{u}_\mathrm{h}) + \boldsymbol{u}_\mathrm{h}\cdot\partial_z(\nu_v\,\partial_z\boldsymbol{u}_\mathrm{h})\,. \tag{11}$$

The pressure gradient work term $-\frac{1}{\rho_0}\boldsymbol{u}_\mathrm{h}\cdot\boldsymbol{\nabla}_\mathrm{h}p$ is the source term for the integrated kinetic energy. In the case of the DG setup, wind forcing is either a source or a sink and comes to the system via the last term in Eq. (11). In the case of the channel setup, the relaxation of the zonal mean profile to the prescribed one acts as a source for mean KE.

Integrating the three-dimensional pressure work term over a volume, using incompressibility and hydrostatic balance (Eq. (2)), we obtain

$$\frac{1}{\rho_0}\boldsymbol{u}_\mathrm{h}\cdot\boldsymbol{\nabla}_\mathrm{h}p = \nabla(\boldsymbol{u}p) + wb\,. \tag{12}$$

Integrating over some domain, the divergence term on the RHS of Eq. (12) becomes less important, and it will be zero if one integrates over the entire flow domain (no pressure flux through the boundaries).

A similar expression holds for the anomalous, i.e., eddy part of the pressure gradient work and buoyancy flux. In this study, we focus on the eddy part $w' b'$ and take it as a local diagnostic for the transfer from APE to KE even though, strictly speaking, it only holds in an (sufficiently large) area-integrated sense.

As an essential part of diagnostics, we compute the horizontal power spectra of the different contributions to the viscous and backscatter parameterizations. In order to use the discrete Fourier transform, we interpolated first to a regular quadrilateral grid. Then the 2D spectra are condensed to 1D spectra by integrating over an annulus of unit width in wavenumber space. Here, we apply cubic interpolation for kinetic energy and nearest-neighbor interpolation for the dissipation power following the results of Juricke et al. (2023), motivated by the smooth nature of the kinetic energy field and the non-smooth, discrete representation of the dissipation and backscatter operators.

The DG setup was simulated and calculated, assuming a spherical geometry. Hence, it was necessary to convert the grid and vector fields into Cartesian coordinates before performing interpolation. We first transformed the mesh and velocities to a new spherical system of coordinates such that the center of the domain is at the equator. After this transformation, we selected the central rectangular area of the domain (see the box in Fig. 4) for further interpolation and Fourier transform.

Spectra are computed as an average of the daily output for nine years and limited horizontally by the wavenumber π/h, where h is the height of an equilateral grid triangle (see discussion in Juricke et al., 2023). h_c is the height of the coarse grid triangle, and h_f is the height of the fine grid triangle in the channel. In the case of the DG setup, one should stop at the wavelength of $2h$, i.e., wavenumber π/h, where h is the smaller side. The limiting wavenumber depends on direction: it is π/h along small sides and $\sqrt{2}\pi/h$ in the direction along and perpendicular to the large side. Since we are willing to discuss spectra averaged over angles, we have to stop at π/h.

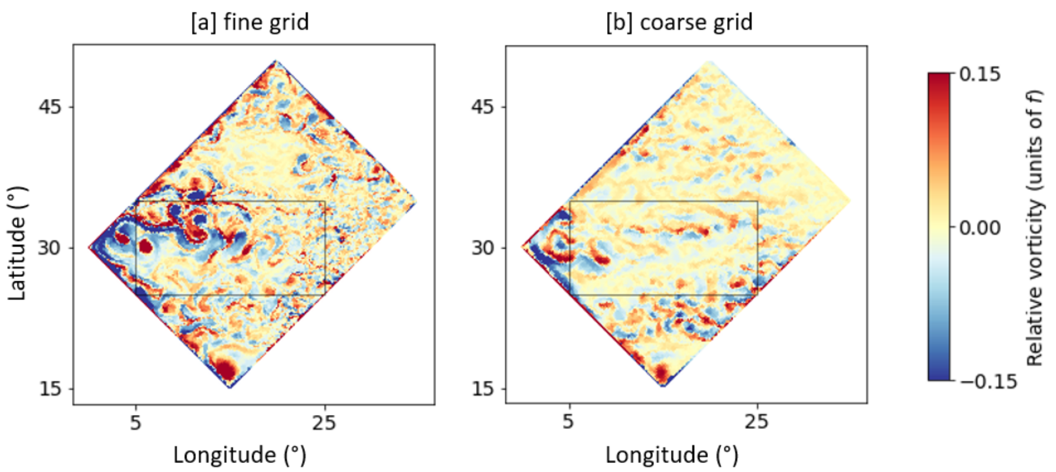

Figure 4. A snapshot of the relative vorticity in the double-gyre setup, showing the designated area for Fourier decomposition (black box).

As a final diagnostics, here specifically for the DG setup, we evaluate vertical density profiles. As mesoscale eddy parameterizations ultimately strive to reproduce a precise representation of the ocean stratification, we examine the alignment of the isopycnal contours with those of the reference simulation.

3 Results

3.1 Matrix of numerical experiments

We performed a matrix of simulations where we tested the different parameterization choices introduced in Section 2 for each of the setups. A summary of simulations is given in Table 1. The 10 km simulation is the high-resolution reference, the 20 km is the low-resolution reference without backscatter. Both use biharmonic viscosity with a variable coefficient designed to dissipate grid scale motion following Juricke et al. (2020). The other simulations are also on the low-resolution 20 km grid and include backscatter with and without the advection and stochastic terms.

Table 1. An overview of the essential parameters for the simulation setups. Δx is a side of an equilateral grid triangle for the channel simulation. For the double-gyre simulation, Δx corresponds to the smallest side of a right-angled grid triangle.

Simulation name	Δx (km)	Smoothing cycles	Backscatter	Subgrid advection	Stochastic backscatter amplitude
20 km	20	(2,2,4)	no	no	no
20 km+BS	20	(2,2,4)	deterministic	no	no
20 km+BS (no BS filter)	20	(2,2,0)	deterministic	no	no
20 km+BS+ADV	20	(2,2,4)	deterministic	yes	no
20 km+BS+ADV (no BS filter)	20	(2,2,0)	deterministic	yes	no
20 km+SBS (high)	20	(2,2,4)	stochastic	no	high
20 km+SBS (middle)	20	(2,2,4)	stochastic	no	middle
20 km+SBS (low)	20	(2,2,4)	stochastic	no	low
20 km+SBS (middle)+ADV	20	(2,2,4)	stochastic	yes	middle
20 km+SBS (low)+ADV	20	(2,2,4)	stochastic	yes	low
10 km	10	(2,2,4)	no	no	no

3.2 Eddy-permitting simulations are overdissipative

To assess the effects of incorporating the new components into the subgrid energy budget, we first look at changes in eddy kinetic energy (Fig. 5a,b) for the simulations that only have the viscosity parameterization. Comparing the simulation results for "20 km" (grey line) and "10 km" (black line), we observe that the low-resolution simulation has a significant EKE deficit for the DG, even more than in the channel.

Variability of the vertical velocity also differs greatly between the two resolutions (Fig. 5c,d), but here with opposite tendencies between the two setups. For the DG, vertical fluctuations at low resolution are larger, while it is the opposite for the channel, but also located at greater depth as compared to the high-resolution reference.

Buoyancy fluxes, which serve as an indicator of APE release, are substantially reduced at low resolution for both simulations (Fig. 5e,f), especially the near-surface peak is much weaker. In the DG setup, moreover, a significant reduction of energy production is observed along the entire water column.

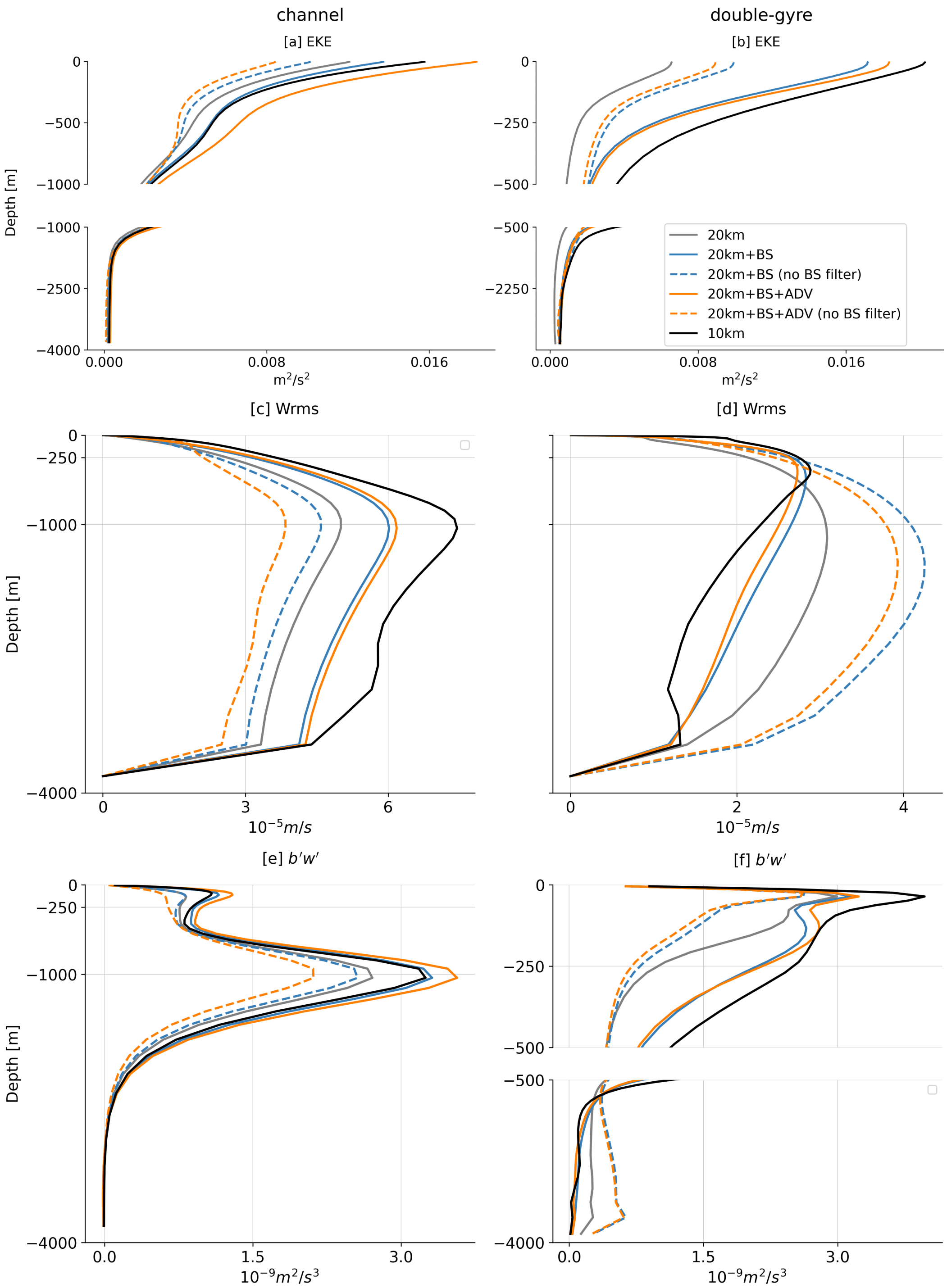

Figure 5. Vertical profiles for the channel setup (left column) and the double-gyre setup (right column). Each setup includes layer and time-averaged (9 years) diagnostics for EKE [m^2/s^2] (a, b), the RMS vertical velocity anomalies [m/s] (c,d), and buoyancy flux [m^2/s^3] (e,f). Figures a, b, and f have a gap on the vertical axis.

3.3 Dynamic backscatter improves the energy cycle

We first switch on dynamic backscatter as in Juricke et al. (2019). This improves all diagnostics on the coarse grid toward the values on the fine grid (solid blue line in Fig. 5).

We note, in particular, that the point of maximum vertical velocity variability in the DG setup moves closer to the surface, as it should (Fig. 5d). Moreover, the upper part of the buoyancy flux profile for the channel becomes more distinct with backscatter, hence agreeing with Soufflet et al. (2016) who observe a dominant peak (due to mesoscale instability) at 1000 m depth and a secondary isolated peak (due to submesoscale instability) closer to the surface. For the DG setup, mesoscale production is the most improved (Fig. 5f).

3.4 Impacts of advection of subgrid energy

When the advection term is included in the subgrid equation, it improves the backscatter effect, bringing it even closer to the high-resolution truth for both setups (solid orange line on Fig. 5a,b). For the channel setup, subgrid advection increases EKE beyond what is observed in the 10 km reference. This is not necessarily a negative result because we do not resolve the full eddying flow even at 10 km resolution (Soufflet et al., 2016).

For both setups, the presence of advection in the subgrid correctly shifts the profile of RMS vertical velocity to the direction of the high-resolution truth, although the amplitude of the shift is small (Fig. 5c,d). The profile of RMS vertical velocity is a convenient diagnostic of instabilities in the deep ocean. Such instabilities may occur when background viscosity is too small (see Juricke et al. (2020). Here, we do not see any indication of the onset of instability, with or without subgrid advection. In the DG, vertical velocity variability even decreases when advection is included, which indicates that subgrid advection does not induce spurious waves. At the same time, subgrid advection *enhances* the production of APE near the peaks (Fig. 5e,f), thereby reducing biases in energy production.

We conclude, based on the vertical profile diagnostics, that adding the advection term to the subgrid equation has a positive effect, with different changes depending on the setup.

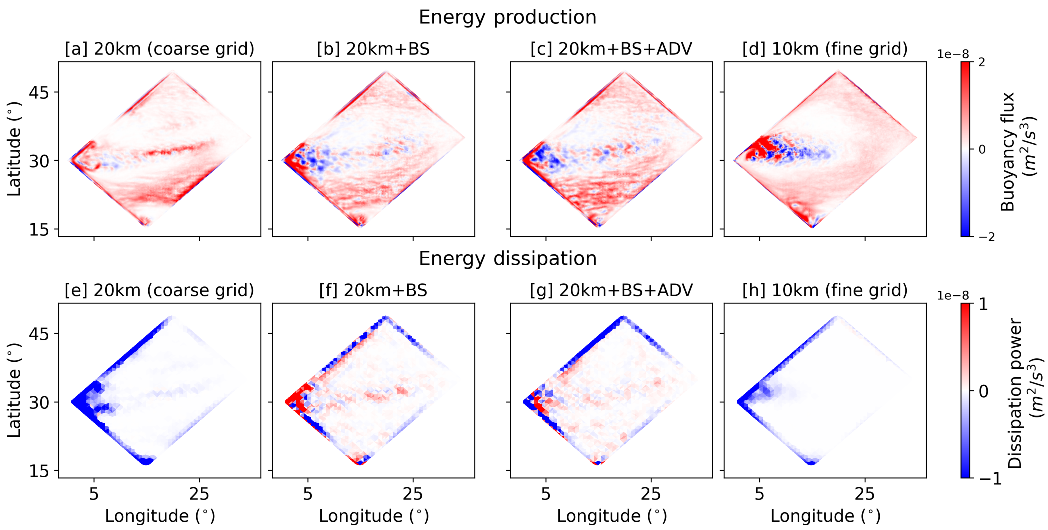

Figure 6. The 9-year average of 2D buoyancy flux $[m^2/s^3]$ (a-d) and the 9-year average of the dissipation power $[m^2/s^3]$ (e-h) computed as the dot product of the velocity field and its dissipation tendency. The dissipation field is also coarse-grained to the 100 km grid. Plots are provided for the following DG configurations: coarse resolution simulation (a,e), coarse resolution with deterministic backscatter (b,f), coarse resolution with deterministic backscatter and subgrid advection (c,g), and fine resolution simulation (d,h).

This conclusion is supported qualitatively by a two-dimensional horizontal view of the production term, see Fig. 6, which shows the buoyancy flux at the maximum level and the dissipation power on the surface level for the different configurations. Both diagnostic fields exhibit significant fluctuations. In order to better distinguish between areas of dissipation and anti-dissipation, we conservatively remapped the dissipation field to a coarse mesh with 100 km resolution. Due to subgrid advection, the central jet's energy production areas are extended, reaching further into the jet domain, albeit the jet is in the wrong position compared to the high-resolution simulation (Fig. 6c). Additionally, subgrid advection prevents backscatter work in the border layer, as demonstrated in Fig. 6g. With the addition of advection, backscatter now focuses primarily on the eddy regions within the domain, resulting in a more physical process representation.

3.5 Spectral diagnostics

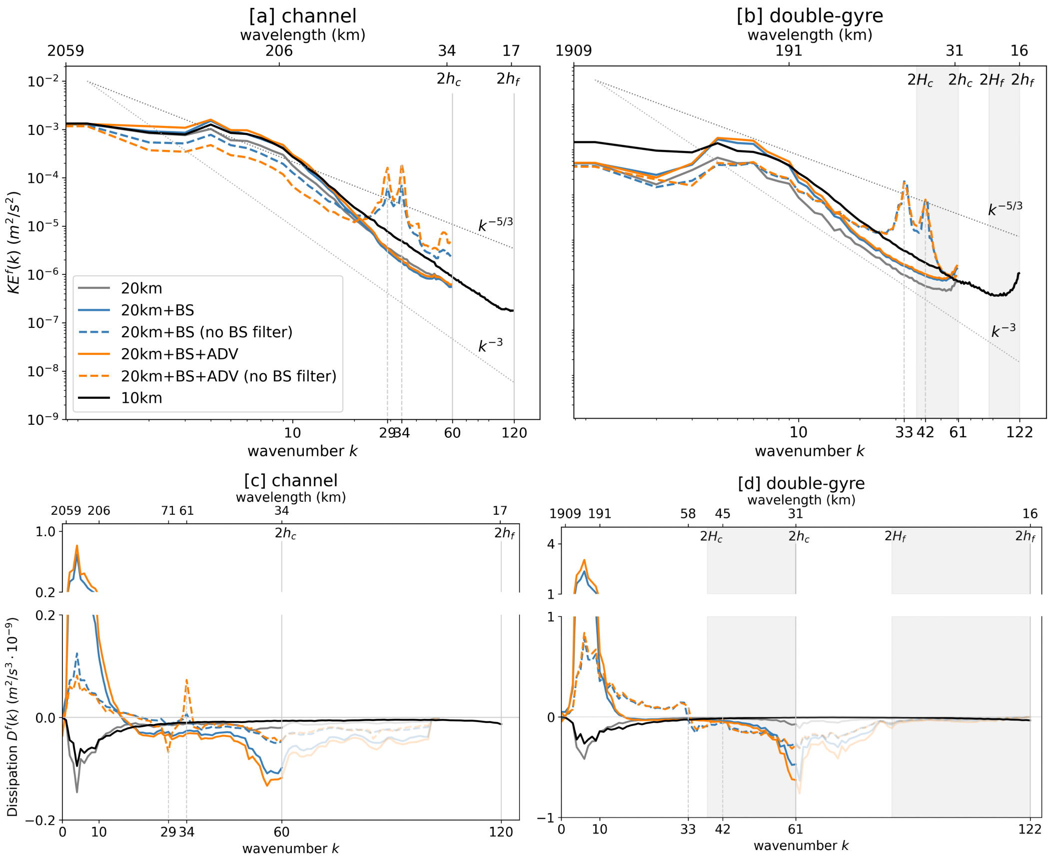

Figure 7. Kinetic energy and dissipation spectra for the channel and DG setups average over 9 years. The vertical lines show the largest wavenumbers (smallest wavelength) on coarse and fine meshes.

Spectral diagnostics of EKE (Fig. 7a,b) show the expected scalings (i.e., $-5/3$ and -3) are in some ranges of wavenumbers, and a relatively early (i.e., at low wavenumbers) deviation from these spectral slopes in the 20 km simulation without backscatter. Backscatter significantly increases the energy level, especially at mid-range without adding much energy to the small scales (which is generally not desirable for reasons of numerical stability). Including advection results in a minor positive change to KE across all scales. For channel, a rather close agreement is reached between the simulations with backscatter and high-resolution simulation (and slightly overperforms after adding subgrid advection). For the DG, the level of KE is still deficient at very small and large scales, even with subgrid advection.

In all DG simulations, one can observe a spectral density pile up near the finest grid scale ($2h_c$). While this is generally seen as related to insufficient dissipation, the same effect can be observed in channel simulations when considering the finest grid scale and has been (at least partially) identified as an artifact of the interpolation from the triangular to a rectangular grid when computing Fourier spectra (Juricke et al., 2023).

Dissipation power spectra (Fig. 7c,d) show the total dissipation (in the case of simulations with the purely viscous closure without backscatter) or the sum of total dissipation and backscatter (in the case of simulations with backscatter) across scales. One might expect that viscous dissipation is concentrated at small scales. However, if the resolution is insufficient, it affects all scales and peaks at scales where the energy content is maximal (also see the discussion in Soufflet et al., 2016). On the other hand, backscatter has a distinct injection maximum at large scales and a dissipation maximum at small scales. The points where the dissipation power spectrum crosses the k-axis mark the scales at which there is a change from energy dissipation to energy injection. When there are more smoothing cycles, the point of intersection moves towards larger scales. Conversely, reducing smoothing causes the intersection point to shift towards smaller scales. The 20 km simulation without backscatter is more dissipative than the 10 km, and the influence of dissipation is mostly at the long-wave part of the spectrum. This changes completely with backscatter: energy is injected on large scales, propagates in both directions of the energy cascade, and actively dissipates along the direct cascade on smaller scales. We observe that the added subgrid advection component enhances the backscatter effect on the large scales and dissipation near the grid scales. Subgrid advection acts as a field catalyst, increasing total kinetic energy and total (positive and negative) dissipation over the full range of scales. It does not, however, noticeably affect the scale at which the overall dissipation (small scales) changes to backscatter (large scales).

3.6 Sufficient filtering is important

Insufficient backscatter smoothing causes significant deviations for all diagnostics. When disabling the filter in the backscatter operator, we observe a loss of energy for all simulations (dashed lines in Fig. 5a,b,c,d). For the channel, the performance is even worse than the 20 km simulation without backscatter (Fig. 5a,b). Concerning vertical velocity (Fig. 5c,d), it either substantially enhances variability (DG) or reduces it (channel). We also observed significant unphysical fluctuations on small scales in the energy spectra (Fig. 7a,b). The further detrimental impact of insufficient smoothing is seen in snapshots of the vorticity fields: Eddies and filaments get a highly distorted "patchy" structure and do not propagate in a physically fully coherent way (not shown).

The simulations with insufficient backscatter filtering illustrate the minimal scales where non-smoothed backscatter injects energy into the system. In the case of the channel setup (Fig. 7c), we observe the additional isolated peaks of energy injection (wave number 34) and energy dissipation (wave number 29). They coincide with the double peaks in KE (Fig. 7a). The general nature of the two kinetic energy peaks (consistent between the setups) can only be speculated at this point but may relate to the formulation or filtering of the subgrid, which determines the backscatter coefficient or, most likely, they are a product of the procedure of collapsing spectra from 2D to 1D, where different directions in the grid may show up as two peaks.

We do not exclude the potential interference between the role of advection and the degree of backscatter operator smoothing, as both affect the locality of the backscatter parameterization. However, insufficient scale separation between dissipation and backscatter causes serious flow deviations and is an inadequate parameterization option for FESOM2. At this point, a generalization to other grid types regarding smoothing can not be made.

3.7 EOF analysis

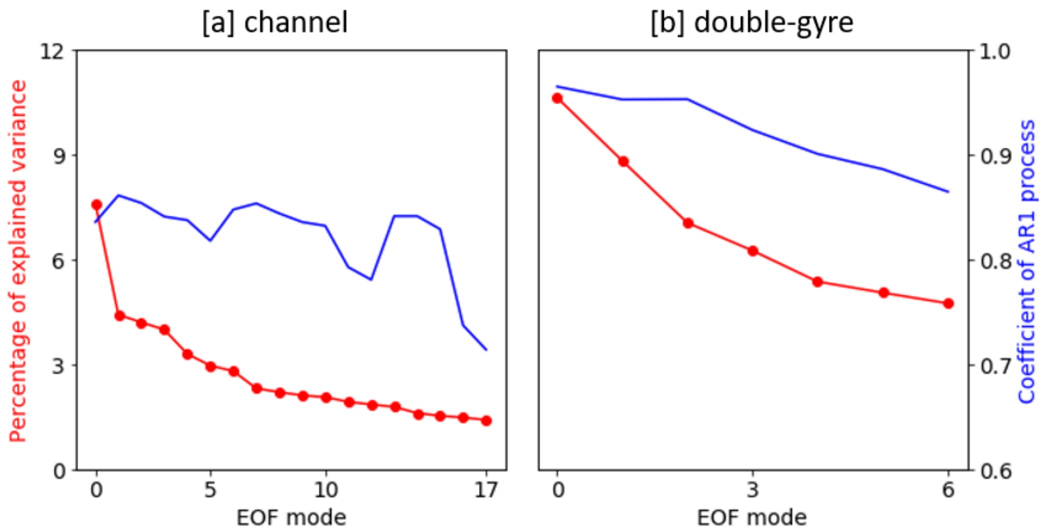

Figure 8. The explained variance and the fitted coefficient for the AR(1) process are listed for each EOF mode.

The first EOFs of the kinetic energy of the high-resolution simulation correspond to the highest variability of KE and are determined by the fluctuations of the mean flow. The presence of a strong localized jet in the DG setup allows the first few EOFs to be relatively large-scale and to capture a large part of the variability in KE, whereas the removed mean flow variability of the channel setup makes the first EOFs already much more small-scale. Constructing the spatial correlation of the stochastic subgrid term based on EOFs with very fine local structures can excite undesirable noise. This needs to be kept in mind and treated with caution. To explain a reference percentage of variability (i.e., 50% in our case), one needs to consider 18 EOFs for the channel setup and only 7 EOFs for the DG setup (see Fig. 8). The reduction of the fitted coefficients of the autoregression process for the corresponding PC accompanies the decrease in the explainable capacity of the EOFs. We are getting shorter correlation times for the higher EOFs with patterns of smaller scales.

As an alternative approach, we also calculated the kinetic energy difference between the coarse-grained data and the output of a coarse-resolution simulation instead of just the pure coarse-grained high-resolution kinetic energy. Through this second approach, we could take the systematic differences in kinetic energy between the outputs of simulations with different resolutions to generate meaningful EOF patterns of missing kinetic energy variability. In the following, however, we will focus on the initial approach, i.e., the patterns generated directly from the kinetic energy data of the coarse-grained high-resolution data. The reason for this is that for the second approach, it was necessary to keep substantially more EOF modes (more than twice as many) to retain 50% of variability, leading to a much more small-scale structure of stochastic forcing patterns that could potentially cause model instabilities and undesired excitation of grid-scale noise. Another reason is that eddy formation differs between high and coarse resolutions. For instance, a large eddy in high resolution does not always align with the eddy pattern observed in coarse resolution, as examined in the analysis of relative vorticity dynamics (not shown). Thus, we have not found enough reasons to alter our method of selecting data, but other options on how to create the EOF patterns are possible.

3.8 Impact of the stochastic subgrid energy source

Based on the magnitude of the other terms in the subgrid energy equation, we selected three options for the coefficient C_1 in Eq. (4): $C_1 = 0.001$, which corresponds to "low"-intensity noise (simulation "20 km+SBS(low)"), $C_1 = 0.005$ corresponding to "middle"-intensity noise (simulation "20 km+SBS(middle)"), and $C_1 = 0.01$ (channel) or $C_1 = 0.008$ (DG) corresponding to the maximum amplitude that does not cause the model to become numerically unstable ("20 km+SBS(high)").

The first result of our simulations is that we can significantly enhance the model's kinetic energy levels via stochastic backscatter while preserving stability. We observe the energizing of the surface layers in the vertical energy profiles (Fig. 9a,b) for all noise categories and, in particular, the energy increase beyond the reference simulation for the "strong" noise. We also find a good agreement of kinetic energy in the reference simulation for the spectra at large scales (Fig. 10), which indicates that we are able (at least partially) to reproduce the spectral slope using the stochastic subgrid energy equation. On the other hand, the vertical energy profile shows unphysical energy growth in the lower layers of the model when using the "strong" stochastic term. It is possible that a more careful tuning of the amplitude as a function of z might mitigate this problem. However, this would be at the expense of introducing yet more tuning parameters so that we restrict ourselves to testing with the stated form of multiplicative noise with simple amplitude tuning. Diagnostics of vertical velocity anomalies (Fig. 9c,d) reveals that, especially in the case of the channel setup, the high-amplitude stochastic term doesn't reflect the ocean behavior at depth, and therefore, this amplitude is outside of the possible range.

Snapshots of relative vorticity for the DG (Fig. 11) show that stochastic backscatter energizes the field with eddies, especially along the jet area. However, we observe increased eddy activity in the northern part of the DG domain that does not correspond to the high-resolution truth. This effect can be caused by insufficient EOF selection, poor fitting of the principal components, a locally overly large noise amplitude, or by the performance of the EOF approach itself.

We nevertheless confirmed the presence of additional eddy dynamics along the jet (see Fig. 11d,e) and an improvement of the kinetic energy spectra curve across the full range of scales (see Fig. 10). Our concern about near-grid-scale noise caused by the stochastic component was not confirmed for the DG setup.

The results for the channel setup showed a worse performance of the EOF approach: we obtained small-scale growth of kinetic energy (Fig. 10a), which could be explained as a spurious wave generation caused by the stochastic backscatter. Thus, the robustness of the stochastic component, in particular, depends on the flow characteristics and noise amplitude of extracted EOF patterns, which should be sufficiently large-scale. This property was also validated when analyzing the simulations using not total high-resolution KE data but the data of KE difference between two resolutions. In this case, the model diagnostics showed a worsening in energetics compared to the high-resolution KE-based EOFs and the relative vorticity field (not shown).

3.9 Combined effect of subgrid advection and stochastic forcing

Our final set of simulations assesses the combined effect of stochastic and advection subgrid terms. Global diagnostics are summarized in Table 2. It shows generally favorable improvements when using some form of backscatter and, in particular, reasonable performance when using both new subgrid terms together. However, it is difficult to pick a clear winner. We therefore turn to discuss further: SSH differences as well as vertical density

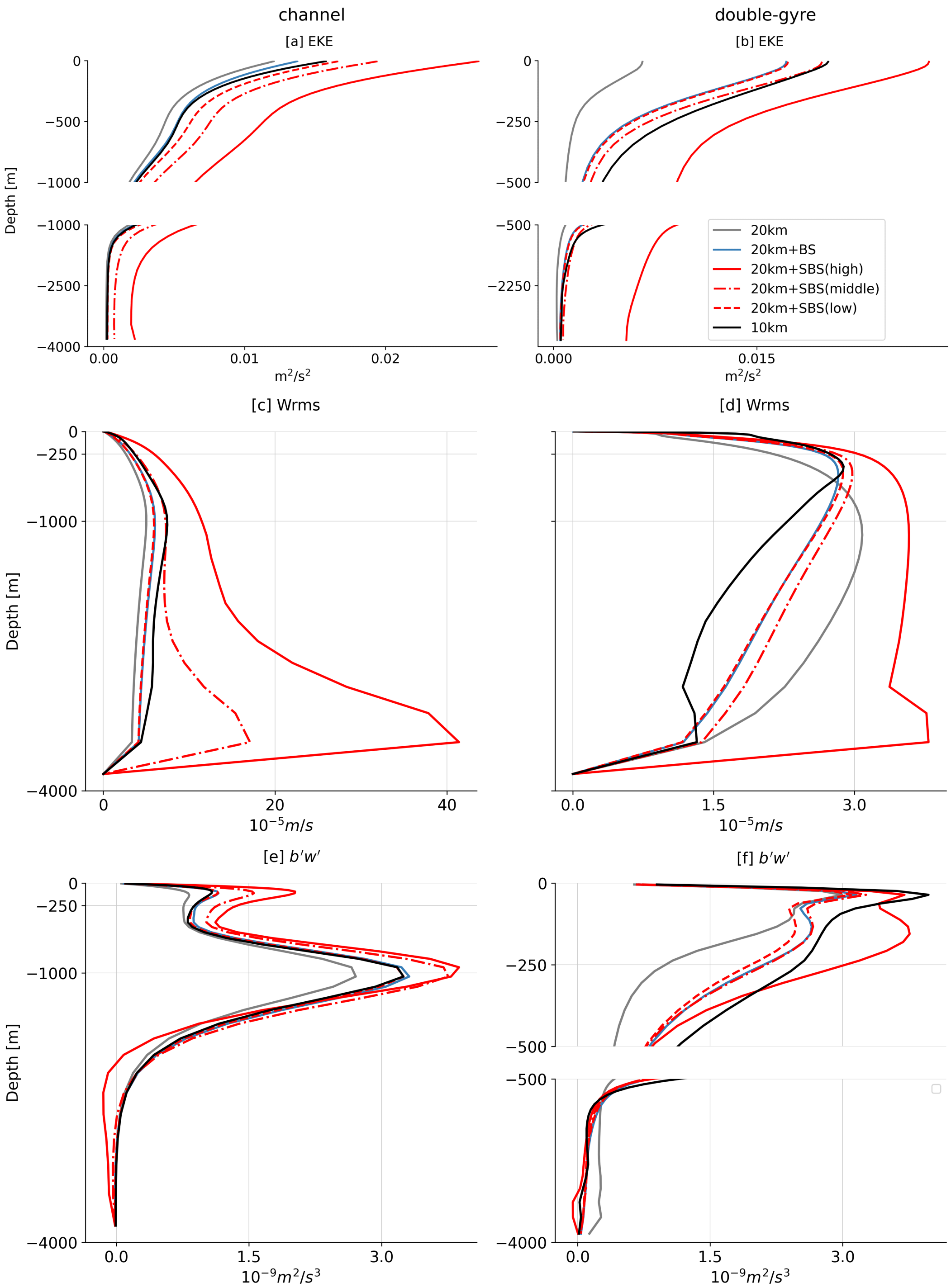

Figure 9. Vertical profiles for the channel setup (left column) and the double-gyre setup (right column) after incorporating stochastic terms of varying amplitudes. Each setup includes layer and time-averaged (9 years) diagnostics for EKE $[m^2/s^2]$ (a, b), the RMS vertical velocity anomalies $[m/s]$ (c,d), and buoyancy flux $[m^2/s^3]$ (e,f). Figures a, b, and f have a gap on the vertical axis.

profiles. For conciseness, we limit the discussion to the more realistic DG setup and also restrict to the low (C_1=0.001) and middle-intensity (C_1=0.005) cases for the stochastic term

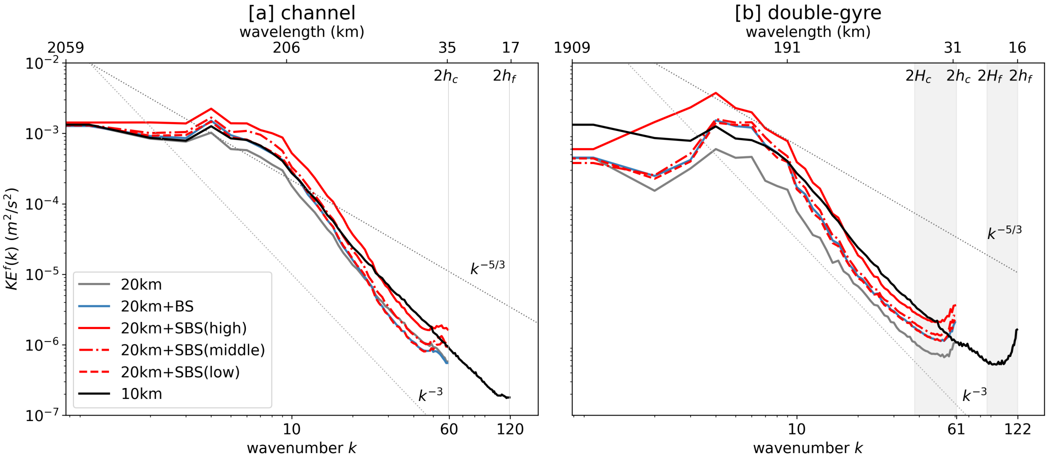

Figure 10. Kinetic energy spectra for different amplitudes of stochastic term. A dashed red line represents the spectra of the low-amplitude stochastic term on the subgrid and is almost identical to the spectra of the deterministic backscatter simulation data. The dashed-dotted and solid red lines represent data simulated with middle and high-amplitude stochastic terms, respectively.

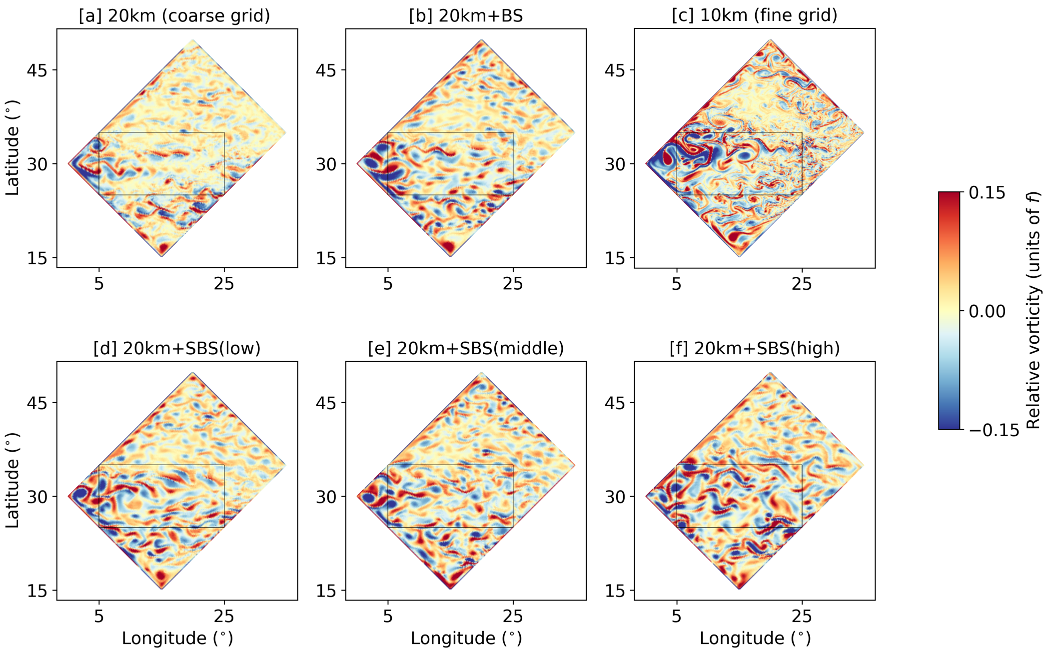

Figure 11. Snapshots of relative vorticity for coarse resolution without backscatter (a), coarse resolution with deterministic backscatter (b), fine resolution (c), and coarse resolution with varying stochastic backscatter amplitudes (d-f). The black boxes show the designated area for Fourier decomposition.

as the the large amplitude case has already been rejected as performing poorly (see Fig. 9 and the discussion in Section 3.8).

The SSH diagnostics show the time-averaged SSH for the coarse-grid simulation without backscatter (Fig. 12a), coarse-grid simulation with backscatter (Fig. 12b), and the

Table 2. Summary of global diagnostics, averaged over a 9-year period, comparing the various subgrid model options relative to the high-resolution reference, which is normalized to 100 %, except for RMSE $\overline{SSH}$, where high-resolution simulation corresponds to 0. The top-performing results for each diagnostic are set in red. It should be noted that the high-resolution reference is not the final truth when it comes to, e.g., KE, as at even higher resolution, it will be more KE. The vertically integrated buoyancy flux is taken over the top 500 m for the double-gyre setup.

Diagnostic variable	Setup	20 km	20 km+BS	20 km+BS+ADV	20 km+SBS (low) - 20 km+SBS (middle)	20 km+SBS (middle) +ADV	10 km
Surface KE m/s^2	CH DG	0.0170 (82%) 0.0144 (44%)	0.0209 (101%) 0.0252 (76%)	0.0232 (112%) 0.0262 (81%)	0.0216 - 0.0246 (104 -119%) 0.0256 - 0.0281 (79-86%)	0.0215 (104%) 0.0266 (82%)	0.0207 (100%) 0.0325 (100%)
Surface EKE m^2/s^2	CH DG	0.0121 (77%) 0.0066 (33%)	0.0137 (87%) 0.0171 (84%)	0.0182 (115%) 0.0183 (90%)	0.0167 - 0.0194 (106-123%) 0.0173 - 0.0198 (85-98%)	0.0164 (104%) 0.0199 (98%)	0.0158 (100%) 0.0203 (100%)
max $(b'\,w')$ $10^{-9}\,m^2/s^3$	CH DG	2.71 (83%) 2.99 (75%)	3.31 (122%) 3.15 (79%)	3.56 (133%) 3.24 (82%)	3.25 - 3.75 (100-138%) 3.10 - 3.26 (78-82%)	3.32 (123%) 3.23 (81%)	3.25 (100%) 3.97 (100%)
vert. int. $(b'\,w')$ $10^{-6}\,m^3/s^3$	CH DG	2.68 (84%) 0.68 (54%)	3.32 (104%) 1.01 (81%)	3.58 (113%) 1.03 (82%)	3.25 - 3.76 (102-118%) 0.96 - 1.02 (77-82%)	3.30 (104%) 1.01 (81%)	3.18 (100%) 1.25 (100%)
RMSE $\overline{SSH}$ (%)	DG	0.110	0.066	0.050	0.046 - 0.054	0.057	0

fine-resolution simulation (Fig. 12c). The middle and bottom rows of Fig. 12 show the time-averaged SSH difference between the coarse-grained high-resolution simulation and the different combinations of subgrid terms as indicated in the subplot headings.

Two features deserve particular attention: First, we look at the flow separation from the wall near the left corner of the domain. This point of separation is moved north when the resolution is finer. The reason for this is the reduction of viscous dissipation in higher-resolution simulations (more discussion in Sein et al. (2016)). For vertical walls, the sensitivity to the level of viscosity is higher than for sloped topography. Thus, the backscatter, which has a limited impact on the location of the mean flow and mainly affects the eddy part of the flow, can not completely fix the point of separation. However, we observe the magnitude of the mean SSH difference decreases with backscatter (dark red in the left corner in Fig. 12e–i vs. Fig. 12d). This moves the point of jet separation a little further north.

The presence of the subgrid advection term (Fig. 12e) decreases the difference to the high-resolution simulation along the jet area. At the same time, it slightly worsens the SSH difference in the south of the domain. The stochastic term helps to improve the southern area SSH difference (Fig. 12g–i), but with accompanying growth of noise in the difference field along the north-west boundary (Fig. 12i). Overall, combining the classical backscatter with the additional components reduce the RMSE $\overline{SSH}$ by about 50%.

Second, the density profiles are compared on a North-South transect at 15° longitude (Fig. 13). We observe a significant difference between coarse-resolution without backscatter and any of the simulations with backscatter: without backscatter, one can see a nearly barotropic jet penetrating along the entire water column at around 30° N. The lack of eddies together with the wind forcing lead to steep isopycnals and strong vertical mixing in the middle of the domain. With backscatter, eddies can form, which immediately reduces the barotropic mixing, and also improves the form of isopycnals in the upper layers toward the slopes seen in the reference simulation. In addition, the backscatter DG simulations after 9 years might still contain some drift in the stratification, although probably small (i.e. the figures might still change a bit if we let it run for longer).

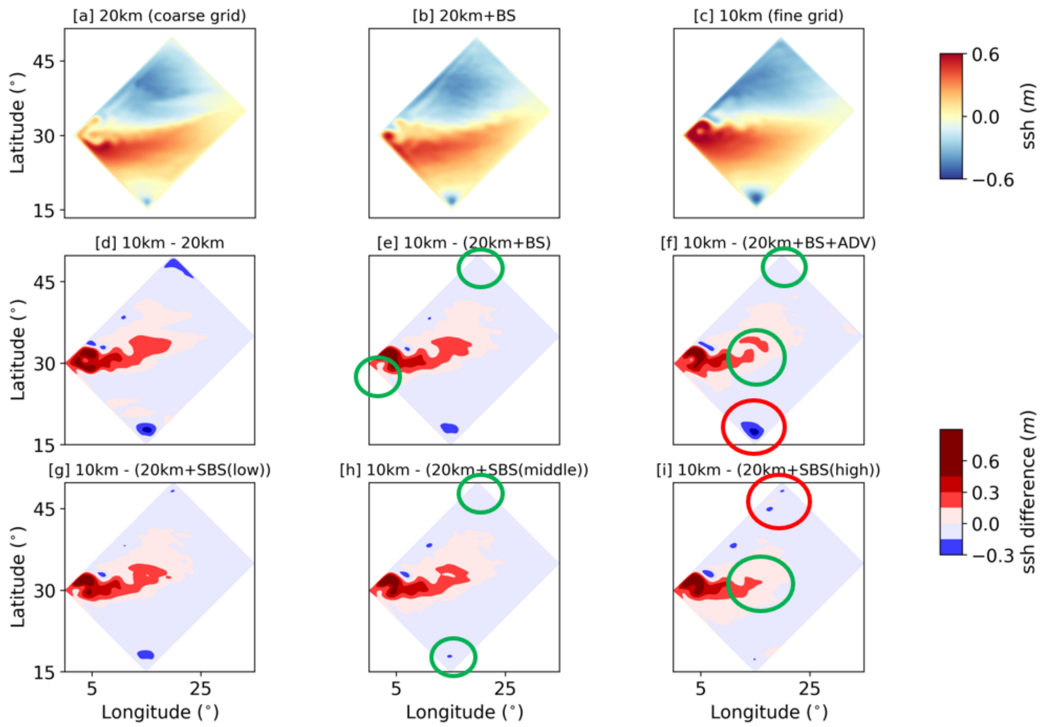

Figure 12. Over nine years, the sea surface height [m] was averaged and compared between three simulations: coarse-resolution simulation (a), coarse-resolution simulation with deterministic backscatter (b), and fine resolution (c). The difference in SSH between the high-resolution coarse-grained simulation and the various coarse-resolution simulations (d-i) was also analyzed. Green and red circles indicate specific regions of improvements and impairments compared to the low resolution.

Adding advection (Fig. 13d vs. Fig. 13c, Fig. 13h vs. Fig. 13e and Fig. 13i vs. Fig. 13f) straightens the slope of isopycnals, especially in the deep southern part of the domain where the isopycnal levels bend too much in the backscatter-only case (Fig. 13c). Moreover, the contours of the isopycnal surfaces become more variable, again more like in the reference simulation. Adding the stochastic term straightens isopycnals along the entire domain. The optimal results are obtained using the stochastic term of moderate amplitude within the range of noise amplitudes. The low-amplitude noise does not have a big impact, while the high-amplitude noise leads to excessive mixing near the surface.

Based on SSH diagnostics (Fig. 13i) as well as EKE diagnostics (Table 2), the coarse-resolution setup that utilizes a combination of the middle-intensity stochastic term and advection component on the subgrid produces very good results. Furthermore, the new terms individually have the potential to improve certain flow features (Table 2) and rectify the flow behavior in different regions of the DG field (Fig. 13f,h).

Compared to the reference high-resolution simulation, coarse-resolution simulations with backscatter still have too much mixing. We increase EKE in the coarse resolution, but our diffusivity (in tracer equations) is not touched. Larger EKE corresponds to stronger temperature gradients and hence stronger mixing due to diffusion. So one would expect a bit more diapycnal mixing in this case.

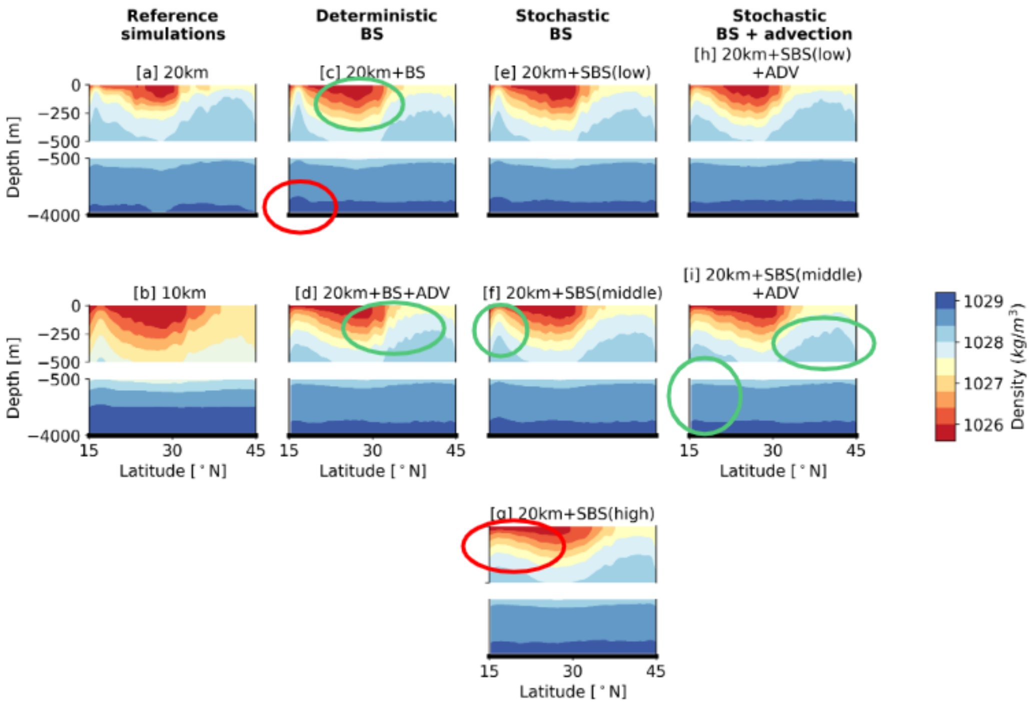

Figure 13. The annual average of the vertical density profiles along 15° longitude for the double-gyre setup. The green circles indicate where specific improvements were made toward the high-resolution reference simulation, while the red circles indicate areas with impairments. The figures have a gap on the vertical axis.

4 Discussion and conclusion

In this work, we tested the performance of two additional contributions to the subgrid energy equation, advection, and stochastic forcing, in the framework of kinetic energy backscatter of Juricke et al. (2019), which is based on earlier work by Jansen et al. (2015).

The idea behind advecting subgrid kinetic energy by the three-dimensional resolved flow is motivated by the fact that the locations of kinetic energy dissipation and forcing do not necessarily coincide. Our results show that, indeed, this additional contribution to the subgrid energy equation has an unconditionally positive effect: it corrects the behavior of isopycnals, decreases the difference of SSH to the high-resolution simulation in eddy-rich regions and improves the mean vertical profiles. Energetically, subgrid advection catalyzes all scales, enhancing energy creation and dissipation. In some situations, these effects are small but with tendency toward the reference truth. At the same time, the advection of subgrid energy adds only a 1.5% penalty to simulation time. Moreover, no tuning is necessary as it is based on physical modeling. Our conclusion is, therefore, that subgrid kinetic energy should be treated with advection.

The second additional, stochastic contribution to the subgrid energy budget has been designed to enhance the simulated eddy variability by incorporating data on regions of enhanced eddy activity from a high-resolution simulation. Such a stochastic term can improve diagnostics in the flow's calm and active areas. In particular, the improvement in SSH variability could not be achieved with deterministic backscatter only. Moreover, the spectral characteristics of the flow with stochastic subgrid forcing improve across a wide range of scales. However, we need to be cautious when using stochastic forcing: if its amplitude is too large, it can cause serious distortions and artifacts, even while a consequently improved energy spectrum may be close to expectations. Moreover, the acceptable level depends on the setup and is difficult to assess a priori. It is possible, to some extent, to guard against such failures by looking for anomalies in the amplitude of vertical velocity fluctuations in deep water or an excess of eddies in calm regions of the domain. But careful monitoring and tuning is critical and it will generally be necessary to recompute patterns for different domains.

None of the parameterizations considered here are guaranteed to force only Rossby modes. Thus, it is of concern whether backscatter leads to excessive diapycnal mixing. However, our analysis of the density diagnostics did not find any evidence of such behavior. Why and under which circumstances this is the case remains an open question and may be related to more complex bathymetry.

Stochastic forcing not only improves the flow characteristics, when done carefully, but also allows generating ensemble simulations. This enables the construction of distribution functions for output variables and measures the uncertainty of backscatter performance, an important potential direction for further research.

Several other aspects, which are worth further investigation, relate to the design of the stochastic term. One potential alternative to the EOF method is the use of dynamical mode decomposition as a tool to understand the flow variability and reduce the dimensionality of the system (Franzke et al., 2022). Following the EOF approach, the selection of data for decomposition and the number of the EOF modes, which explains a sufficient amount of missing variability, remain at the modeler's discretion.

Machine learning methods could capture the missing variability as an alternative to stochastic methods. Deep learning methods driven by the data from an idealized simulation (Bolton & Zanna, 2019) and from the realistic coupled climate models (Guillaumin & Zanna, 2021) were applied to ocean momentum forcing to represent the subgrid variability. The authors showed that convolutional neural networks can be constructed to satisfy the momentum conservation law and capture spatial and temporal eddy variability.

Finally, the necessary scale separation between the work of the backscatter and viscous operators is crucial and can be diagnosed by spectral methods. When there is not enough scale separation, the energy injection occurs in the dissipation scale range. This results in highly disturbed flow filaments and prevents eddies from propagating in a physically coherent manner. We cannot exclude potential interference between the role of advection and the degree of backscatter operator smoothing, as both affect the spatial locality of backscatter. However, insufficient scale separation between dissipation and backscatter causes serious flow distortion and is inadequate as an eddy parameterization for FESOM2.

Potential research on parametrizing mesoscale eddies beyond the scope of dynamic energy backscatter could be related to the position of large oceanic structures (for instance, the jet in the case of the double-gyre setup) in coarse resolution simulations. Dynamic backscatter, in any of its variations considered here, so far did not yield fundamental improvements, for example, of the point of jet separation. This is mostly likely due to the variety of processes interacting in such highly dynamic regions, which cannot all be improved by backscatter alone. However, improvements to the mean flow by the default dynamic backscatter have also been observed by (Juricke et al., 2020b). Nevertheless, new or extended approaches in this regard remain a focus of further research.

5 Open Research

Data Availability Statement

The model output data is publicly available at `https://zenodo.org/record/8248679`. The latest stable FESOM2 release (with the new backscatter terms implementation soon to be added) is available at `https://github.com/FESOM/fesom2`. Routines for the Fourier spectra are available at `https://zenodo.org/record/7270305` (Bellinghausen, 2022).

Acknowledgments

This paper is a contribution to the project M3 (Towards Consistent Subgrid Momentum Closures) of the Collaborative Research Centre TRR 181 "Energy Transfers in Atmosphere and Ocean" funded by the Deutsche Forschungsgemeinschaft (DFG, German Research Foundation) – Project-ID 274762653 – TRR 181. The computational resources were supplied by the supercomputing facilities at the Alfred-Wegener-Institut, Helmholtz-Zentrum für Polar- und Meeresforschung.

Appendix A Appendix

Table A1. Table of setups coefficients

Coefficients	Channel	Double-gyre
β-coefficient	$1.6 \cdot 10^{-11}$	$1.8 \cdot 10^{-11}$
Bottom drag (C_d)	0.005	0.001
Background viscosity amplitude (γ_0[m/s]) (Formula 12 in Juricke et al. (2020))	0.001	0.005
Coefficient of flow-aware viscosity (γ_1) (Formula 12 in Juricke et al. (2020))	0.06	0.3
Years of spin-up	1	50
Years of analysis/averaging	9	9

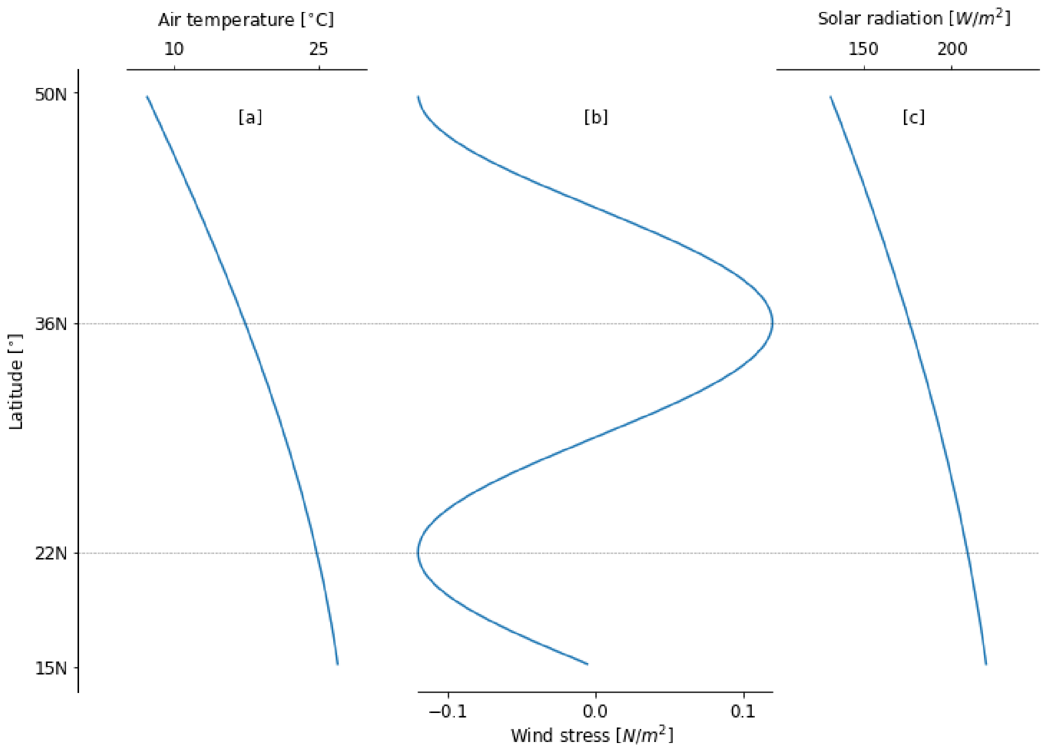

Figure A1. The analytical forcing functions are based on latitude in the double-gyre setup. These functions include air surface layer temperature (a), wind stress (b), and solar radiation (c).

References

Bellinghausen, K. (2022). *Spectral diagnostics for triangular meshes (version 1.0) [software].* Zenodo. DOI: 10.5281/zenodo.7270305

Berner, J., Shutts, G., Leutbecher, M., & Palmer, T. (2009). A spectral stochastic kinetic energy backscatter scheme and its impact on flow-dependent predictability in the ECMWF ensemble prediction system. *J. Atmos. Sci.*, *66*, 603–626. DOI: 10.1175/2008JAS2677.1

Bolton, T., & Zanna, L. (2019). Applications of deep learning to ocean data inference and subgrid parameterization. *J. Adv. Model. Earth Syst.*, *11*(1), 376–399. DOI: 10.1029/2018MS001472

Cooper, F. C. (2017). Optimisation of an idealised primitive equation ocean model using stochastic parameterization. *Ocean Model.*, *113*, 187–200. DOI: 10.1016/j.ocemod.2016.12.010

Danilov, S., Sidorenko, D., Wang, Q., & Jung, T. (2017). The Finite-volumE Sea ice–Ocean Model (FESOM2). *Geosci. Model Dev.*, *10*(2), 765–789. DOI: 10.5194/gmd-10-765-2017

Dwivedi, S., Franzke, C. L. E., & Lunkeit, F. (2019). Energetically consistent stochastic and deterministic kinetic energy backscatter schemes for atmospheric models. *Q. J. Roy. Meteorol. Soc.*, *145*, 1–11. DOI: 10.1002/qj.3625

Ferrari, R., & Wunsch, C. (2009). Ocean circulation kinetic energy: Reservoirs, sources, and sinks. *Annu. Rev. Fluid Mech.*, *41*(1), 253–282. DOI: 10.1146/annurev.fluid.40.111406.102139

Fox-Kemper, B., Adcroft, A., Böning, C. W., Chassignet, E. P., Curchitser, E., Danabasoglu, G., . . . Yeager, S. G. (2019). Challenges and prospects in ocean circulation models.

Frontiers in Marine Science, *6*. DOI: 10.3389/fmars.2019.00065

Fox-Kemper, B., Ferrari, R., & Hallberg, R. (2008). Parameterization of mixed layer eddies. Part I: theory and diagnosis. *J. Phys. Oceanogr.*, *38*, 1145–1165. DOI: 10.1175/2007JPO3792.1

Franzke, C. L. E., Gugole, F., & Juricke, S. (2022, 07). Systematic multi-scale decomposition of ocean variability using machine learning. *Chaos: An Interdisciplinary Journal of Nonlinear Science*, *32*(7), 073122. DOI: 10.1063/5.0090064

Frederiksen, J., O'Kane, T., & Zidikheri, M. (2013, 01). Subgrid modelling for geophysical flows. *Phil. Trans. R. Soc. A*, *371*, 20120166. DOI: 10.1098/rsta.2012.0166

Gent, P. R. (2011). The Gent–McWilliams parameterization: 20/20 hindsight. *Ocean Model.*, *39*(1–2), 2–9. DOI: 10.1016/j.ocemod.2010.08.002

Gent, P. R., & McWilliams, J. C. (1990). Isopycnal mixing in ocean circulation models. *J. Phys. Oceanogr.*, *20*, 150–155. DOI: 10.1175/1520-0485(1990)020⟨0150:IMIOCM⟩2.0.CO;2

Grooms, I., & Majda, A. J. (2013). Efficient stochastic superparameterization for geophysical turbulence. *Proc. Nat. Acad. Sci.*, *110*, 4464–4469. DOI: 10.1073/pnas.1302548110

Grooms, I., Majda, A. J., & Smith, K. S. (2015). Stochastic superparameterization in a quasigeostrophic model of the Antarctic Circumpolar Current. *Ocean Model.*, *85*, 1–15. DOI: 10.1016/j.ocemod.2014.10.001

Guillaumin, A. P., & Zanna, L. (2021). Stochastic-deep learning parameterization of ocean momentum forcing. *J. Adv. Model. Earth Syst.*, *13*(9), e2021MS002534. DOI: 10.1029/2021MS002534

Hallberg, R. (2013). Using a resolution function to regulate parameterizations of oceanic mesoscale eddy effects. *Ocean Model.*, *72*, 92–103. DOI: 10.1016/j.ocemod.2013.08.007

Hewitt, H., Roberts, M., Mathiot, P., Biastoch, A., Blockley, E., Chassignet, E., ... Zhang, Q. (2020, 12). Resolving and parameterising the ocean mesoscale in earth system models. *Current Climate Change Reports*, 137–152. DOI: 10.1007/s40641-020-00164-w

Jansen, M. F., Adcroft, A., Khani, S., & Kong, H. (2019). Toward an energetically consistent, resolution aware parameterization of ocean mesoscale eddies. *J. Adv. Model. Earth Syst.*, *11*(8), 2844–2860. DOI: 10.1029/2019MS001750

Jansen, M. F., & Held, I. M. (2014). Parameterizing subgrid-scale eddy effects using energetically consistent backscatter. *Ocean Model.*, *80*, 36–48. DOI: 10.1016/j.ocemod.2014.06.002

Jansen, M. F., Held, I. M., Adcroft, A. J., & Hallberg, R. (2015). Energy budget-based backscatter in an eddy permitting primitive equation model. *Ocean Model.*, *94*, 15–26. DOI: 10.1016/j.ocemod.2015.07.015

Juricke, S., Bellinghausen, K., Danilov, S. D., Kutsenko, A. A., & Oliver, M. (2023). Scale analysis on unstructured grids: Kinetic energy and dissipation power spectra on triangular meshes. *J. Adv. Model. Earth Syst.*, *15*, e2022MS003280. DOI: 10.1029/2022MS003280

Juricke, S., Danilov, S., Koldunov, N., Oliver, M., Sein, D. V., Sidorenko, D., & Wang, Q. (2020). A kinematic kinetic energy backscatter parametrization: From implementation to global ocean simulations. *J. Adv. Model. Earth Syst.*, *12*, e2020MS002175. DOI: 10.1029/2020MS002175

Juricke, S., Danilov, S., Koldunov, N., Oliver, M., & Sidorenko, D. (2020b). Ocean kinetic energy backscatter parametrization on unstructured grids: Impact on global eddy-permitting simulations. *J. Adv. Model. Earth Syst.*, *12*, e2019MS001855. DOI: 10.1029/2019MS001855

Juricke, S., Danilov, S., Kutsenko, A., & Oliver, M. (2019). Ocean kinetic energy backscatter parametrizations on unstructured grids: Impact on mesoscale turbulence in a channel. *Ocean Model.*, *138*, 51–67. DOI: 10.1016/j.ocemod.2019.03.009

Juricke, S., Palmer, T. N., & Zanna, L. (2017). Stochastic sub-grid scale ocean mixing: Impacts on low frequency variability. *J. Climate*, *30*(30), 4997–5019. DOI: 10.1175/

JCLI-D-16-0539.1

Klöwer, M., Jansen, M. F., Claus, M., Greatbatch, R. J., & Thomsen, S. (2018). Energy budget-based backscatter in a shallow water model of a double gyre basin. *Ocean Model.*, *132*, 1–11. DOI: 10.1016/j.ocemod.2018.09.006

Leutbecher, M., Lock, S.-J., Ollinaho, P., Lang, S. T. K., Balsamo, G., Bechtold, P., ... Weisheimer, A. (2017). Stochastic representations of model uncertainties at ECMWF: state of the art and future vision. *Quart. J. Roy. Meteorol. Soc.*, *143*(707), 2315–2339. DOI: 10.1002/qj.3094

Levy, M., Klein, P., Treguier, A.-M., Iovino, D., Madec, G., Masson, S., & Takahashi, K. (2010, 12). Modifications of gyre circulation by sub-mesoscale physics. *Ocean Model.*, *34*, 1–15. DOI: 10.1016/j.ocemod.2010.04.001

Mana, P. P., & Zanna, L. (2014). Toward a stochastic parameterization of ocean mesoscale eddies. *Ocean Model.*, *79*, 1–20. DOI: 10.1016/j.ocemod.2014.04.002

Pacanowski, R. C., & Philander, S. G. H. (1981). Parameterization of vertical mixing in numerical models of tropical oceans. *J. Phys. Oceanogr.*, *11*(11), 1443–1451. DOI: 10.1175/1520-0485(1981)011⟨1443:POVMIN⟩2.0.CO;2

Perezhogin, P. (2019). Deterministic and stochastic parameterizations of kinetic energy backscatter in the NEMO ocean model in Double-Gyre configuration. *IOP Conf. Ser.: Earth Environ. Sci.*, *386*, 012025. DOI: 10.1088/1755-1315/386/1/012025

Redi, M. H. (1982). Oceanic isopycnal mixing by coordinate rotation. *J. Phys. Oceanogr.*, *12*(10), 1154–1158. DOI: 10.1175/1520-0485(1982)012⟨1154:OIMBCR⟩2.0.CO;2

Scholz, P., Sidorenko, D., Danilov, S., Wang, Q., Koldunov, N., Sein, D., & Jung, T. (2022). Assessment of the finite-volume sea ice–ocean model (fesom2.0) – part 2: Partial bottom cells, embedded sea ice and vertical mixing library cvmix. *Geoscientific Model Development*, *15*(2), 335–363. DOI: 10.5194/gmd-15-335-2022

Scholz, P., Sidorenko, D., Gurses, O., Danilov, S., Koldunov, N., Wang, Q., ... Jung, T. (2019). Assessment of the Finite VolumE Sea Ice Ocean Model (FESOM2.0), Part I: Description of selected key model elements and comparison to its predecessor version. *Geosci. Model Dev. Discussions*, *2019*, 1–42. DOI: 10.5194/gmd-2018-329

Sein, D. V., Danilov, S., Biastoch, A., Durgadoo, J. V., Sidorenko, D., Harig, S., & Wang, Q. (2016). Designing variable ocean model resolution based on the observed ocean variability. *J. Adv. Model. Earth Syst.*, *8*(2), 904–916. DOI: 10.1002/2016MS000650

Soufflet, Y., Marchesiello, P., Lemarié, F., Jouanno, J., Capet, X., Debreu, L., & Benshila, R. (2016). On effective resolution in ocean models. *Ocean Model.*, *98*, 36–50. DOI: 10.1016/j.ocemod.2015.12.004

Zanna, L., Mana, P. P., Anstey, J., David, T., & Bolton, T. (2017). Scale-aware deterministic and stochastic parametrizations of eddy-mean flow interaction. *Ocean Model.*, *111*, 66–80. DOI: 10.1016/j.ocemod.2017.01.004

Advancing eddy parameterizations: Dynamic energy backscatter and the role of subgrid advection and stochastic forcing

Ekaterina Bagaeva[1,2], Sergey Danilov[2], Marcel Oliver[3], Stephan Juricke[1,2]

[1]Constructor University, Campus Ring 1, 28759 Bremen, Germany
[2]Alfred Wegener Institute for Polar and Marine Research, Am Handelshafen 12, 27570 Bremerhaven, Germany
[3]Mathematical Institute for Machine Learning and Data Science, KU Eichstätt–Ingolstadt, Auf der Schanz 49, 85049 Ingolstadt, Germany

Key Points:

- Implementation and positive evaluation of subgrid advection for kinetic energy backscatter parameterization
- Inclusion of new stochastic term - based on high-resolution data - to subgrid energy equation
- Scale analysis reveals the necessity of sufficient scale separation between viscous energy dissipation and energy injection via backscatter

Corresponding author: Ekaterina Bagaeva, ebagaeva@constructor.university

Abstract

A universal approach to overcome resolution limitations in the ocean is to parametrize physical processes. The traditional method of parametrizing mesoscale range processes on eddy-permitting mesh resolutions, known as a viscous momentum closure, tends to over-dissipate eddy kinetic energy. To return excessively dissipated energy to the system, the viscous closure is equipped with a dynamic energy backscatter, which amplitude is based on the amount of unresolved kinetic energy (UKE). Our study suggests including the advection of UKE to consider the effects of nonlocality on the subgrid. Furthermore, we suggest incorporating a stochastic element into the subgrid energy equation to account for variability, which is not present in a fully deterministic approach. This study demonstrates increased eddy activity and highlights improved flow characteristics. In addition, we provide diagnostics of optimal scale separation between dissipation and injection operators. The implementations are tested on two intermediate complexity setups of the global ocean model FESOM2: an idealized channel setup and a double-gyre setup.

Plain Language Summary

Modeling oceanic eddies requires incorporating physical processes through additional equations. While the overall understanding of the ocean is clear, the models tend to lose too much kinetic energy, resulting in systematic errors. Our goal in this study is to explore how to prevent false energy loss by sending the energy back to where it originated. Our research shows that by adding an advection and a random element, the current method can better capture the turbulent nature of the flow. We tested the implementation on the channel and the double-gyre setups and observed an increase in eddy activity and an improvement in flow characteristics.

1 Introduction

Mesoscale eddies play an important role in determining ocean circulation. They contain a large part of the kinetic energy (KE) of the ocean, contribute to the transfer of heat and properties, and impact the form and evolution of ocean currents. Their horizontal size is proportional to the Rossby radius of deformation, which reaches up to 200 km in the low latitudes, decreasing to less than 10 km in high latitudes. In addition, the Rossby radius decreases in shelf areas reflecting weak density stratification and small depth.

Mesoscale eddies are generated through different types of instabilities, with the most prominent sources being the baroclinic instability and the instabilities of the mean flow. Baroclinic instability releases the available potential energy (APE) maintained by the mean forcing of the ocean, transferring it into eddy kinetic energy (EKE) across a range of scales near the Rossby deformation radius (Ferrari & Wunsch, 2009).

A direct cascade of enstrophy to small scales and an inverse cascade of energy to large scales usually accompany the dynamics of mesoscale eddies. Eddy kinetic energy is partly transferred to mean kinetic energy, but the rest of the upscale transfer is stopped by large-scale friction, eddy killing by winds at the surface, interactions with topography, or wave generation. Enstrophy and some energy go downscale, reaching grid scales where they need to be dissipated through horizontal eddy viscosity. In nature, at even smaller scales of the cascade, the flow transitions to ageostrophic turbulence and waves and finally to three-dimensional turbulence, the energy of which is converted to heat by molecular dissipation.

In climate studies, ocean models are integrated over hundreds of years, which limits their resolution to coarse (around 1°) or eddy-permitting resolutions (around $1/4^\circ$)(Hewitt et al., 2020). Baroclinic instability in an ocean model is not resolved at coarse resolution, and eddy-driven transfers of buoyancy and other properties are absent. The APE cannot be converted to EKE; it has to be taken out by parameterizations compensating for the missing eddies. This is generally done by the Gent-McWilliams (GM) parameterization (Gent & McWilliams, 1990; Gent, 2011), which introduces the so-called eddy bolus velocities, which model the eddy-driven property fluxes and release the APE. Additionally, the missing mixing by eddies along isopycnal surfaces is parameterized by isopycnal diffusion (Redi, 1982)

The horizontal grids with a cell size around $1/4°$ or $1/6°$ are often described as "eddy-permitting." Such grids are sufficiently fine to represent eddies and simulate baroclinic instability in parts of the ocean. The GM parameterization must be carefully tuned on eddy-permitting meshes, as described in Hallberg (2013). However, the range of resolved scales on such meshes is not large enough, and viscous closures (e.g., Fox-Kemper et al., 2008) intended to eliminate enstrophy and energy at grid scales also affect the scales where eddies are generated by baroclinic instability and where the bulk of EKE is residing. As a result, both EKE and eddy generation are excessively dissipated. Until the resolution reaches the level of resolving sub-mesoscale dynamics (generally finer than 5 km at midlatitudes), the entire range of scales, including large scales, will be exposed to the over-dissipation, as illustrated, e.g., by Soufflet et al. (2016). It leads to an underestimated transfer of heat, salt, momentum and misrepresentation of the mean dynamics of the ocean and the forcing sensitivity of models.

For a more accurate ocean simulation and better representation of eddy dynamics, energy dissipated due to horizontal viscosity should be returned back to the system. The kinetic energy backscatter parameterization proposed for the ocean in Jansen et al. (2015) and developed further by Juricke et al. (2019) is intended to help in such situations. Within our work, energy backscatter performs the function of energy reinjection, transferring energy to the scales of eddy generation, thereby compensating the over-dissipation of the large scales and energizing the entire range of scales.

The concept of energy backscatter in its deterministic and stochastic forms has a long history of research in atmospheric and ocean sciences. Physical and numerical approaches to the compensation of excessive energy losses for atmospheric parameterization were mentioned in the works of e.g. Berner et al. (2009), Leutbecher et al. (2017), Dwivedi et al. (2019). Idealized ocean models were enhanced by backscatter to account for the dynamics of unresolved mesoscale eddies in the works of e.g. Frederiksen et al. (2013), Jansen and Held (2014), Jansen et al. (2015), Zanna et al. (2017).

The task of backscatter implementation has simple solutions, such as a kinematic backscatter, proposed in Juricke et al. (2020). It reduces viscous over dissipation by subtracting locally averaged viscous force multiplied by a tuning coefficient. This parameterization does not increase the computational costs and significantly improves ocean simulation toward the high-resolution truth. However, it acts instantaneously and can not be flow-aware simply due to the backscatter design.

More physically grounded and reliable is the concept of dynamic energy backscatter, whose amplitude depends on the subgrid energy, first introduced in the context of eddy-permitting ocean models by Jansen et al. (2015) and developed further by Juricke et al. (2019). The subgrid kinetic energy budget, which will be explained further, controls how the excessively dissipated energy is returned back to the resolved scales. This work aims to contribute to the theory and practical use of the kinetic energy backscatter in the following three directions.

First, the existing implementations of dynamic kinetic energy backscatter by Jansen et al. (2015), Juricke et al. (2019), Juricke et al. (2020b), Klöwer et al. (2018) are either considering the balance of unresolved (subgrid) EKE (i.e., UKE) as taking place locally or being distributed by the barotropic (vertically mean) flow (Jansen et al., 2019). This is arguably a simplification, as UKE should be transported by the fully resolved 3D flow, and a question arises whether ignoring this transport is a good approximation. Indeed, one may expect that input (generation) of subgrid energy and its dissipation are not colocated, and the UKE density at a given point is influenced by its input in regions upstream. Only in situations when the flow statistics are homogeneous in the direction of mean flow (e.g., a uniform zonally re-entrant channel flow), the advection can be assumed to be of minor importance, but even in such cases, eddies can be strong enough to introduce inhomogeneities affecting the distribution of UKE in space.

This paper tries to partly answer the question of the role of subgrid advection. For this, we implement full 3D advection of UKE in backscatter parameterization of Juricke et al. (2019) and demonstrate that accounting for advection leads to consistent improvements compared to control simulations in which the advection of UKE was ignored. This conclusion holds even for the channel setup with zonally homogeneous mean flow.

Second, while stochastic backscatter can offer more freedom in how to return energy to the resolved scales than deterministic backscatter and also can be used to represent missing variability and subgrid uncertainties, the question of the optimal form of the stochastic contribution in backscatter schemes remains open. Among existing studies, stochastic eddy forcing is applied to the quasi-geostrophic model in Mana and Zanna (2014); stochastic parameterizations extracting information from the subgrid eddy statistics are studied in Grooms and Majda (2013), Grooms et al. (2015); stochastic forcing is applied to velocity and temperature equations in Cooper (2017); stochastic perturbations are tested on various parameterization schemes in Juricke et al. (2017). Perezhogin (2019) develops and compares deterministic and stochastic kinetic energy backscatter schemes for the primitive equations of the ocean. The interest of the ocean modeling community in stochastic schemes remains high and is expected to increase further during this decade (Fox-Kemper et al., 2019).

We propose to combine the deterministic backscatter with a stochastic approach by adding a new stochastic term to the UKE. The new term is designed to improve the simulated eddy variability using data from a high-resolution reference simulation denoted as truth. We test different intensities of such a data-driven stochastic term and find that certain intensity ranges benefit the flow. However, exceeding these intensity intervals can lead to serious flow distortion.

Third, in both deterministic and stochastic energy backscatter parameterizations, one has to decide about the scale of energy injection. Spatial smoothing applied to the injection ensures a scale separation between energy reinjection and energy dissipation. Spatial filtering operators commonly involve only the nearest discrete cells for the reason of parallel implementation. Every cycle of spatial filtering applied to the operators increases the scales on which these operators act. Both over-smoothing and insufficient smoothing hamper performance of the backscatter term.

Understanding scale separation is also essential when several parameterizations are applied simultaneously. Jansen et al. (2019) consider a generalized energy-based parameterization that combines the GM parameterization and backscatter approach proposed in Jansen et al. (2015). The GM parameterization dissipates APE at the grid scales and represents the effect of the conversion of APE into EKE; however, classically ignoring the respective EKE input into the momentum equations. A significant result of their paper is the opportunity to smoothly tune the model between non-eddy-resolving and eddy-resolving regimes by coupling GM to the backscatter parameterization.

The question on optimal smoothing is the third question addressed in this work. We show that insufficient scale separation could cause a leak of energy and the inability of the flow structures to propagate coherently.

The set of numerical simulations addresses the three research questions raised above. We run the Finite-volumE Sea ice-Ocean Model (FESOM2, Danilov et al., 2017; Scholz et al., 2019) for two middle complexity setups: a channel setup and a double gyre setup, described in detail in Section 2.4. Channel simulations allow us to compare results with the previous works mostly tested on the channel setup (e.g., Juricke et al., 2020). However, it has several disadvantages, such as high variability of area-integrated kinetic energy due to the channel's narrowness or a lack of spatial separation between regions of release and dissipation of energy. As an extension of the idealized channel setup, the double-gyre setup has more defined areas of creation and dissipation of kinetic energy and a longer zonal direction that allows eddies to develop and evolve in space. It also has the advantage of being more intuitively understandable and closer to reality, as it represents the idealized physical processes of subpolar and subtropical gyres in the North Atlantic or North Pacific basins. In addition, the double-gyre setup can be extended to include more complicated coastlines and bottom topography to create an even more realistic representation of basin dynamics.

The outline of the article is as follows. We begin in Section 2 with the model essentials, which include the methodology used to create the new components of the subgrid energy budget for energy backscatter, the description of the two modeling setups that we use to test the implementations and the diagnostics used to investigate the effect of the new components. Section 3 describes the results and improvements achieved in simulations whereas the advection and stochastic components in the UKE, applied independently and simultaneously. The paper closes with discussions and conclusions in Section 4.

2 Model essentials

2.1 Equations of motion

We solve the primitive equations in idealized ocean basins with eddy viscosity and backscatter. The horizontal momentum equation reads

$$\partial_t \boldsymbol{u}_\mathrm{h} + f\,\boldsymbol{e}_z \times \boldsymbol{u}_\mathrm{h} + (\boldsymbol{u}_\mathrm{h}\cdot\boldsymbol{\nabla}_\mathrm{h} + w\partial_z)\boldsymbol{u}_\mathrm{h} + \boldsymbol{\nabla}_\mathrm{h} p/\rho_0 = \boldsymbol{V}(\boldsymbol{u}_\mathrm{h}) + \boldsymbol{B}(\boldsymbol{u},e) + \partial_z(\nu_v\,\partial_z \boldsymbol{u}_\mathrm{h}) \quad (1)$$

where $\boldsymbol{u} = (u, v, w)$ denotes the full three-dimensional velocity field, $\boldsymbol{u}_\mathrm{h} = (u, v)$ the horizontal velocity field, f the Coriolis parameter, $\boldsymbol{e}_z$ the unit vertical vector, p the pressure, ρ_0 the reference density, $\boldsymbol{V}(\boldsymbol{u}_\mathrm{h})$ the horizontal eddy viscosity, $\boldsymbol{B}(\boldsymbol{u}, e)$ the backscatter operator, described in more detail below, and ν_v the coefficient of vertical viscosity.

The vertical momentum equation reduces to hydrostatic balance in the form

$$\partial_z p = -g\rho = b\rho_0\,, \quad (2)$$

where g is the gravitational acceleration and ρ is the deviation of density from its reference value ρ_0; b denotes buoyancy and will be used in the following.

The equation for an arbitrary tracer takes the form

$$\partial_t T + \boldsymbol{\nabla}\cdot(\boldsymbol{u}T) = \boldsymbol{\nabla}(\boldsymbol{K}\boldsymbol{\nabla}T)\,, \quad (3)$$

where T is a tracer (temperature or salinity) and $\boldsymbol{K}$ is the diffusivity tensor in the form of a symmetric 3×3 matrix that aims at minimal mixing of tracers across surfaces of isoneutral density. We assume the linear form of the equation of state, in particular, density is linearly dependent only on temperature (salinity tracer stays constant in time). In this case, isoneutral $\boldsymbol{K}$ implies no mixing.

The horizontal viscosity operator in Eq. (1) is biharmonic and has the form described in Juricke et al. (2020), which was found to be minimally dissipative for FESOM.

Backscatter tries to reduce over-dissipation by harnessing the inverse cascade. The coefficients of viscous and backscatter parameterizations have opposite signs, and different approaches define their amplitude. Backscatter is based on a subgrid energy budget simulating the kinetic energy available for backscattering into the resolved flow.

Here, as in Jansen et al. (2015) and (Juricke et al., 2019), we use an explicit subgrid energy budget at each grid cell that defines the backscatter coefficient, i.e., the amplitude of local backscatter. The advantage of this approach is that we can explicitly control and model the transfer of energy between different terms of the resolved dynamics and the subgrid. The kinetic energy accumulated on the subgrid, $e = e(x, y, z, t)$, is called *unresolved kinetic energy* (UKE). The particular model for UKE studied by Juricke et al. (2019) is of the general form

$$\partial_t e = -c_{\text{dis}}\,\dot{E}_{\text{dis}} - \dot{E}_{\text{back}} - \boldsymbol{\nabla}\cdot\left(\nu^C\,\boldsymbol{\nabla} e\right). \tag{4}$$

The first term on the right-hand side of the equation is a kinetic energy source diagnosed from the dissipative term in the horizontal momentum equation. c_{dis} is a parameter that represents the share of direct energy cascade to microscales. If c_{dis} is smaller than 1, part of the kinetic energy goes to small scales and is dissipated. $(1 - c_{\text{dis}})$ can be interpreted as a hidden sink term for the flow. The second term $-\dot{E}_{\text{back}}$ is a UKE sink (on average) and represents the rate of energy returned to the resolved flow via the backscatter operator. The last term is UKE harmonic diffusion, which redistributes subgrid energy and has a significantly smaller magnitude when compared to the other terms. ν^C is a diffusion coefficient roughly corresponding to the average eddy thickness diffusivity over the baroclinically forced region according to Jansen et al. (2015) but the amplitude of this coefficient is of minor importance (see also discussion in Juricke et al. (2019).

To reduce the contribution from the grid-scale fluctuations (for a discussion, see Juricke et al. (2019)) and to control the scales at which energy is injected into the momentum equation via backscatter, it is necessary to apply a smoothing filter within the following terms: the UKE source term $\dot{E}_{\text{dis}}$, the backscatter term $\dot{E}_{\text{back}}$, and the backscatter contribution $\boldsymbol{B}(\boldsymbol{u}, e)$ to the momentum equation (Eq. (1)) (the corresponding order of amount of smoothing cycles is specified in Table 1). This is implemented by repeated application of a single averaging operator that averages cell centroid quantities to the common cell vertex and then averages the new vertex quantities back to the cell centroids. The effect of filtering involved in $\boldsymbol{B}(\boldsymbol{u}, e)$ will be analyzed later.

2.2 Deterministic backscatter with advection

In this study, we extend Eq. (4) by incorporating full advection of UKE in three dimensions by the velocity field of the resolved flow. The subgrid energy budget equation with the new term has the following form:

$$\partial_t e = -c_{\text{dis}}\,\dot{E}_{\text{dis}} - \dot{E}_{\text{back}} - \boldsymbol{\nabla}\cdot(\nu^C\boldsymbol{\nabla} e) - \boldsymbol{u}\cdot\boldsymbol{\nabla} e \tag{5}$$

We study the effect of UKE advection using a channel and double-gyre setups described in Section 2.4. The flow in the channel setup is statistically homogeneous in the zonal direction so that the regions of KE production and dissipation coincide. This makes it more challenging to analyze the direct effect of the subgrid advection term on local energy transfers. In the double-gyre setup, these regions are separated, which can help to interpret the effects of UKE advection.

2.3 Stochastic backscatter

The second extension of the subgrid kinetic energy model (Eq. (4)) is an additional stochastic term whose spatial pattern is derived by diagnosing the kinetic energy from a high-resolution reference simulation. It aims to improve the missing spatial and temporal variability.

To generate correlated patterns for the stochastic forcing, we first ran a higher-resolution, 10km simulation and calculated kinetic energy for every mesh element for each simulated day of a 9 year simulation. Then we coarse-grained the field to the eddy-permitting mesh by calculating the average amount of kinetic energy over four neighboring cells. This provides us with a coarse-grained field of high-resolution kinetic energy that can then be used to generate correlation patterns for the stochastic term in the UKE equation.

The coarse-grained high-resolution kinetic energy is then decomposed into empirical orthogonal functions (EOFs) and the corresponding set of principal components (PCs) that reflect the temporal dynamics of each EOF, where we retain only the EOF patterns with the largest contribution to the total variance. Here, we choose the cutoff at 50% of the total variance, thereby reducing the number of EOFs from thousands to dozens.

We also attempted to use data on the difference between coarse and fine resolution runs for the EOF decomposition (see Section 3.7 for more information) but decided against it due to the higher computational expense and the lack of a clear physical argument in favor.

Based on this decomposition, we introduce a new stochastic term in the subgrid energy equation (Eq. (4)), which now reads

$$\partial_t e = -c_{\mathrm{dis}}\, \dot{E}_{\mathrm{dis}} - \dot{E}_{\mathrm{back}} - \boldsymbol{\nabla} \cdot (\nu^C \boldsymbol{\nabla} e) + C_1\, e \sum_i \mathrm{EOF}_i(x)\ \mathrm{PC}_i(t)\,. \tag{6}$$

The summation is over i, the ordinal number of the EOF. The corresponding PCs follow Ornstein–Uhlenbeck processes

$$\mathrm{d}\,\mathrm{PC}_i = -\mu_i\ \mathrm{PC}_i\ \mathrm{d}t + \sigma\, \mathrm{d}W_i\,, \tag{7}$$

where the $\mathrm{d}W$ is an increment of the standard Wiener process and the mean reversion rates μ_i are determined by fitting the Euler–Maruyama discretization of Eq. (7), which is an AR(1) process, to daily mean data. For simplicity, the variance parameter σ is taken the same across all the PC_i, and is absorbed into the tuning parameter C_1 which is further discussed in Section 3. To generate realizations for a model run, the stochastic equation is again converted into a time-discrete AR(1) process, but with the actual model time step. Finally, the prefactor e in Eq. (6) is a heuristic choice, corresponding to multiplicative noise in order to avoid over-energizing the calm areas of the flow where the subgrid energy is low.

In Section 3, the effect of the implementations described above will be compared to the impact of the older version of the UKE budget for kinetic energy backscatter following Juricke et al. (2019) (Eq. (4)). The latter already substantially improves the mean state. Despite the general capacity of the backscatter to inject as much kinetic energy as we want, the subgrid is designed to limit this amount of energy input. With stochastic forcing in the subgrid, we could continue to increase the amount of input arbitrarily. However, it will not necessarily make a simulation closer to the high-resolution truth but more energetic and model stability may become an issue. Therefore, the diagnostics introduced in Section 2.7 and the tuning of C_1 focus not only on the mean kinetic energy but also on other flow variables and their variability in order to capture the overall effect of the addition of the stochastic term as part of the UKE budget.

2.4 Simulation setups

We use two different setups of the FESOM2 model, which solves the primitive equations on a quasi-B-grid. The surface mesh is triangular, and there are 40 vertical layers, with layer depth varying from 9 m in the top layer to 370 m in the bottom layer, which divide the domain into small triangular prisms. Both setups are bounded vertically by a flat bottom at a depth of 4000 m. The bottom boundary conditions are taken as linear friction. The viscous operator is a discrete biharmonic operator depending on the difference in velocities between neighboring elements following the formula $\nu_{c'c} = \gamma_0 l_{c'c} + \gamma_1 |\boldsymbol{u}_{c'} - \boldsymbol{u}_c| l_{c'c} + \gamma_2 |\boldsymbol{u}_{c'} - \boldsymbol{u}_c|^2 l_{c'c}$, where c and c' are the neighboring grid cells, $l_{c'c}$ is the length of the edge between the cells, and γ_0, γ_1, γ_2 are the tuning coefficients (for more details see (Juricke et al., 2020)). We use the PP vertical mixing scheme (Pacanowski & Philander, 1981) for both setups. For a discussion of alternative mixing schemes, see Scholz et al. (2022).

The first of two test configurations is a zonally periodic channel following Soufflet et al. (2016). The size of the channel is 4.5° (about 500 km) in the zonal direction and 18° (about 2000 km) in the meridional direction.

The initial density profile changes gradually along the meridional direction as well as vertically (Fig. 2a). It is directly associated with the temperature gradient by a linear equation of state. The gradient allows the model to form a jet in the middle of the channel. To continuously maintain a quasi-stationary turbulent regime, the zonally averaged velocity and temperature fields are relaxed to the initial mean temperature and velocity state in the entire domain.

The Rossby radius of deformation (approximately 20 km in the center and ±5 km from south to north) is governed by the predefined vertical stratification to which the model is relaxed. Thus, we choose a coarse grid consisting of equilateral triangles with 20 km edge length, which is eddy-permitting, and a fine grid where the edge length is 10 km thus (barely) eddy-resolving (see Fig. 1a,b).

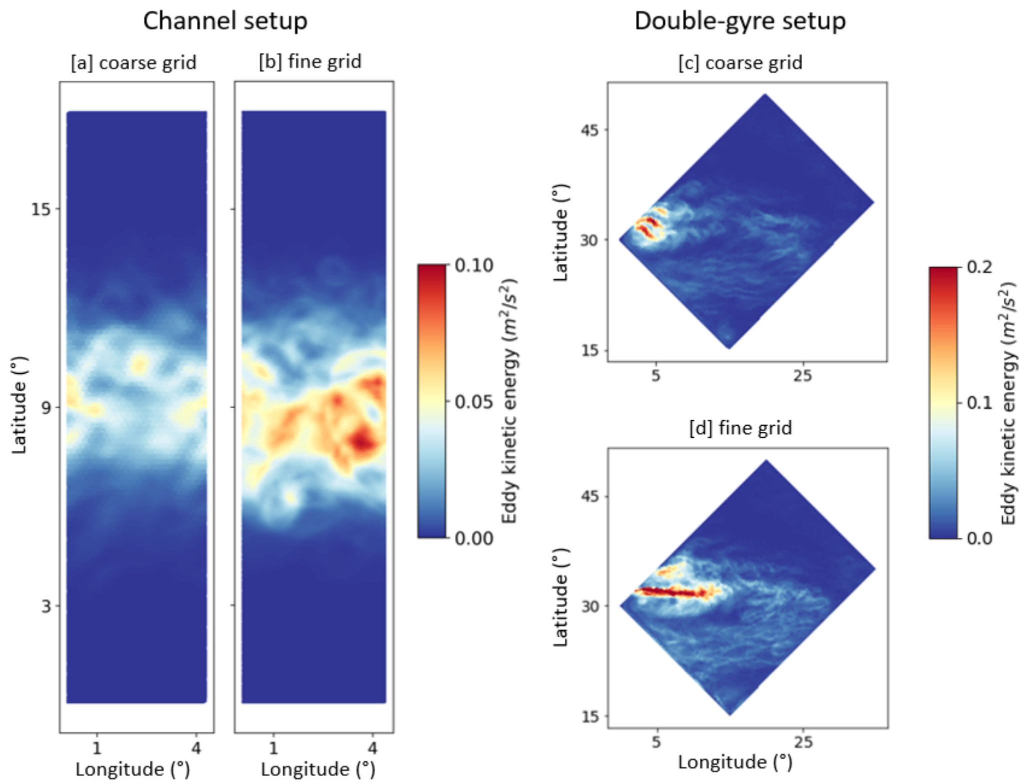

Figure 1. Channel (a,b) and double-gyre (c,d) setups. Annual-mean EKE $[m^2/s^2]$ (after spin-up) for the coarse grid simulation (a,c) and for the fine grid simulation (b,d), which was determined by the formula: $\frac{\overline{u^2}+\overline{v^2}-\overline{u}^2-\overline{v}^2}{2}$. Aerial view of the surface layer.

The second setup follows Levy et al. (2010) and represents a double-gyre configuration, from now on referred to as the DG setup. It uses a rectangular domain with its left corner at 30°N, rotated by 45°. The size of the domain is 28.3° (about 3140 km) on the long side and 21.2° (about 2350 km) on the short side. Vertical walls bound it on all four sides. Here, we use a mesh formed of right-angled triangles instead of equilateral triangles to avoid castellated boundaries. The short sides of the right-angled triangles are equal to 20 km and 10 km, corresponding to the coarse and the high-resolution simulations.

The initial temperature profile follows Pacanowski and Philander (1981) and Levy et al. (2010). It is rapidly nonlinearly decreasing from the surface to a depth of 500 m and slowly linearly decreasing to 0 °C below (Fig. 2b). There is no initial meridional temperature stratification. The initial vertical temperature stratification adjusts during the simulation based on forcing and internal mixing, but due to the depth of the setup, this process takes several decades. Surface forcing is based on a mean northern hemisphere wind stress (Fig. A1b) and heat flux. Wind forcing is an essential flow driver through Ekman pumping. A sinusoidal wind stress profile forces a subpolar gyre in the north and a subtropical gyre in the south, thereby imitating North Atlantic dynamics. The heat flux can be divided into several components, i.e. latent, sensible, and radiative heat flux (Levy et al., 2010). As a simplification, we only use sensible and radiative heat fluxes here. Both enter the surface directly, while radiative heating is also distributed vertically over the first couple of layers according to a solar penetration profile. The heat fluxes then further update the tracer equation via diffusion and mixing. The exact sensible heat flux expression used in the simulation is $-\gamma(T_{\text{ocean}} - T_{\text{atm}})$, where γ is a transfer coefficient and shall be taken to be equal to $4\,\mathrm{W\,m^{-2}\,K^{-1}}$, T_{ocean} - sea surface temperature, and T_{atm} - apparent air temperature (Fig. A1a). The solar radiation model (Fig. A1c) takes losses due to cloudiness, reflection and albedo into account. Latent heat flux due to evaporation is neglected, and so is any freshwater flux (i.e., salinity is constant).

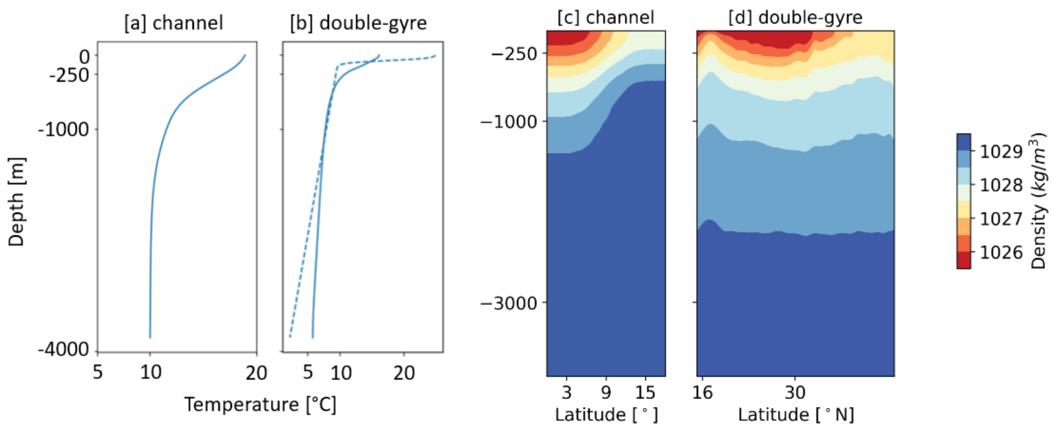

Figure 2. Vertical temperature and density profiles. Panel (a) shows the initial vertical temperature stratification in the channel, while panel (b) displays both the initial (dashed line) and equilibrium (solid line) vertical temperature stratification in the double-gyre setup. Panel (c) shows the annual mean of the vertical density profile along 2.5° longitude in the channel, and panel (d) shows the annual mean of the vertical density profile along 15° longitude in the double-gyre setup after spin-up.

We use cartesian geometry for the channel setup (i.e., we replace the cosine of latitude by one) and spherical geometry for the double-gyre simulation. For the Coriolis parameter, we use the β-plane approximation $f = f_0 - \beta d$, where d is the meridional distance from the zero-degree latitude. The constants here and above are chosen to agree with those originally proposed for these test cases, and are specified in Table A1.

Fig. 2c,d show the stratification of both setups. It is evident that the double gyre has a more complex vertical stratification that changes with integration time until it reaches a (quasi-)equilibrium state, while for the channel, stratification is continuously relaxed back to the initial state.

2.5 How much filtering is necessary?

The use of filters as described in Section 2.1 raises the question of whether shielding the system from small-scale noise could interfere with the impact of the subgrid advection term as advection and smoothing both affect where and at which scales energy is reinjected. In this context, we also want to revisit the question of how much smoothing is really necessary to ensure sufficient scale separation between injection and dissipation range for the energy cascade. Thus, we ran additional simulations, where we reduced the number of filter cycles for the contribution of backscatter in the momentum equation to zero (i.e., in $\boldsymbol{B}(\boldsymbol{u}, e)$ in Eq. 1). We ran these tests with and without subgrid advection.

2.6 Spin-up

Both setups start with appropriate temperature stratification and a small initial perturbation, which leads to the emergence of turbulence in a short time, as evidenced by the growth of kinetic energy over the first year (Fig. 3) and by the presence of eddies in the vorticity field (not shown).

The channel simulation reaches a statistically steady state after a little more than one year, maintained by the relaxation of the velocity and temperature fields. For our diagnostics, we thus take nine years after a single spin-up year. In the DG setup, isopycnals become inclined because of Ekman pumping in the southern part of the domain and Ekman suction in the northern part of the domain as a consequence of the sinusoidal wind forcing. This process is much slower, so we require a 50-year spin-up to reach a quasi-equilibrium state.

Besides the difference in spin-up time, Fig. 3 also indicates different levels of surface KE fluctuation between the two setups. The comparatively larger fluctuations in the channel vs. double-gyre are explained by the fact that the channel is narrow in the zonal direction and, therefore, cannot host many eddies simultaneously. As a result, the resolved EKE fluctuates greatly along the eddy life cycles. To minimize the fluctuation effect, we use 9-year averaging for both setups, i.e., a simulation length of 9 years after the respective spin-up.

Overall, we use the DG setup as an extension of the idealized zonally-periodic channel setup as it has better-defined areas of creation and dissipation of kinetic energy and is longer in the zonal direction, which allows eddies to develop and evolve in space. In addition, the DG setup could be extended to include more complicated and realistic coastlines and bottom topography. One of our aims is to understand how the complexity of the setup influences the effectiveness of the default backscatter of Eq. (4) itself and the new subgrid energy components of Eqs. (5) and (6) implemented in this study.

2.7 Diagnostics

We examine a set of mean quantities calculated for each vertical layer z to diagnose the effect of our changes in the subgrid equation. As a main diagnostic, we use vertical profiles of the area-averaged layer-wise mean eddy kinetic energy

$$\mathrm{EKE}(z) = \overline{\sum_i \tfrac{1}{2}\left((u(z) - \overline{u(z)})_i^2 + (v(z) - \overline{v(z)})_i^2\right) A_i \Big/ \sum_i A_i}\,, \tag{8}$$

where A_i denotes the area of grid cell i, and the overbar denotes the time average of 9 years. We also examine the vertical profiles of the root mean square of vertical velocity anomalies,

$$w_{\mathrm{RMS}}(z) = \sqrt{\overline{\sum_j (w(z) - \overline{w(z)})_j^2\, B_j \Big/ \sum_j B_i}} \tag{9}$$

where j denotes the vertex index and B_j is the area of the median-dual cell associated with vertex j. As they show the amplitude of the time-averaged vertical velocity fluctuations

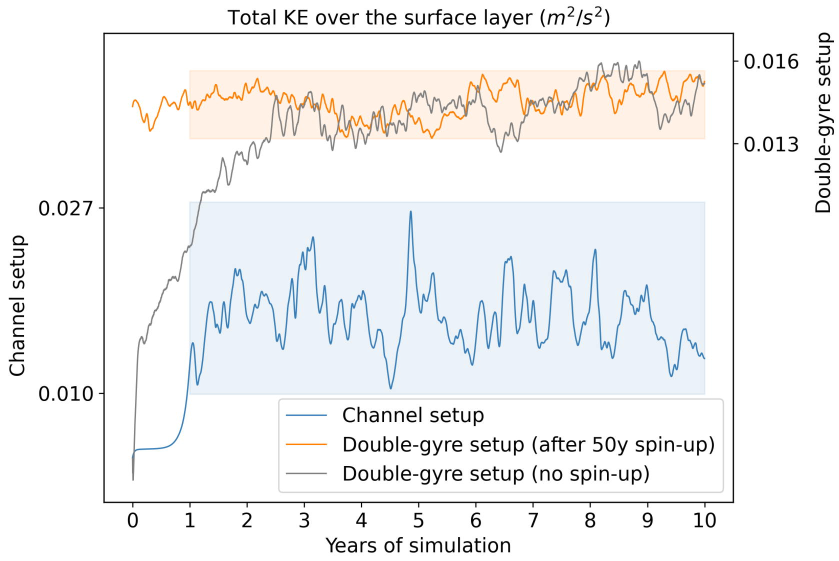

Figure 3. The variability of total surface kinetic energy over time. The blue line represents a 10-year simulation of the channel setup. The highlighted solid blue box indicates the 9 years chosen for analysis, excluding the first spin-up year. After a 50-year spin-up, the orange line corresponds to the double-gyre setup, with the 9 years chosen for analysis indicated by a solid orange box. The grey line indicates the amplitude of the initial drift of the double-gyre setup.

for each vertical layer, they enable the detection of vertical fluctuation anomalies that may appear due to the wrong viscosity and backscatter settings. The different cell areas in Eq. (8) vs. (9) arise because in FESOM2, scalars and pressure are located on vertices while horizontal velocities are located on centroids. Lastly, vertical profiles of buoyancy flux, which characterizes the vertical profile of the release of APE, are computed as

$$\overline{w'\,b'(z)} = \overline{\sum_j (w(z) - \overline{w(z)})_j \, (b(z) - \overline{b(z)})_j \, B_j \Big/ \sum_j B_j} \,. \tag{10}$$

An abnormal change in RMS vertical velocity (Eq. (9)) and in the structure of APE release (Eq. (10)) could indicate an excitation of nonphysical waves, or otherwise changing stratification and dynamics (as is often seen when varying the grid resolution).

Taking the scalar product of the horizontal momentum equation (Eq. (1)) with $\boldsymbol{u}_\mathrm{h}$, we obtain an evolution equation for the (horizontal) kinetic energy density,

$$\frac{1}{2}\partial_t|\boldsymbol{u}_\mathrm{h}|^2 = -\boldsymbol{u}_\mathrm{h}\cdot(\boldsymbol{u}_\mathrm{h}\cdot\boldsymbol{\nabla}_\mathrm{h})\boldsymbol{u}_\mathrm{h} - \frac{1}{\rho_0}\boldsymbol{u}_\mathrm{h}\cdot\boldsymbol{\nabla}_\mathrm{h}p + \boldsymbol{u}_\mathrm{h}\cdot\boldsymbol{V}(\boldsymbol{u}_\mathrm{h}) + \boldsymbol{u}_\mathrm{h}\cdot\partial_z(\nu_v\,\partial_z\boldsymbol{u}_\mathrm{h})\,. \tag{11}$$

The pressure gradient work term $-\frac{1}{\rho_0}\boldsymbol{u}_\mathrm{h}\cdot\boldsymbol{\nabla}_\mathrm{h}p$ is the source term for the integrated kinetic energy. In the case of the DG setup, wind forcing is either a source or a sink and comes to the system via the last term in Eq. (11). In the case of the channel setup, the relaxation of the zonal mean profile to the prescribed one acts as a source for mean KE.

Integrating the three-dimensional pressure work term over a volume, using incompressibility and hydrostatic balance (Eq. (2)), we obtain

$$\frac{1}{\rho_0}\boldsymbol{u}_\mathrm{h}\cdot\boldsymbol{\nabla}_\mathrm{h}p = \nabla(\boldsymbol{u}p) + wb\,. \tag{12}$$

Integrating over some domain, the divergence term on the RHS of Eq. (12) becomes less important, and it will be zero if one integrates over the entire flow domain (no pressure flux through the boundaries).

A similar expression holds for the anomalous, i.e., eddy part of the pressure gradient work and buoyancy flux. In this study, we focus on the eddy part $w' b'$ and take it as a local diagnostic for the transfer from APE to KE even though, strictly speaking, it only holds in an (sufficiently large) area-integrated sense.

As an essential part of diagnostics, we compute the horizontal power spectra of the different contributions to the viscous and backscatter parameterizations. In order to use the discrete Fourier transform, we interpolated first to a regular quadrilateral grid. Then the 2D spectra are condensed to 1D spectra by integrating over an annulus of unit width in wavenumber space. Here, we apply cubic interpolation for kinetic energy and nearest-neighbor interpolation for the dissipation power following the results of Juricke et al. (2023), motivated by the smooth nature of the kinetic energy field and the non-smooth, discrete representation of the dissipation and backscatter operators.

The DG setup was simulated and calculated, assuming a spherical geometry. Hence, it was necessary to convert the grid and vector fields into Cartesian coordinates before performing interpolation. We first transformed the mesh and velocities to a new spherical system of coordinates such that the center of the domain is at the equator. After this transformation, we selected the central rectangular area of the domain (see the box in Fig. 4) for further interpolation and Fourier transform.

Spectra are computed as an average of the daily output for nine years and limited horizontally by the wavenumber π/h, where h is the height of an equilateral grid triangle (see discussion in Juricke et al., 2023). h_c is the height of the coarse grid triangle, and h_f is the height of the fine grid triangle in the channel. In the case of the DG setup, one should stop at the wavelength of $2h$, i.e., wavenumber π/h, where h is the smaller side. The limiting wavenumber depends on direction: it is π/h along small sides and $\sqrt{2}\pi/h$ in the direction along and perpendicular to the large side. Since we are willing to discuss spectra averaged over angles, we have to stop at π/h.

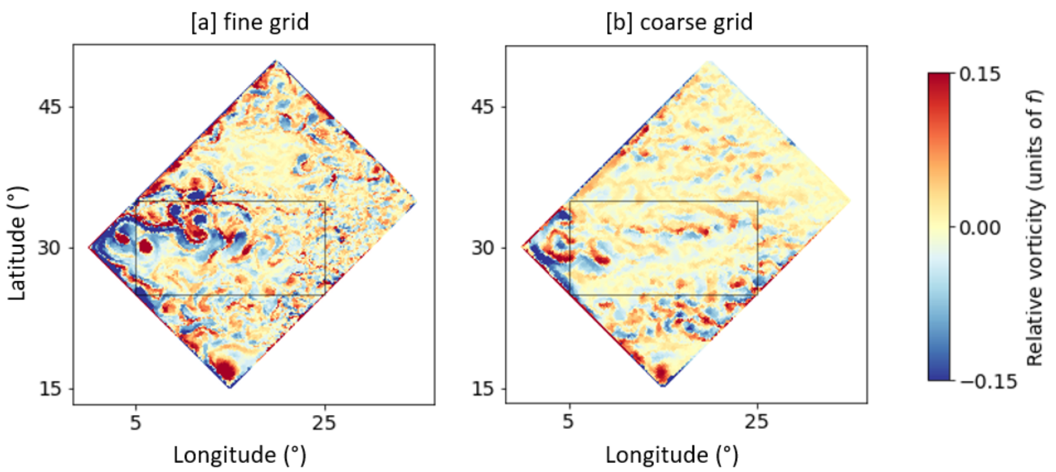

Figure 4. A snapshot of the relative vorticity in the double-gyre setup, showing the designated area for Fourier decomposition (black box).

As a final diagnostics, here specifically for the DG setup, we evaluate vertical density profiles. As mesoscale eddy parameterizations ultimately strive to reproduce a precise representation of the ocean stratification, we examine the alignment of the isopycnal contours with those of the reference simulation.

3 Results

3.1 Matrix of numerical experiments

We performed a matrix of simulations where we tested the different parameterization choices introduced in Section 2 for each of the setups. A summary of simulations is given in Table 1. The 10 km simulation is the high-resolution reference, the 20 km is the low-resolution reference without backscatter. Both use biharmonic viscosity with a variable coefficient designed to dissipate grid scale motion following Juricke et al. (2020). The other simulations are also on the low-resolution 20 km grid and include backscatter with and without the advection and stochastic terms.

Table 1. An overview of the essential parameters for the simulation setups. Δx is a side of an equilateral grid triangle for the channel simulation. For the double-gyre simulation, Δx corresponds to the smallest side of a right-angled grid triangle.

Simulation name	Δx (km)	Smoothing cycles	Backscatter	Subgrid advection	Stochastic backscatter amplitude
20 km	20	(2,2,4)	no	no	no
20 km+BS	20	(2,2,4)	deterministic	no	no
20 km+BS (no BS filter)	20	(2,2,0)	deterministic	no	no
20 km+BS+ADV	20	(2,2,4)	deterministic	yes	no
20 km+BS+ADV (no BS filter)	20	(2,2,0)	deterministic	yes	no
20 km+SBS (high)	20	(2,2,4)	stochastic	no	high
20 km+SBS (middle)	20	(2,2,4)	stochastic	no	middle
20 km+SBS (low)	20	(2,2,4)	stochastic	no	low
20 km+SBS (middle)+ADV	20	(2,2,4)	stochastic	yes	middle
20 km+SBS (low)+ADV	20	(2,2,4)	stochastic	yes	low
10 km	10	(2,2,4)	no	no	no

3.2 Eddy-permitting simulations are overdissipative

To assess the effects of incorporating the new components into the subgrid energy budget, we first look at changes in eddy kinetic energy (Fig. 5a,b) for the simulations that only have the viscosity parameterization. Comparing the simulation results for "20 km" (grey line) and "10 km" (black line), we observe that the low-resolution simulation has a significant EKE deficit for the DG, even more than in the channel.

Variability of the vertical velocity also differs greatly between the two resolutions (Fig. 5c,d), but here with opposite tendencies between the two setups. For the DG, vertical fluctuations at low resolution are larger, while it is the opposite for the channel, but also located at greater depth as compared to the high-resolution reference.

Buoyancy fluxes, which serve as an indicator of APE release, are substantially reduced at low resolution for both simulations (Fig. 5e,f), especially the near-surface peak is much weaker. In the DG setup, moreover, a significant reduction of energy production is observed along the entire water column.

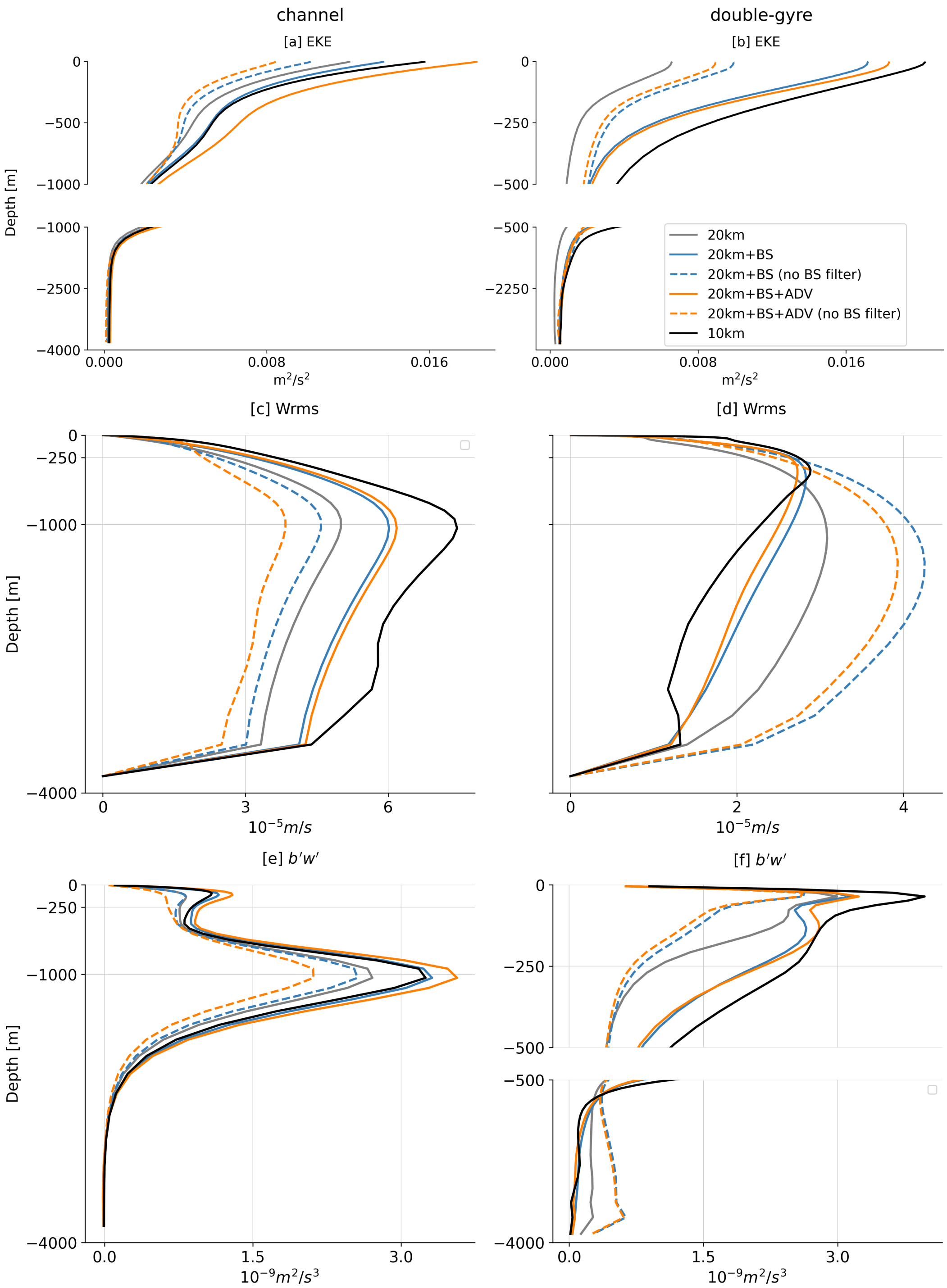

Figure 5. Vertical profiles for the channel setup (left column) and the double-gyre setup (right column). Each setup includes layer and time-averaged (9 years) diagnostics for EKE $[m^2/s^2]$ (a, b), the RMS vertical velocity anomalies $[m/s]$ (c,d), and buoyancy flux $[m^2/s^3]$ (e,f). Figures a, b, and f have a gap on the vertical axis.

3.3 Dynamic backscatter improves the energy cycle

We first switch on dynamic backscatter as in Juricke et al. (2019). This improves all diagnostics on the coarse grid toward the values on the fine grid (solid blue line in Fig. 5).

We note, in particular, that the point of maximum vertical velocity variability in the DG setup moves closer to the surface, as it should (Fig. 5d). Moreover, the upper part of the buoyancy flux profile for the channel becomes more distinct with backscatter, hence agreeing with Soufflet et al. (2016) who observe a dominant peak (due to mesoscale instability) at 1000 m depth and a secondary isolated peak (due to submesoscale instability) closer to the surface. For the DG setup, mesoscale production is the most improved (Fig. 5f).

3.4 Impacts of advection of subgrid energy

When the advection term is included in the subgrid equation, it improves the backscatter effect, bringing it even closer to the high-resolution truth for both setups (solid orange line on Fig. 5a,b). For the channel setup, subgrid advection increases EKE beyond what is observed in the 10 km reference. This is not necessarily a negative result because we do not resolve the full eddying flow even at 10 km resolution (Soufflet et al., 2016).

For both setups, the presence of advection in the subgrid correctly shifts the profile of RMS vertical velocity to the direction of the high-resolution truth, although the amplitude of the shift is small (Fig. 5c,d). The profile of RMS vertical velocity is a convenient diagnostic of instabilities in the deep ocean. Such instabilities may occur when background viscosity is too small (see Juricke et al. (2020). Here, we do not see any indication of the onset of instability, with or without subgrid advection. In the DG, vertical velocity variability even decreases when advection is included, which indicates that subgrid advection does not induce spurious waves. At the same time, subgrid advection *enhances* the production of APE near the peaks (Fig. 5e,f), thereby reducing biases in energy production.

We conclude, based on the vertical profile diagnostics, that adding the advection term to the subgrid equation has a positive effect, with different changes depending on the setup.

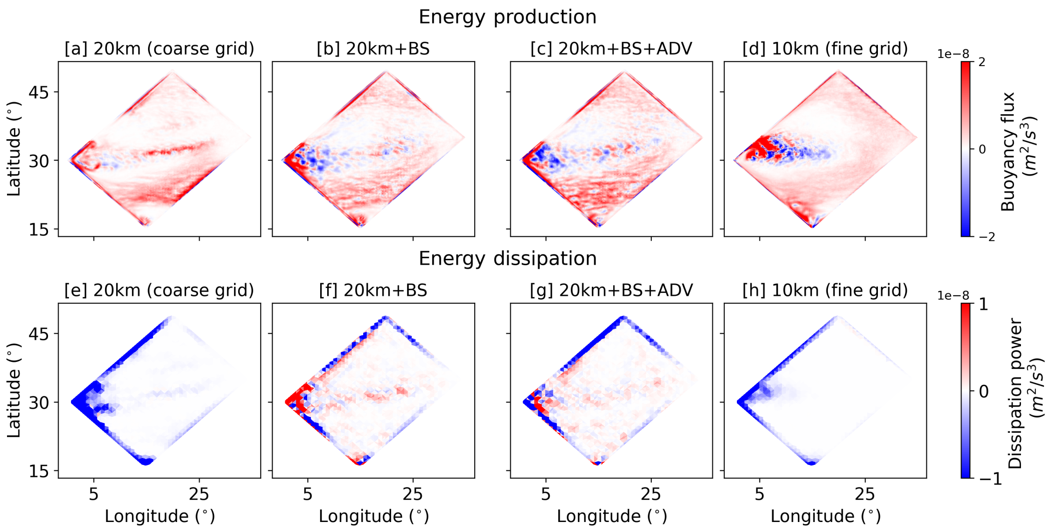

Figure 6. The 9-year average of 2D buoyancy flux $[m^2/s^3]$ (a-d) and the 9-year average of the dissipation power $[m^2/s^3]$ (e-h) computed as the dot product of the velocity field and its dissipation tendency. The dissipation field is also coarse-grained to the 100 km grid. Plots are provided for the following DG configurations: coarse resolution simulation (a,e), coarse resolution with deterministic backscatter (b,f), coarse resolution with deterministic backscatter and subgrid advection (c,g), and fine resolution simulation (d,h).

This conclusion is supported qualitatively by a two-dimensional horizontal view of the production term, see Fig. 6, which shows the buoyancy flux at the maximum level and the dissipation power on the surface level for the different configurations. Both diagnostic fields exhibit significant fluctuations. In order to better distinguish between areas of dissipation and anti-dissipation, we conservatively remapped the dissipation field to a coarse mesh with 100 km resolution. Due to subgrid advection, the central jet's energy production areas are extended, reaching further into the jet domain, albeit the jet is in the wrong position compared to the high-resolution simulation (Fig. 6c). Additionally, subgrid advection prevents backscatter work in the border layer, as demonstrated in Fig. 6g. With the addition of advection, backscatter now focuses primarily on the eddy regions within the domain, resulting in a more physical process representation.

3.5 Spectral diagnostics

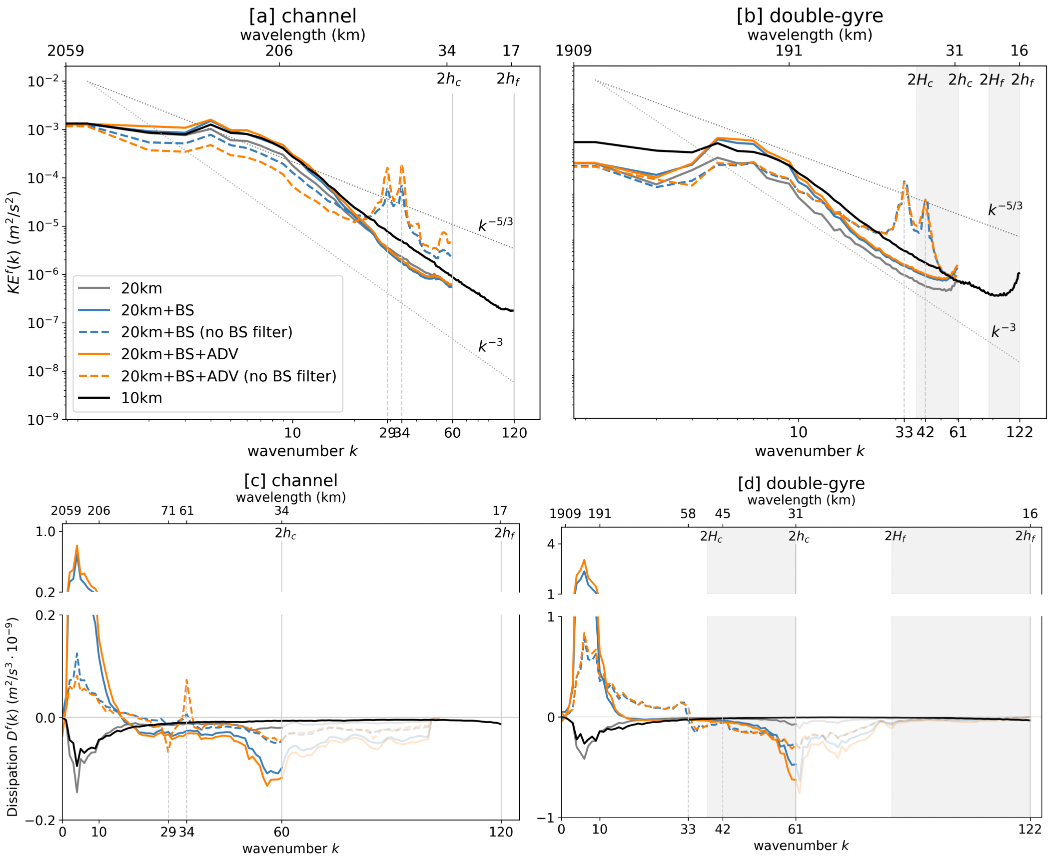

Figure 7. Kinetic energy and dissipation spectra for the channel and DG setups average over 9 years. The vertical lines show the largest wavenumbers (smallest wavelength) on coarse and fine meshes.

Spectral diagnostics of EKE (Fig. 7a,b) show the expected scalings (i.e., $-5/3$ and -3) are in some ranges of wavenumbers, and a relatively early (i.e., at low wavenumbers) deviation from these spectral slopes in the 20 km simulation without backscatter. Backscatter significantly increases the energy level, especially at mid-range without adding much energy to the small scales (which is generally not desirable for reasons of numerical stability). Including advection results in a minor positive change to KE across all scales. For channel, a rather close agreement is reached between the simulations with backscatter and high-resolution simulation (and slightly overperforms after adding subgrid advection). For the DG, the level of KE is still deficient at very small and large scales, even with subgrid advection.

In all DG simulations, one can observe a spectral density pile up near the finest grid scale ($2h_c$). While this is generally seen as related to insufficient dissipation, the same effect can be observed in channel simulations when considering the finest grid scale and has been (at least partially) identified as an artifact of the interpolation from the triangular to a rectangular grid when computing Fourier spectra (Juricke et al., 2023).

Dissipation power spectra (Fig. 7c,d) show the total dissipation (in the case of simulations with the purely viscous closure without backscatter) or the sum of total dissipation and backscatter (in the case of simulations with backscatter) across scales. One might expect that viscous dissipation is concentrated at small scales. However, if the resolution is insufficient, it affects all scales and peaks at scales where the energy content is maximal (also see the discussion in Soufflet et al., 2016). On the other hand, backscatter has a distinct injection maximum at large scales and a dissipation maximum at small scales. The points where the dissipation power spectrum crosses the k-axis mark the scales at which there is a change from energy dissipation to energy injection. When there are more smoothing cycles, the point of intersection moves towards larger scales. Conversely, reducing smoothing causes the intersection point to shift towards smaller scales. The 20 km simulation without backscatter is more dissipative than the 10 km, and the influence of dissipation is mostly at the long-wave part of the spectrum. This changes completely with backscatter: energy is injected on large scales, propagates in both directions of the energy cascade, and actively dissipates along the direct cascade on smaller scales. We observe that the added subgrid advection component enhances the backscatter effect on the large scales and dissipation near the grid scales. Subgrid advection acts as a field catalyst, increasing total kinetic energy and total (positive and negative) dissipation over the full range of scales. It does not, however, noticeably affect the scale at which the overall dissipation (small scales) changes to backscatter (large scales).

3.6 Sufficient filtering is important

Insufficient backscatter smoothing causes significant deviations for all diagnostics. When disabling the filter in the backscatter operator, we observe a loss of energy for all simulations (dashed lines in Fig. 5a,b,c,d). For the channel, the performance is even worse than the 20 km simulation without backscatter (Fig. 5a,b). Concerning vertical velocity (Fig. 5c,d), it either substantially enhances variability (DG) or reduces it (channel). We also observed significant unphysical fluctuations on small scales in the energy spectra (Fig. 7a,b). The further detrimental impact of insufficient smoothing is seen in snapshots of the vorticity fields: Eddies and filaments get a highly distorted “patchy” structure and do not propagate in a physically fully coherent way (not shown).

The simulations with insufficient backscatter filtering illustrate the minimal scales where non-smoothed backscatter injects energy into the system. In the case of the channel setup (Fig. 7c), we observe the additional isolated peaks of energy injection (wave number 34) and energy dissipation (wave number 29). They coincide with the double peaks in KE (Fig. 7a). The general nature of the two kinetic energy peaks (consistent between the setups) can only be speculated at this point but may relate to the formulation or filtering of the subgrid, which determines the backscatter coefficient or, most likely, they are a product of the procedure of collapsing spectra from 2D to 1D, where different directions in the grid may show up as two peaks.

We do not exclude the potential interference between the role of advection and the degree of backscatter operator smoothing, as both affect the locality of the backscatter parameterization. However, insufficient scale separation between dissipation and backscatter causes serious flow deviations and is an inadequate parameterization option for FESOM2. At this point, a generalization to other grid types regarding smoothing can not be made.

3.7 EOF analysis

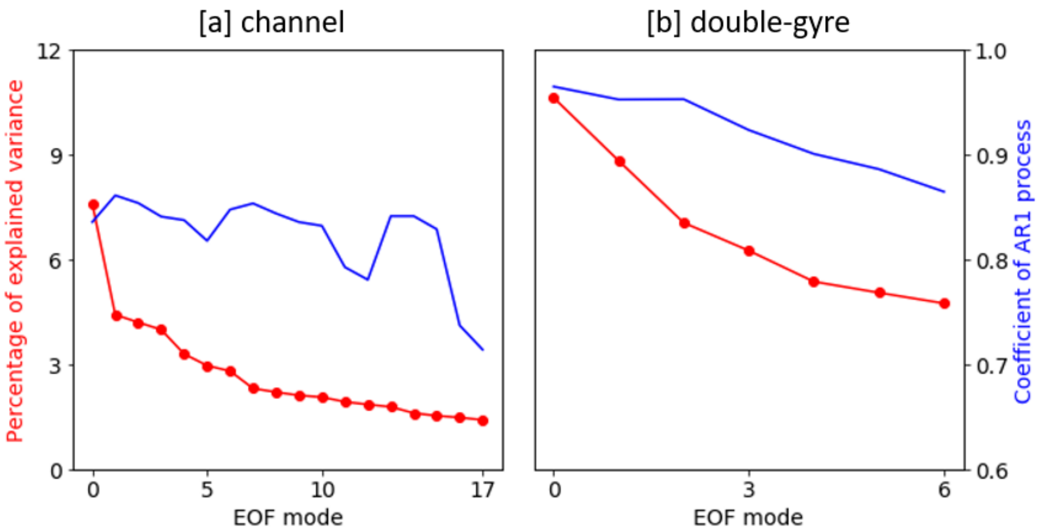

Figure 8. The explained variance and the fitted coefficient for the AR(1) process are listed for each EOF mode.

The first EOFs of the kinetic energy of the high-resolution simulation correspond to the highest variability of KE and are determined by the fluctuations of the mean flow. The presence of a strong localized jet in the DG setup allows the first few EOFs to be relatively large-scale and to capture a large part of the variability in KE, whereas the removed mean flow variability of the channel setup makes the first EOFs already much more small-scale. Constructing the spatial correlation of the stochastic subgrid term based on EOFs with very fine local structures can excite undesirable noise. This needs to be kept in mind and treated with caution. To explain a reference percentage of variability (i.e., 50% in our case), one needs to consider 18 EOFs for the channel setup and only 7 EOFs for the DG setup (see Fig. 8). The reduction of the fitted coefficients of the autoregression process for the corresponding PC accompanies the decrease in the explainable capacity of the EOFs. We are getting shorter correlation times for the higher EOFs with patterns of smaller scales.

As an alternative approach, we also calculated the kinetic energy difference between the coarse-grained data and the output of a coarse-resolution simulation instead of just the pure coarse-grained high-resolution kinetic energy. Through this second approach, we could take the systematic differences in kinetic energy between the outputs of simulations with different resolutions to generate meaningful EOF patterns of missing kinetic energy variability. In the following, however, we will focus on the initial approach, i.e., the patterns generated directly from the kinetic energy data of the coarse-grained high-resolution data. The reason for this is that for the second approach, it was necessary to keep substantially more EOF modes (more than twice as many) to retain 50% of variability, leading to a much more small-scale structure of stochastic forcing patterns that could potentially cause model instabilities and undesired excitation of grid-scale noise. Another reason is that eddy formation differs between high and coarse resolutions. For instance, a large eddy in high resolution does not always align with the eddy pattern observed in coarse resolution, as examined in the analysis of relative vorticity dynamics (not shown). Thus, we have not found enough reasons to alter our method of selecting data, but other options on how to create the EOF patterns are possible.

3.8 Impact of the stochastic subgrid energy source

Based on the magnitude of the other terms in the subgrid energy equation, we selected three options for the coefficient C_1 in Eq. (4): $C_1 = 0.001$, which corresponds to "low"-intensity noise (simulation "20 km+SBS(low)"), $C_1 = 0.005$ corresponding to "middle"-intensity noise (simulation "20 km+SBS(middle)"), and $C_1 = 0.01$ (channel) or $C_1 = 0.008$ (DG) corresponding to the maximum amplitude that does not cause the model to become numerically unstable ("20 km+SBS(high)").

The first result of our simulations is that we can significantly enhance the model's kinetic energy levels via stochastic backscatter while preserving stability. We observe the energizing of the surface layers in the vertical energy profiles (Fig. 9a,b) for all noise categories and, in particular, the energy increase beyond the reference simulation for the "strong" noise. We also find a good agreement of kinetic energy in the reference simulation for the spectra at large scales (Fig. 10), which indicates that we are able (at least partially) to reproduce the spectral slope using the stochastic subgrid energy equation. On the other hand, the vertical energy profile shows unphysical energy growth in the lower layers of the model when using the "strong" stochastic term. It is possible that a more careful tuning of the amplitude as a function of z might mitigate this problem. However, this would be at the expense of introducing yet more tuning parameters so that we restrict ourselves to testing with the stated form of multiplicative noise with simple amplitude tuning. Diagnostics of vertical velocity anomalies (Fig. 9c,d) reveals that, especially in the case of the channel setup, the high-amplitude stochastic term doesn't reflect the ocean behavior at depth, and therefore, this amplitude is outside of the possible range.

Snapshots of relative vorticity for the DG (Fig. 11) show that stochastic backscatter energizes the field with eddies, especially along the jet area. However, we observe increased eddy activity in the northern part of the DG domain that does not correspond to the high-resolution truth. This effect can be caused by insufficient EOF selection, poor fitting of the principal components, a locally overly large noise amplitude, or by the performance of the EOF approach itself.

We nevertheless confirmed the presence of additional eddy dynamics along the jet (see Fig. 11d,e) and an improvement of the kinetic energy spectra curve across the full range of scales (see Fig. 10). Our concern about near-grid-scale noise caused by the stochastic component was not confirmed for the DG setup.

The results for the channel setup showed a worse performance of the EOF approach: we obtained small-scale growth of kinetic energy (Fig. 10a), which could be explained as a spurious wave generation caused by the stochastic backscatter. Thus, the robustness of the stochastic component, in particular, depends on the flow characteristics and noise amplitude of extracted EOF patterns, which should be sufficiently large-scale. This property was also validated when analyzing the simulations using not total high-resolution KE data but the data of KE difference between two resolutions. In this case, the model diagnostics showed a worsening in energetics compared to the high-resolution KE-based EOFs and the relative vorticity field (not shown).

3.9 Combined effect of subgrid advection and stochastic forcing

Our final set of simulations assesses the combined effect of stochastic and advection subgrid terms. Global diagnostics are summarized in Table 2. It shows generally favorable improvements when using some form of backscatter and, in particular, reasonable performance when using both new subgrid terms together. However, it is difficult to pick a clear winner. We therefore turn to discuss further: SSH differences as well as vertical density

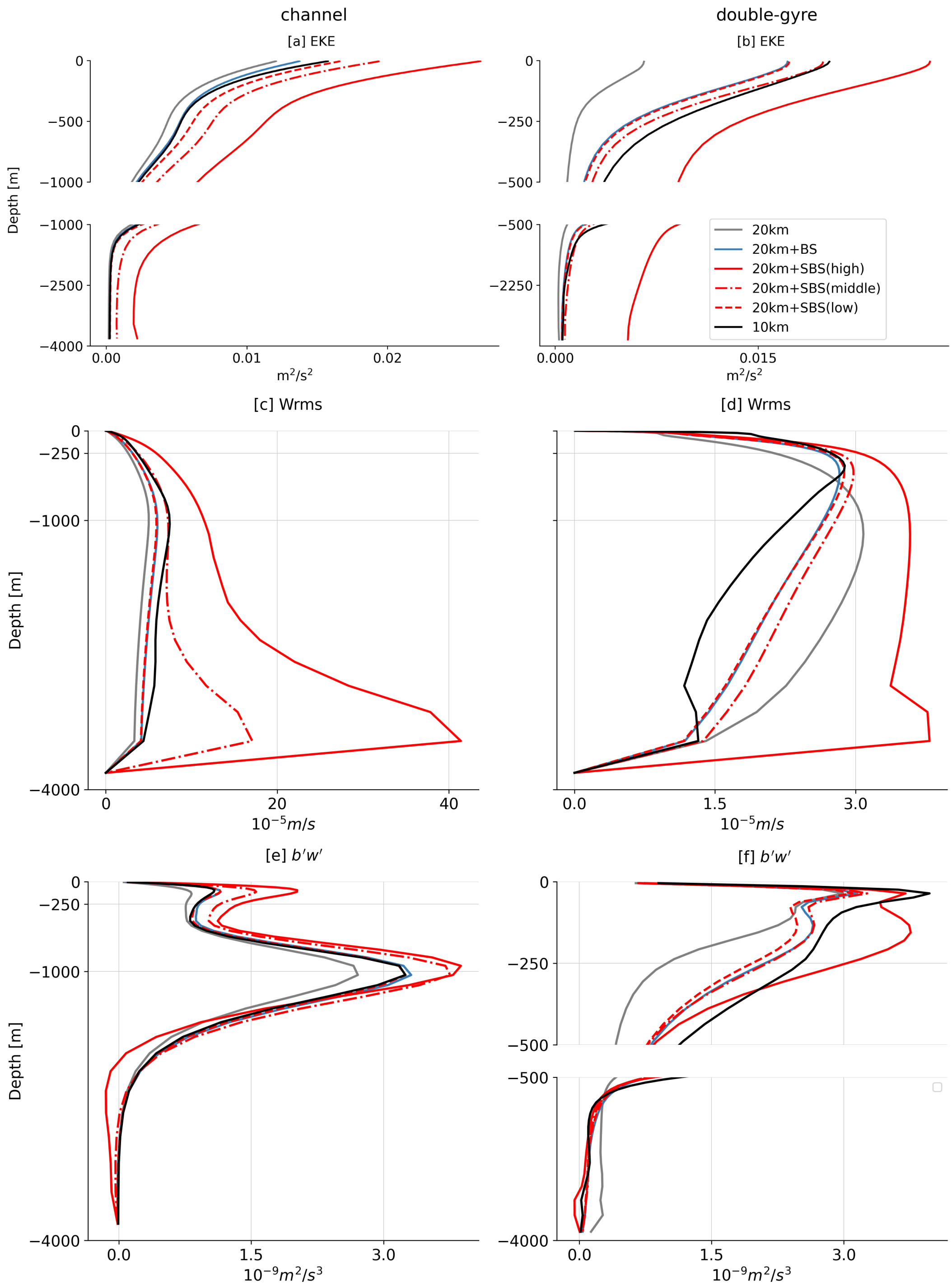

Figure 9. Vertical profiles for the channel setup (left column) and the double-gyre setup (right column) after incorporating stochastic terms of varying amplitudes. Each setup includes layer and time-averaged (9 years) diagnostics for EKE $[m^2/s^2]$ (a, b), the RMS vertical velocity anomalies $[m/s]$ (c,d), and buoyancy flux $[m^2/s^3]$ (e,f). Figures a, b, and f have a gap on the vertical axis.

profiles. For conciseness, we limit the discussion to the more realistic DG setup and also restrict to the low (C_1=0.001) and middle-intensity (C_1=0.005) cases for the stochastic term

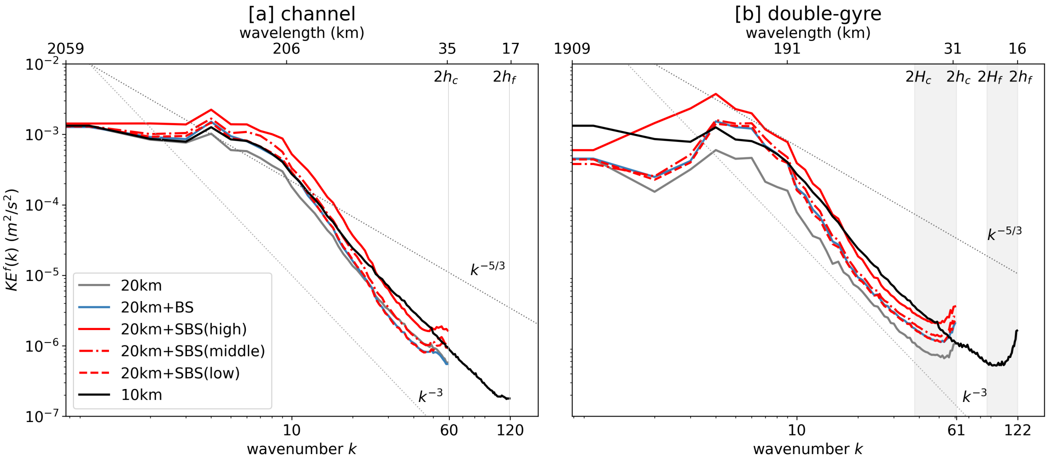

Figure 10. Kinetic energy spectra for different amplitudes of stochastic term. A dashed red line represents the spectra of the low-amplitude stochastic term on the subgrid and is almost identical to the spectra of the deterministic backscatter simulation data. The dashed-dotted and solid red lines represent data simulated with middle and high-amplitude stochastic terms, respectively.

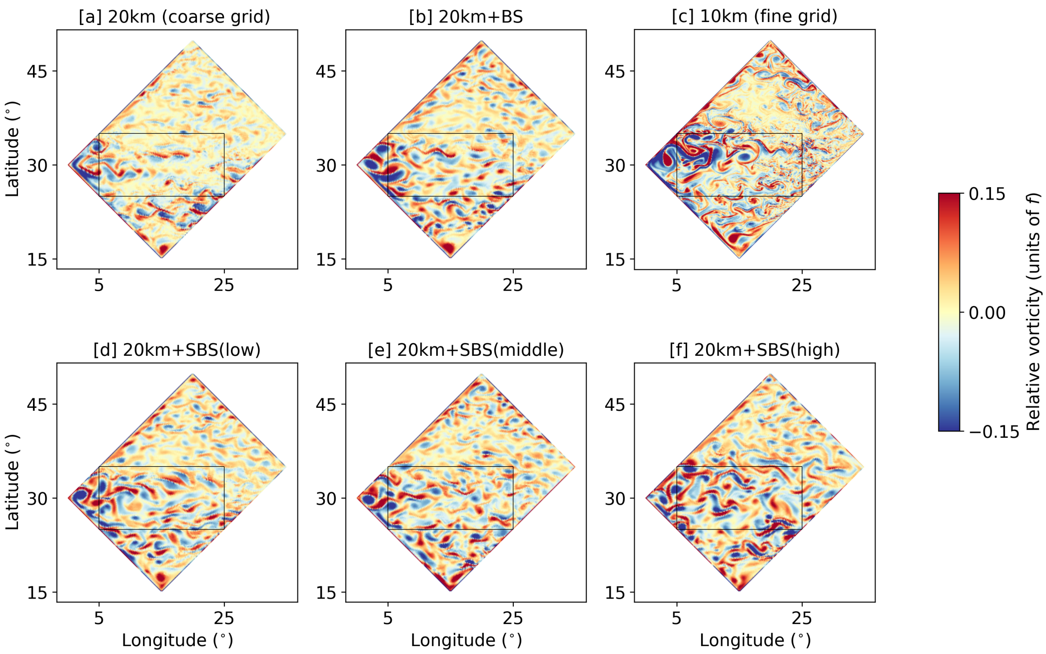

Figure 11. Snapshots of relative vorticity for coarse resolution without backscatter (a), coarse resolution with deterministic backscatter (b), fine resolution (c), and coarse resolution with varying stochastic backscatter amplitudes (d-f). The black boxes show the designated area for Fourier decomposition.

as the the large amplitude case has already been rejected as performing poorly (see Fig. 9 and the discussion in Section 3.8).

The SSH diagnostics show the time-averaged SSH for the coarse-grid simulation without backscatter (Fig. 12a), coarse-grid simulation with backscatter (Fig. 12b), and the

Table 2. Summary of global diagnostics, averaged over a 9-year period, comparing the various subgrid model options relative to the high-resolution reference, which is normalized to 100 %, except for RMSE $\overline{SSH}$, where high-resolution simulation corresponds to 0. The top-performing results for each diagnostic are set in red. It should be noted that the high-resolution reference is not the final truth when it comes to, e.g., KE, as at even higher resolution, it will be more KE. The vertically integrated buoyancy flux is taken over the top 500 m for the double-gyre setup.

Diagnostic variable	Setup	20 km	20 km+BS	20 km+BS+ADV	20 km+SBS (low) - 20 km+SBS (middle)	20 km+SBS (middle) +ADV	10 km
Surface KE m/s^2	CH DG	0.0170 (82%) 0.0144 (44%)	0.0209 (101%) 0.0252 (76%)	0.0232 (112%) 0.0262 (81%)	0.0216 - 0.0246 (104 -119%) 0.0256 - 0.0281 (79-86%)	0.0215 (104%) 0.0266 (82%)	0.0207 (100%) 0.0325 (100%)
Surface EKE m^2/s^2	CH DG	0.0121 (77%) 0.0066 (33%)	0.0137 (87%) 0.0171 (84%)	0.0182 (115%) 0.0183 (90%)	0.0167 - 0.0194 (106-123%) 0.0173 - 0.0198 (85-98%)	0.0164 (104%) 0.0199 (98%)	0.0158 (100%) 0.0203 (100%)
max $(b' w')$ $10^{-9}\,m^2/s^3$	CH DG	2.71 (83%) 2.99 (75%)	3.31 (122%) 3.15 (79%)	3.56 (133%) 3.24 (82%)	3.25 - 3.75 (100-138%) 3.10 - 3.26 (78-82%)	3.32 (123%) 3.23 (81%)	3.25 (100%) 3.97 (100%)
vert. int. $(b' w')$ $10^{-6}\,m^3/s^3$	CH DG	2.68 (84%) 0.68 (54%)	3.32 (104%) 1.01 (81%)	3.58 (113%) 1.03 (82%)	3.25 - 3.76 (102-118%) 0.96 - 1.02 (77-82%)	3.30 (104%) 1.01 (81%)	3.18 (100%) 1.25 (100%)
RMSE $\overline{SSH}$ (%)	DG	0.110	0.066	0.050	0.046 - 0.054	0.057	0

fine-resolution simulation (Fig. 12c). The middle and bottom rows of Fig. 12 show the time-averaged SSH difference between the coarse-grained high-resolution simulation and the different combinations of subgrid terms as indicated in the subplot headings.

Two features deserve particular attention: First, we look at the flow separation from the wall near the left corner of the domain. This point of separation is moved north when the resolution is finer. The reason for this is the reduction of viscous dissipation in higher-resolution simulations (more discussion in Sein et al. (2016)). For vertical walls, the sensitivity to the level of viscosity is higher than for sloped topography. Thus, the backscatter, which has a limited impact on the location of the mean flow and mainly affects the eddy part of the flow, can not completely fix the point of separation. However, we observe the magnitude of the mean SSH difference decreases with backscatter (dark red in the left corner in Fig. 12e–i vs. Fig. 12d). This moves the point of jet separation a little further north.

The presence of the subgrid advection term (Fig. 12e) decreases the difference to the high-resolution simulation along the jet area. At the same time, it slightly worsens the SSH difference in the south of the domain. The stochastic term helps to improve the southern area SSH difference (Fig. 12g–i), but with accompanying growth of noise in the difference field along the north-west boundary (Fig. 12i). Overall, combining the classical backscatter with the additional components reduce the RMSE $\overline{SSH}$ by about 50%.

Second, the density profiles are compared on a North-South transect at 15° longitude (Fig. 13). We observe a significant difference between coarse-resolution without backscatter and any of the simulations with backscatter: without backscatter, one can see a nearly barotropic jet penetrating along the entire water column at around 30° N. The lack of eddies together with the wind forcing lead to steep isopycnals and strong vertical mixing in the middle of the domain. With backscatter, eddies can form, which immediately reduces the barotropic mixing, and also improves the form of isopycnals in the upper layers toward the slopes seen in the reference simulation. In addition, the backscatter DG simulations after 9 years might still contain some drift in the stratification, although probably small (i.e. the figures might still change a bit if we let it run for longer).

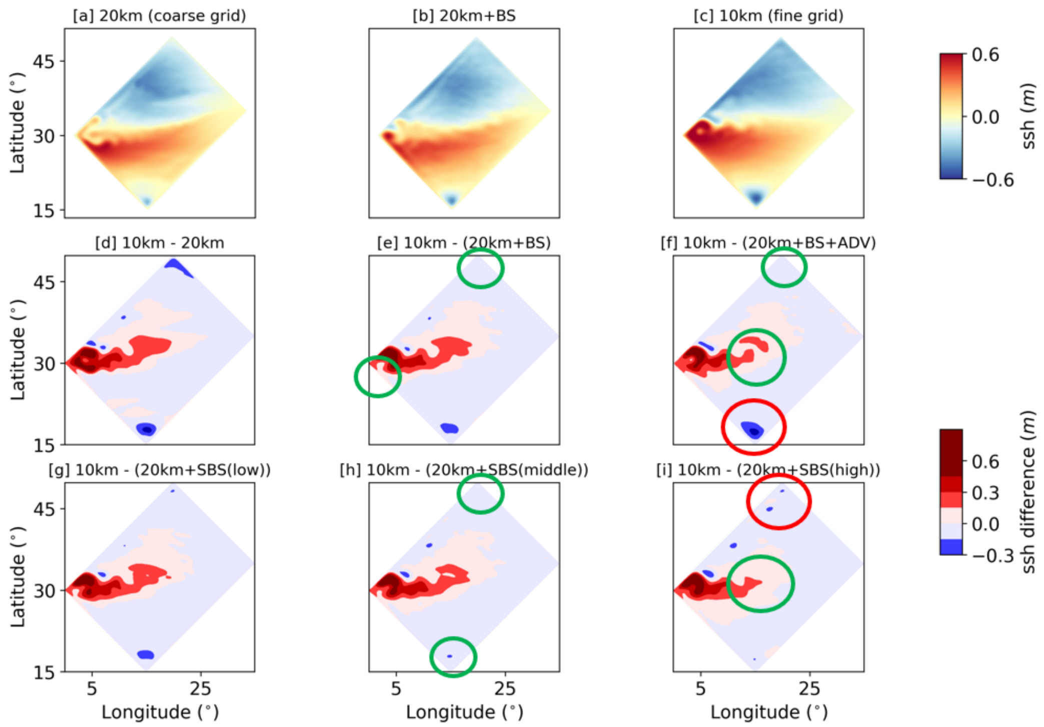

Figure 12. Over nine years, the sea surface height $[m]$ was averaged and compared between three simulations: coarse-resolution simulation (a), coarse-resolution simulation with deterministic backscatter (b), and fine resolution (c). The difference in SSH between the high-resolution coarse-grained simulation and the various coarse-resolution simulations (d-i) was also analyzed. Green and red circles indicate specific regions of improvements and impairments compared to the low resolution.

Adding advection (Fig. 13d vs. Fig. 13c, Fig. 13h vs. Fig. 13e and Fig. 13i vs. Fig. 13f) straightens the slope of isopycnals, especially in the deep southern part of the domain where the isopycnal levels bend too much in the backscatter-only case (Fig. 13c). Moreover, the contours of the isopycnal surfaces become more variable, again more like in the reference simulation. Adding the stochastic term straightens isopycnals along the entire domain. The optimal results are obtained using the stochastic term of moderate amplitude within the range of noise amplitudes. The low-amplitude noise does not have a big impact, while the high-amplitude noise leads to excessive mixing near the surface.

Based on SSH diagnostics (Fig. 13i) as well as EKE diagnostics (Table 2), the coarse-resolution setup that utilizes a combination of the middle-intensity stochastic term and advection component on the subgrid produces very good results. Furthermore, the new terms individually have the potential to improve certain flow features (Table 2) and rectify the flow behavior in different regions of the DG field (Fig. 13f,h).

Compared to the reference high-resolution simulation, coarse-resolution simulations with backscatter still have too much mixing. We increase EKE in the coarse resolution, but our diffusivity (in tracer equations) is not touched. Larger EKE corresponds to stronger temperature gradients and hence stronger mixing due to diffusion. So one would expect a bit more diapycnal mixing in this case.

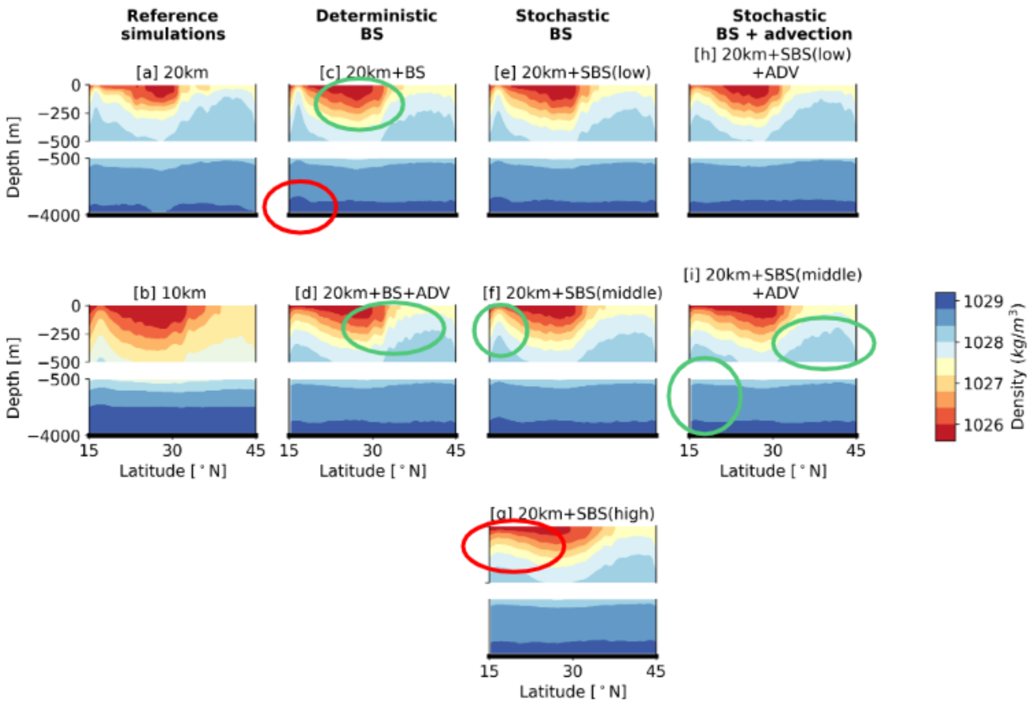

Figure 13. The annual average of the vertical density profiles along 15° longitude for the double-gyre setup. The green circles indicate where specific improvements were made toward the high-resolution reference simulation, while the red circles indicate areas with impairments. The figures have a gap on the vertical axis.

4 Discussion and conclusion

In this work, we tested the performance of two additional contributions to the subgrid energy equation, advection, and stochastic forcing, in the framework of kinetic energy backscatter of Juricke et al. (2019), which is based on earlier work by Jansen et al. (2015).

The idea behind advecting subgrid kinetic energy by the three-dimensional resolved flow is motivated by the fact that the locations of kinetic energy dissipation and forcing do not necessarily coincide. Our results show that, indeed, this additional contribution to the subgrid energy equation has an unconditionally positive effect: it corrects the behavior of isopycnals, decreases the difference of SSH to the high-resolution simulation in eddy-rich regions and improves the mean vertical profiles. Energetically, subgrid advection catalyzes all scales, enhancing energy creation and dissipation. In some situations, these effects are small but with tendency toward the reference truth. At the same time, the advection of subgrid energy adds only a 1.5% penalty to simulation time. Moreover, no tuning is necessary as it is based on physical modeling. Our conclusion is, therefore, that subgrid kinetic energy should be treated with advection.

The second additional, stochastic contribution to the subgrid energy budget has been designed to enhance the simulated eddy variability by incorporating data on regions of enhanced eddy activity from a high-resolution simulation. Such a stochastic term can improve diagnostics in the flow's calm and active areas. In particular, the improvement in SSH variability could not be achieved with deterministic backscatter only. Moreover, the spectral characteristics of the flow with stochastic subgrid forcing improve across a wide range of scales. However, we need to be cautious when using stochastic forcing: if its amplitude is too large, it can cause serious distortions and artifacts, even while a consequently improved energy spectrum may be close to expectations. Moreover, the acceptable level depends on the setup and is difficult to assess a priori. It is possible, to some extent, to guard against such failures by looking for anomalies in the amplitude of vertical velocity fluctuations in deep water or an excess of eddies in calm regions of the domain. But careful monitoring and tuning is critical and it will generally be necessary to recompute patterns for different domains.

None of the parameterizations considered here are guaranteed to force only Rossby modes. Thus, it is of concern whether backscatter leads to excessive diapycnal mixing. However, our analysis of the density diagnostics did not find any evidence of such behavior. Why and under which circumstances this is the case remains an open question and may be related to more complex bathymetry.

Stochastic forcing not only improves the flow characteristics, when done carefully, but also allows generating ensemble simulations. This enables the construction of distribution functions for output variables and measures the uncertainty of backscatter performance, an important potential direction for further research.

Several other aspects, which are worth further investigation, relate to the design of the stochastic term. One potential alternative to the EOF method is the use of dynamical mode decomposition as a tool to understand the flow variability and reduce the dimensionality of the system (Franzke et al., 2022). Following the EOF approach, the selection of data for decomposition and the number of the EOF modes, which explains a sufficient amount of missing variability, remain at the modeler's discretion.

Machine learning methods could capture the missing variability as an alternative to stochastic methods. Deep learning methods driven by the data from an idealized simulation (Bolton & Zanna, 2019) and from the realistic coupled climate models (Guillaumin & Zanna, 2021) were applied to ocean momentum forcing to represent the subgrid variability. The authors showed that convolutional neural networks can be constructed to satisfy the momentum conservation law and capture spatial and temporal eddy variability.

Finally, the necessary scale separation between the work of the backscatter and viscous operators is crucial and can be diagnosed by spectral methods. When there is not enough scale separation, the energy injection occurs in the dissipation scale range. This results in highly disturbed flow filaments and prevents eddies from propagating in a physically coherent manner. We cannot exclude potential interference between the role of advection and the degree of backscatter operator smoothing, as both affect the spatial locality of backscatter. However, insufficient scale separation between dissipation and backscatter causes serious flow distortion and is inadequate as an eddy parameterization for FESOM2.

Potential research on parametrizing mesoscale eddies beyond the scope of dynamic energy backscatter could be related to the position of large oceanic structures (for instance, the jet in the case of the double-gyre setup) in coarse resolution simulations. Dynamic backscatter, in any of its variations considered here, so far did not yield fundamental improvements, for example, of the point of jet separation. This is mostly likely due to the variety of processes interacting in such highly dynamic regions, which cannot all be improved by backscatter alone. However, improvements to the mean flow by the default dynamic backscatter have also been observed by (Juricke et al., 2020b). Nevertheless, new or extended approaches in this regard remain a focus of further research.

5 Open Research

Data Availability Statement

The model output data is publicly available at `https://zenodo.org/record/8248679`. The latest stable FESOM2 release (with the new backscatter terms implementation soon to be added) is available at `https://github.com/FESOM/fesom2`. Routines for the Fourier spectra are available at `https://zenodo.org/record/7270305` (Bellinghausen, 2022).

Acknowledgments

This paper is a contribution to the project M3 (Towards Consistent Subgrid Momentum Closures) of the Collaborative Research Centre TRR 181 "Energy Transfers in Atmosphere and Ocean" funded by the Deutsche Forschungsgemeinschaft (DFG, German Research Foundation) – Project-ID 274762653 – TRR 181. The computational resources were supplied by the supercomputing facilities at the Alfred-Wegener-Institut, Helmholtz-Zentrum für Polar- und Meeresforschung.

Appendix A Appendix

Table A1. Table of setups coefficients

Coefficients	Channel	Double-gyre
β-coefficient	$1.6 \cdot 10^{-11}$	$1.8 \cdot 10^{-11}$
Bottom drag (C_d)	0.005	0.001
Background viscosity amplitude (γ_0[m/s]) (Formula 12 in Juricke et al. (2020))	0.001	0.005
Coefficient of flow-aware viscosity (γ_1) (Formula 12 in Juricke et al. (2020))	0.06	0.3
Years of spin-up	1	50
Years of analysis/averaging	9	9

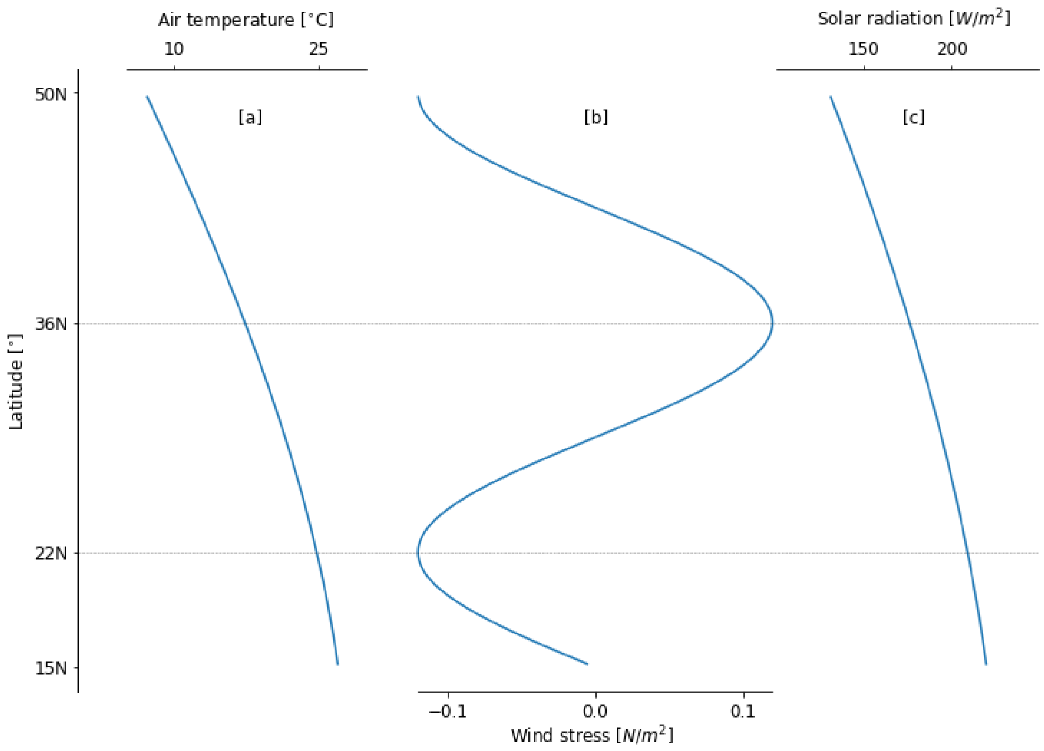

Figure A1. The analytical forcing functions are based on latitude in the double-gyre setup. These functions include air surface layer temperature (a), wind stress (b), and solar radiation (c).

References

Bellinghausen, K. (2022). *Spectral diagnostics for triangular meshes (version 1.0) [software].* Zenodo. DOI: 10.5281/zenodo.7270305

Berner, J., Shutts, G., Leutbecher, M., & Palmer, T. (2009). A spectral stochastic kinetic energy backscatter scheme and its impact on flow-dependent predictability in the ECMWF ensemble prediction system. *J. Atmos. Sci.*, *66*, 603–626. DOI: 10.1175/2008JAS2677.1

Bolton, T., & Zanna, L. (2019). Applications of deep learning to ocean data inference and subgrid parameterization. *J. Adv. Model. Earth Syst.*, *11*(1), 376–399. DOI: 10.1029/2018MS001472

Cooper, F. C. (2017). Optimisation of an idealised primitive equation ocean model using stochastic parameterization. *Ocean Model.*, *113*, 187–200. DOI: 10.1016/j.ocemod.2016.12.010

Danilov, S., Sidorenko, D., Wang, Q., & Jung, T. (2017). The Finite-volumE Sea ice–Ocean Model (FESOM2). *Geosci. Model Dev.*, *10*(2), 765–789. DOI: 10.5194/gmd-10-765-2017

Dwivedi, S., Franzke, C. L. E., & Lunkeit, F. (2019). Energetically consistent stochastic and deterministic kinetic energy backscatter schemes for atmospheric models. *Q. J. Roy. Meteorol. Soc.*, *145*, 1–11. DOI: 10.1002/qj.3625

Ferrari, R., & Wunsch, C. (2009). Ocean circulation kinetic energy: Reservoirs, sources, and sinks. *Annu. Rev. Fluid Mech.*, *41*(1), 253–282. DOI: 10.1146/annurev.fluid.40.111406.102139

Fox-Kemper, B., Adcroft, A., Böning, C. W., Chassignet, E. P., Curchitser, E., Danabasoglu, G., . . . Yeager, S. G. (2019). Challenges and prospects in ocean circulation models.

Frontiers in Marine Science, *6*. DOI: 10.3389/fmars.2019.00065

Fox-Kemper, B., Ferrari, R., & Hallberg, R. (2008). Parameterization of mixed layer eddies. Part I: theory and diagnosis. *J. Phys. Oceanogr.*, *38*, 1145–1165. DOI: 10.1175/2007JPO3792.1

Franzke, C. L. E., Gugole, F., & Juricke, S. (2022, 07). Systematic multi-scale decomposition of ocean variability using machine learning. *Chaos: An Interdisciplinary Journal of Nonlinear Science*, *32*(7), 073122. DOI: 10.1063/5.0090064

Frederiksen, J., O'Kane, T., & Zidikheri, M. (2013, 01). Subgrid modelling for geophysical flows. *Phil. Trans. R. Soc. A*, *371*, 20120166. DOI: 10.1098/rsta.2012.0166

Gent, P. R. (2011). The Gent–McWilliams parameterization: 20/20 hindsight. *Ocean Model.*, *39*(1–2), 2–9. DOI: 10.1016/j.ocemod.2010.08.002

Gent, P. R., & McWilliams, J. C. (1990). Isopycnal mixing in ocean circulation models. *J. Phys. Oceanogr.*, *20*, 150–155. DOI: 10.1175/1520-0485(1990)020⟨0150:IMIOCM⟩2.0.CO;2

Grooms, I., & Majda, A. J. (2013). Efficient stochastic superparameterization for geophysical turbulence. *Proc. Nat. Acad. Sci.*, *110*, 4464–4469. DOI: 10.1073/pnas.1302548110

Grooms, I., Majda, A. J., & Smith, K. S. (2015). Stochastic superparameterization in a quasigeostrophic model of the Antarctic Circumpolar Current. *Ocean Model.*, *85*, 1–15. DOI: 10.1016/j.ocemod.2014.10.001

Guillaumin, A. P., & Zanna, L. (2021). Stochastic-deep learning parameterization of ocean momentum forcing. *J. Adv. Model. Earth Syst.*, *13*(9), e2021MS002534. DOI: 10.1029/2021MS002534

Hallberg, R. (2013). Using a resolution function to regulate parameterizations of oceanic mesoscale eddy effects. *Ocean Model.*, *72*, 92–103. DOI: 10.1016/j.ocemod.2013.08.007

Hewitt, H., Roberts, M., Mathiot, P., Biastoch, A., Blockley, E., Chassignet, E., … Zhang, Q. (2020, 12). Resolving and parameterising the ocean mesoscale in earth system models. *Current Climate Change Reports*, 137–152. DOI: 10.1007/s40641-020-00164-w

Jansen, M. F., Adcroft, A., Khani, S., & Kong, H. (2019). Toward an energetically consistent, resolution aware parameterization of ocean mesoscale eddies. *J. Adv. Model. Earth Syst.*, *11*(8), 2844–2860. DOI: 10.1029/2019MS001750

Jansen, M. F., & Held, I. M. (2014). Parameterizing subgrid-scale eddy effects using energetically consistent backscatter. *Ocean Model.*, *80*, 36–48. DOI: 10.1016/j.ocemod.2014.06.002

Jansen, M. F., Held, I. M., Adcroft, A. J., & Hallberg, R. (2015). Energy budget-based backscatter in an eddy permitting primitive equation model. *Ocean Model.*, *94*, 15–26. DOI: 10.1016/j.ocemod.2015.07.015

Juricke, S., Bellinghausen, K., Danilov, S. D., Kutsenko, A. A., & Oliver, M. (2023). Scale analysis on unstructured grids: Kinetic energy and dissipation power spectra on triangular meshes. *J. Adv. Model. Earth Syst.*, *15*, e2022MS003280. DOI: 10.1029/2022MS003280

Juricke, S., Danilov, S., Koldunov, N., Oliver, M., Sein, D. V., Sidorenko, D., & Wang, Q. (2020). A kinematic kinetic energy backscatter parametrization: From implementation to global ocean simulations. *J. Adv. Model. Earth Syst.*, *12*, e2020MS002175. DOI: 10.1029/2020MS002175

Juricke, S., Danilov, S., Koldunov, N., Oliver, M., & Sidorenko, D. (2020b). Ocean kinetic energy backscatter parametrization on unstructured grids: Impact on global eddy-permitting simulations. *J. Adv. Model. Earth Syst.*, *12*, e2019MS001855. DOI: 10.1029/2019MS001855

Juricke, S., Danilov, S., Kutsenko, A., & Oliver, M. (2019). Ocean kinetic energy backscatter parametrizations on unstructured grids: Impact on mesoscale turbulence in a channel. *Ocean Model.*, *138*, 51–67. DOI: 10.1016/j.ocemod.2019.03.009

Juricke, S., Palmer, T. N., & Zanna, L. (2017). Stochastic sub-grid scale ocean mixing: Impacts on low frequency variability. *J. Climate*, *30*(30), 4997–5019. DOI: 10.1175/

JCLI-D-16-0539.1

Klöwer, M., Jansen, M. F., Claus, M., Greatbatch, R. J., & Thomsen, S. (2018). Energy budget-based backscatter in a shallow water model of a double gyre basin. *Ocean Model.*, *132*, 1–11. DOI: 10.1016/j.ocemod.2018.09.006

Leutbecher, M., Lock, S.-J., Ollinaho, P., Lang, S. T. K., Balsamo, G., Bechtold, P., ... Weisheimer, A. (2017). Stochastic representations of model uncertainties at ECMWF: state of the art and future vision. *Quart. J. Roy. Meteorol. Soc.*, *143*(707), 2315–2339. DOI: 10.1002/qj.3094

Levy, M., Klein, P., Treguier, A.-M., Iovino, D., Madec, G., Masson, S., & Takahashi, K. (2010, 12). Modifications of gyre circulation by sub-mesoscale physics. *Ocean Model.*, *34*, 1–15. DOI: 10.1016/j.ocemod.2010.04.001

Mana, P. P., & Zanna, L. (2014). Toward a stochastic parameterization of ocean mesoscale eddies. *Ocean Model.*, *79*, 1–20. DOI: 10.1016/j.ocemod.2014.04.002

Pacanowski, R. C., & Philander, S. G. H. (1981). Parameterization of vertical mixing in numerical models of tropical oceans. *J. Phys. Oceanogr.*, *11*(11), 1443–1451. DOI: 10.1175/1520-0485(1981)011⟨1443:POVMIN⟩2.0.CO;2

Perezhogin, P. (2019). Deterministic and stochastic parameterizations of kinetic energy backscatter in the NEMO ocean model in Double-Gyre configuration. *IOP Conf. Ser.: Earth Environ. Sci.*, *386*, 012025. DOI: 10.1088/1755-1315/386/1/012025

Redi, M. H. (1982). Oceanic isopycnal mixing by coordinate rotation. *J. Phys. Oceanogr.*, *12*(10), 1154–1158. DOI: 10.1175/1520-0485(1982)012⟨1154:OIMBCR⟩2.0.CO;2

Scholz, P., Sidorenko, D., Danilov, S., Wang, Q., Koldunov, N., Sein, D., & Jung, T. (2022). Assessment of the finite-volume sea ice–ocean model (fesom2.0) – part 2: Partial bottom cells, embedded sea ice and vertical mixing library cvmix. *Geoscientific Model Development*, *15*(2), 335–363. DOI: 10.5194/gmd-15-335-2022

Scholz, P., Sidorenko, D., Gurses, O., Danilov, S., Koldunov, N., Wang, Q., ... Jung, T. (2019). Assessment of the Finite VolumE Sea Ice Ocean Model (FESOM2.0), Part I: Description of selected key model elements and comparison to its predecessor version. *Geosci. Model Dev. Discussions*, *2019*, 1–42. DOI: 10.5194/gmd-2018-329

Sein, D. V., Danilov, S., Biastoch, A., Durgadoo, J. V., Sidorenko, D., Harig, S., & Wang, Q. (2016). Designing variable ocean model resolution based on the observed ocean variability. *J. Adv. Model. Earth Syst.*, *8*(2), 904–916. DOI: 10.1002/2016MS000650

Soufflet, Y., Marchesiello, P., Lemarié, F., Jouanno, J., Capet, X., Debreu, L., & Benshila, R. (2016). On effective resolution in ocean models. *Ocean Model.*, *98*, 36–50. DOI: 10.1016/j.ocemod.2015.12.004

Zanna, L., Mana, P. P., Anstey, J., David, T., & Bolton, T. (2017). Scale-aware deterministic and stochastic parametrizations of eddy-mean flow interaction. *Ocean Model.*, *111*, 66–80. DOI: 10.1016/j.ocemod.2017.01.004